The University of New South Wales
School of Physics

Analysis of Gattini Antarctic Sky Camera Data

Timothy Blair Leslie
<timl@phys.unsw.edu.au>

Bachelor of Science
(Physics)

June 2007

Supervisors: Prof. Michael Ashley, Dr. Jon Lawrence

Abstract

The Gattini project consists of two site testing cameras located at Dome C on the Antarctic plateau, which are designed to measure the background sky brightness and to collect cloud cover statistics. In this thesis I present an analysis of the data produced by the Gattini cameras for the winter of 2006. Software to analyse the large data sets generated by the cameras is developed and presented along with preliminary estimates of the background sky brightness as well as cloud cover estimates. The background sky brightness is measured to be between 20.5 and 21.0 mag/arcsec^2. A lower bound for the amount of time with clear skies is estimated at 79.4% between May and October.

Contents

List of Figures

List of Tables

Acknowledgements

This thesis represents a small part of the Gattini project as a whole, and I would like to acknowledge the following institutions and individuals who have played significant roles in the project. Anna Moore (Caltech/Arcetri), PI of Gattini project. Eric Aristidi (University of Nice), who was the winter-over astronomer supporting the operation of Gattini at Dome C during 2006. The French and Italian Antarctic agencies (French Polar Institute Paul Emile Victor (IPEV) and Programma Nazionale Ricerche in Antartide (PNRA)) for installation and support of the cameras at Dome C. The Australian Antarctic Division and the US National Science Foundation for financial support. The Australian Research Council for financial support. The rest of the Gattini team, who have all contributed to this project: Tony Travouillon (Caltech), Michael Ashley, Jon Everett, Suzanne Kenyon, Jon Lawrence, Daniel Luong-Van, Andre Phillips, John Storey, Melinda Taylor (UNSW), Maurizio Busso, G. Tosti (University of Perugia), Maurizio Candidi (PNRA), Brice Le Roux (University Marseille), Roberto Ragazzoni, Piero Salinari (University of Arcetri) and Runa Briguglio (University Roma).

I would also like to personally thank those individuals who have assisted me in one way or another throughout the completion of this thesis. My supervisors, Prof. Michael Ashely and Dr. Jon Lawrence, for their excellent direction and feedback throughout the project. My fellow honours students, for sharing this experience with me and providing solidarity on our respective journeys of discovery. Dr. Andreas Leofler, for putting my Achilles tendon back together when it was inconsiderate enough to snap while I was trying to write a thesis. Finally, Leigh Dunlop, for her continued love and support through yet another massive project. Thank you all.

Chapter 1

Introduction

It is often said that space is the final frontier and this is particularly true when it comes to picking the best locations for astronomical observatories. Unfortunately the cost of putting a telescope into space is truly astronomical, so new, terrestrial observatory sites are always being considered.

To determine whether a site is favourable for ground based observation, extensive testing must be carried out to quantify its atmospheric characteristics. This ensures that the money invested in developing telescope facilities has the greatest scientific return.

In this thesis I present the results of one such site testing experiment which has been running at Dome C, high on the Antarctic plateau, since February 2006.

1.1 Astronomy in Antarctica

The high Antarctic plateau provides unique conditions which are particularly well suited to astronomy. It has been found that the high points on the plateau have conditions which are superior to the best sites at mid latitudes.

The Antarctic plateau has long been identified as an excellent potential site for astronomical observations [1]. While the South Pole itself has been inhabited for 50 years now, with year round occupation for over 30 years, other, more remote sites have been identified as potentially superior locations for observations.

Meteorological records gave indications that the seeing conditions at the summits of the plateau, such as Dome C and Dome A, would be considerably better than those at the South Pole [2] [3].

Measurements of auroral activity show that the summits of the plateau suffer significantly less from auroral contributions to the sky brightness than the South Pole [4]

Atmospheric models have also been developed which showed that sites high on the plateau are well suited to both infrared and submillimetre observations, with sensitivity gains over mid-latitude sites of up to three orders of magnitude [5].

The potential for astrometric interferometry at the summits of the plateau has also been noted, based on the excellent results found at the South Pole and the expectation of lower turbulence levels at these higher elevations [6].

1.2 Dome C

Dome C is located on the Antarctic plateau at 76°6′ South, 123°21′ East (Fig. 1.1), at an altitude of 3250m. In recent years a number of experiments have been run to quantify the atmospheric characteristics of this site to determine its suitability as a site for large telescopes for optical, infrared and submillimetre astronomy.

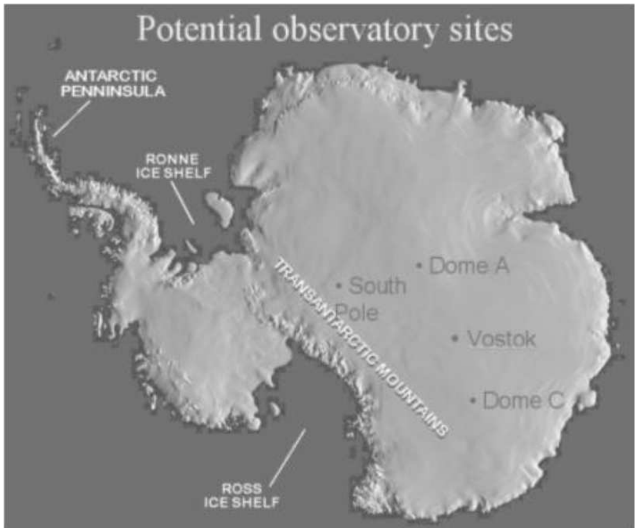

Figure 1.1: A map of Antarctica showing the location of Dome C and other important landmarks.

Concordia station, which is a French/Italian collaboration, has been established at Dome C and provides a base from which experiments can be run.

1.2.1 Weather

Experiments which measure the wind, temperature and cloud cover at Dome C have shown it to be a very favourable location for ground based astronomy. Aristidi et. al. (2005) found that the average ground wind speed over a period of time between 1984 and 2003 was 3.2ms^{-1} [7]. They were also able to show that the average wind speed was lower during astronomical darkness, which is when the low wind speed is most important. These wind speeds are significantly lower than most mid latitude sites (Paranal, for example, has an average wind speed of 6.6ms^{-1})[1] as well as being an improvement on the South Pole, with an average wind speed of 5.5ms^{-1}.[2] Low surface wind speeds are an important factor for an observational site, as they imply a low level of turbulence near the surface. Surface winds can also affect the telescope structure itself.

The temperature at Dome C is also well suited to astronomy. Not only are there consistently low temperatures, but the surface inversion layer only extends to a height of around 50 meters, compared to 220m at the South Pole [7]. A low temperature is important as it leads to low atmospheric thermal emission, which is particularly important for infrared observations.

The amount of usable dark time at a particular site depends heavily on how often the skies above the site are clear. Measurements with the ICECAM experiment over the winter of 2001 showed that there was evidence of clear skies 74% of the time [8].

1.2.2 Astronomical Seeing

An important characteristic of an observatory site is the *astronomical seeing*. The seeing at ground based observatories is generally measured in arcseconds, and defines the best possible angular resolution achievable with an optical telescope.

Measurements of the seeing at Dome C have been conducted since December 2002 [9]. A differential image motion monitor (DIMM) experiment ran over

---

[1] http://www.eso.org/gen-fac/pubs/astclim/lasilla/

[2] http://www.esrl.noaa.gov/gmd/publications/annrpt24/spo152.htm

the summers from 2002 until 2005 to assess the ground based seeing and also the contribution of the surface boundary layer to these measurements. During daytime observations in the summer a mean seeing value of 0.66” was found using a telescope at a height of 8.5 metres off the ice. Concurrent measurements at a height of 3.5m showed that nearly half of the ground surface turbulence was to be found in the 5m region between the two monitors [10].

Measurements taken above this ground layer turbulence show seeing values superior to any site on the planet. Balloon based measurements in the winter have measured the seeing at a height of $h \geq 30m$ to be $0.36'' \pm 0.19$ [11]. Measurements taken using a combination of MASS (multi-aperture scintillation sensor) and SODAR (sonic detection and ranging) from the AASTINO (Automated Astrophysical Site Testing International Observatory) [12] facility have measured the mean seeing above 30m to be 0.27” [13]. These values compare extremely favourably against other sites such as Mauna Kea (night time seeing of 0.63” [14]) and the South Pole (night time seeing of 1.74” [15]).

1.2.3 Optical Sky Brightness

On the back of the remarkable seeing results found at Dome C, investigations began into the background sky brightness, another critical parameter in deciding whether to develop a large telescope at the site.

The brightness of astronomical objects is measured on a scale based on the negative logarithm of their intensity. The history of this scale dates back to the ancient Greeks (see [16] for a brief overview of the history of the magnitude scale). Objects are measured on this scale in units of magnitude (mag), however for regions of the sky we want to know the brightness per unit area of the sky, so we measure the background sky brightness in mag/arcsec^2. Some of the darkest skies have been measured at the Paranal site in northern Chile, with a night sky brightness of 21.6 mag/arcsec^2 [17] in the V band (centered on 505nm).

An extensive review of the contributing sources of optical sky brightness was presented by Kenyon and Storey in 2006 [18]. The main contributors to the sky brightness were identified as scattered sunlight, moonlight, aurora, airglow, zodiacal light, integrated starlight, diffuse galactic light, integrated cosmic light and light pollution. In addition to these factors, the amount of astronomical dark time (defined as the sun being more than 18° below the horizon) also plays a crucial role in determining the quality of a site for astronomical observation.

The most significant contributors to the sky brightness are scattered and direct sunlight. When the sun is below the horizon, scattering of the sunlight contributes to the brightness until the sun is around 18° below the horizon. The review found that, depending on the proportion of cloud free nights at Dome C, both Mauna Kea and Done C had a similar amount of usable astronomical dark time. This is despite the fact that the total dark time at the high latitude site is approximately twice that at Dome C.

The next largest sky brightness contributor is the moon, which also leads to both direct and scattered light. The brightness contribution of the moon depends both on its position in the sky and its phase. The contribution to the brightness at zenith due to the moon is greatly reduced at Dome C compared to other sites due to the fact that the moon never rises to closer then 43° from the zenith. This benefit is negated somewhat by the fact that the fullness of the moon and its elevation above the horizon are correlated, meaning the moon tends to be relatively high in the sky when it is at its fullest. Overall, the median contribution to brightness at zenith from moonlight was found to be 1.7 mag/arcsec^2.

Aurora over Antarctica tend to occur within an annulus centered on the geomagnetic South Pole (GSP). The location of the GSP (as of January 2005) was 79.5° south, 108.5° east. This is reasonably close to the location of Dome C, meaning that Dome C lies well within the inner radius of the annulus of auroral activity. As such the contribution due to auroral events is expected to be minimal. The total contribution is dependent on the 11 year sunspot cycle. The review quotes figures of an auroral contribution of less than 22.7 mag/arcsec^2 for 50% of the wintertime during a solar maximum year and 23.5 mag/arcsec^2 during a solar minimum year.

Zodiacal light refers to the sunlight which is scattered off the disk of interplanetary dust which lies in the plane of the solar system. Because this plane remains reasonably low in the sky at Dome C, the contribution to the sky brightness is quite small. The brightest it gets is 23.1 mag/arcsec^2 at zenith, and even at 60° from the zenith it is no brighter than 22.0 mag/arcsec^2.

Airglow is due to chemiluminescence of atoms and molecules in the upper atmosphere. A number of contributing emission lines are identified in the review, the strongest of which is from the hydroxyl radial (OH). The overall contribution to sky brightness due to airglow at Dome C is found to not be significantly different from that at temperate sites.

A grating spectrograph experiment, NIGEL, was installed at Dome C over the summer of 2004-2005 to measure the sky brightness at Dome C [19]. During this deployment calibration data was obtained during periods of twilight. The equipment is currently being upgraded before redeployment to Antarctica in the coming summer.

1.2.4 Infrared and Submillimetre

As well as being a promising site for optical observations, testing has also been carried out at Dome C to measure the suitability for both infrared and submillimetre astronomy. Initial measurements of the sky opacity at 350μm suggest that Dome C has a median opacity of $\tau_0 = 1.61$ compared to $\tau_0 = 1.80$ at the South Pole [20]. Measurements of the infrared sky brightness have been made across a continuum of wavelengths and show a number of particularly clear frequency windows [21].

Preliminary investigations into the conditions for millimetre astronomy have also been conducted at Dome C. Site testing suggests that Dome C is at least as good as, if not better than, the South Pole for millimetre wavelength observations [22]. In fact, Dome C was used as a millimetre observation location as early as 1996, with the APACHE96 telescope measuring cosmic microwave background radiation anisotropies at millimeter wavelengths [23].

1.3 Gattini Project

The Gattini project is a collaboration between Australian, Italian, French and US astronomers, running site testing experiments at Dome C, Antarctica as part of the larger IRAIT project [24].

In February 2006 the Gattini project began operations at Dome C. The aim of this project is to measure the background sky optical brightness and collect statistics of cloud cover and auroral events [25].

The Gattini project consists of two cameras operating at Dome C, which take images of the sky every five minutes. These images are stored for subsequent offline processing and analysis. The two cameras are called Gattini-SBC and Gattini-allsky. Gattini-SBC has a relatively narrow field of view and is designed to measure the background sky brightness, calibrated against known catalogue stars. The Gattini-allsky camera has a wide field of view and is designed to allow for the collection of statistics about cloud cover and auroral events.

While the cameras have been in operation for over 12 months, a complete analysis of the data collected has not yet been performed, as the data was only returned in early 2007.

1.4 Overview

The aim of this thesis is to analyse and reduce the data from both of the Gattini cameras from the 2006 winter period as well as developing programs to automatically perform the data reduction.

In Chapter 2 I describe the experimental setup, including the hardware and software systems which collect the data as well as the different types of data produced. This is followed in Chapter 3 by a gallery of images taken by the cameras, which provides an idea of the kinds of data which need to be handled.

In Chapter 4 I outline the analysis which was performed on the data to extract the relevant information from the images. Chapter 5 presents the software which was used to orchestrate the image analysis and the subsequent exploration of the generated results.

Chapter 6 presents the results of the analysis, including results for the background sky brightness and cloud cover statistics. In Chapter 7 various aspects of the project are discussed, along with a summary of issues to be addressed in the ongoing operation of the cameras. Concluding remarks are given in Chapter 8

Chapter 2

Experimental Setup

The Gattini project consists of a number of hardware and software system running together to perform the different aspects of the experiment. In this chapter I describe these systems, how they interact, and the data which they produce.

2.1 Cameras

The two cameras used in the experiment are virtually identical, except for the lenses and the external windows of their enclosures. The cameras live atop a laboratory located approximately 1km from Concordia station at Dome C (see Figure 2.1). Each camera is enclosed in an airtight box with viewing window and is controlled via USB by a single PC running inside the lab.

Both cameras use identical Apogee Alta U2000[1] camera systems which have Kodak KAI-2020M[2] interline CCDs. The CCDs consist of 1600x1200 7.4μm pixels with a peak quantum efficiency of 56% at 480nm. The interline CCDs were chosen as they remove the need for a mechanical shutter on the camera.

Power to the Gattini experiment is supplied directly from the AC mains in the Concordia station. There is also a UPS inside the lab so that in the event of a power outage at the station, the systems can be shut down properly, which protects against damage to the disks and data.

Figure 2.2 shows both cameras in their enclosures with the lids open. A

---

[1] http://www.ccd.com/alta_u2000.html

[2] http://www.ccd.com/pdf/ccd_2000.pdf

Figure 2.1: The atmospheric lab in the background of the image, with the camera enclosures visible on its roof.

complete description of the physical setup of the cameras is given by Moore et. al. in [25]

2.1.1 Gattini-allsky

The primary aim of the Gattini all sky camera is to collect long term cloud cover statistics and to measure any bright auroral events. The all sky camera uses a Pentax C20616TH 6.5mm f/1.8 lens which gives a plate scale of 3.9 arcmin/pixel and a 104.4 x 78.3 degree field-of-view. There are no optical filters attached to the all sky camera, so the frequency response is simply that of the CCD, which is shown in Figure 2.3.

The centre of the all sky field of view is 190.7 azimuth, 81.3 elevation. The sky camera enclosure has a domed, perspex window, as can be seen in Figure 2.4.

Figure 2.2: The two cameras in their enclosures in the lab at UNSW. The all sky camera is on the left and the SBC is on the right.

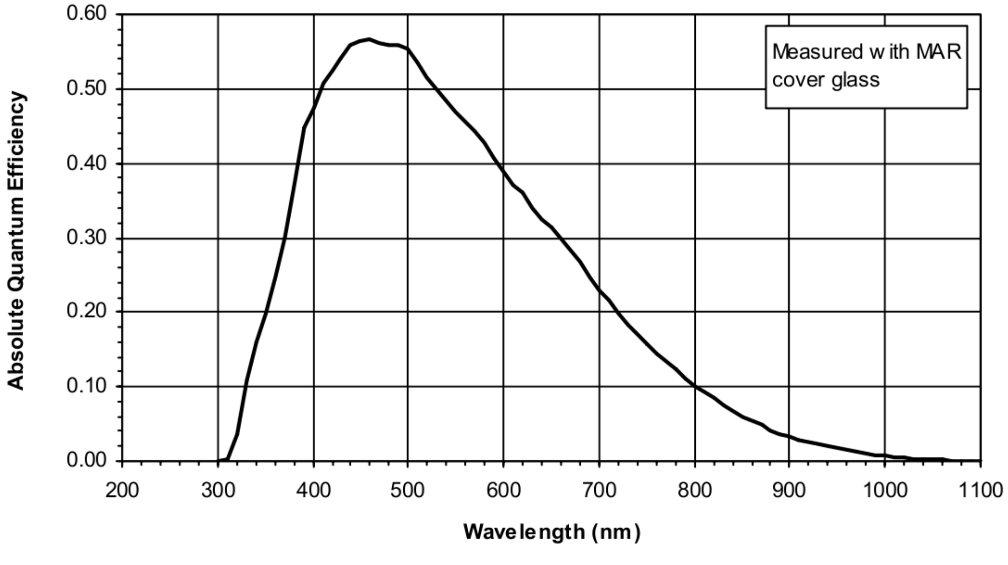

Figure 2.3: The CCD sensitivity.

Figure 2.4: The all sky camera in its enclosure.

2.1.2 Gattini-SBC

The Gattini Sky Brightness Camera (SBC) is designed to take narrow field images of the sky, with the primary aim being to determine the background sky brightness. A secondary aim of the SBC is to investigate the potential for transient astronomy. The SBC camera uses a 135 mm focal length f/2.8 lens giving a plate scale of 11.3 arcsec/pixel and 5.0 x 3.8 degree field of view. A sloan g' filter (Fig. 2.5) is used which has a central wavelength of 477nm and a bandwidth of approximately 150nm.

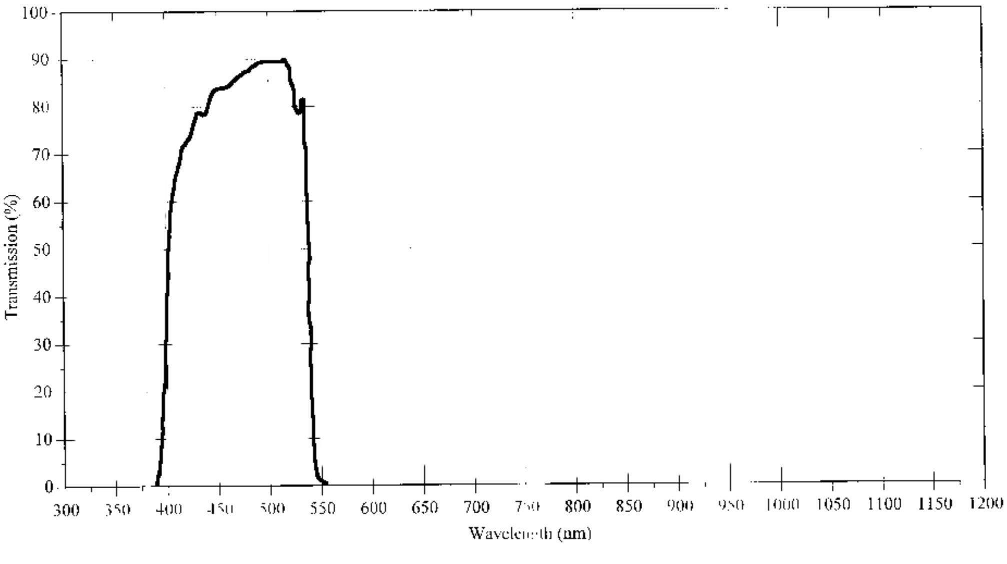

Figure 2.5: The sloan g' filter.

The window on the SBC enclosure is a flat piece of Pyrex glass, as can be seen in Figure 2.6. This was chosen because a domed window like the one on the all sky enclosure would result in too much optical aberration. The centre of the SBC field of view is at approximately 177.25 azimuth, 76.1 elevation, which is close to the celestial south pole. This ensures that some stars remain within the field of view constantly.

Figure 2.6: The SBC in its enclosure.

2.2 CCD Properties

The images are recorded using 1600x1200 pixel CCDs. The properties of these CCDs play an important role in our analysis, so it is vital that these properties are well understood.

Figure 2.7 shows a schematic of the pixel layout for the CCD as well as a pin layout diagram showing how a controlling system can connect to the CCD. The basic structure of the CCD consists of an array of pixels, each of which consists of a small photodiode. These photodiodes are controlled by digital electronics, which provide the required interfaces for a controlling system to take images as required. When photons hit a pixel they create an electron-hole pair, which is collected in a potential well.

To take an image, the controlling system raises the voltage on an input pin (`VSUB`), which empties all the potential wells. When this voltage is then dropped, the CCD begins collecting electrons again. After the desired in-

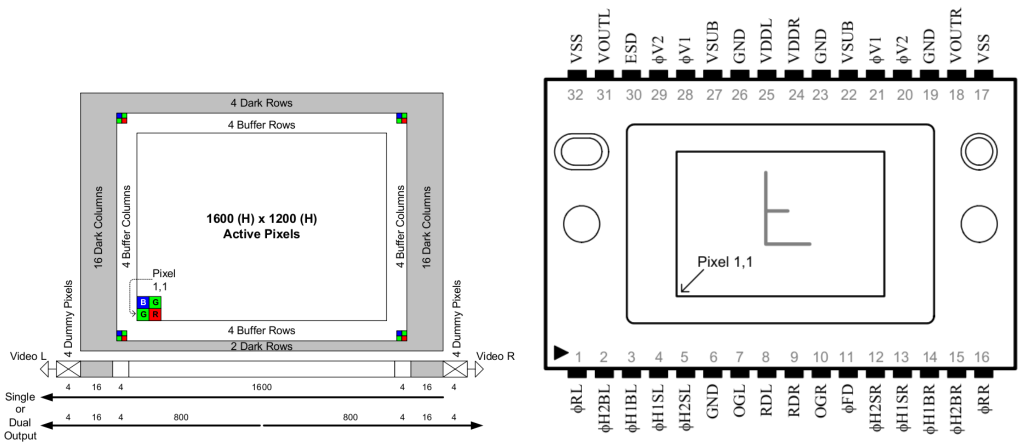

Figure 2.7: Diagrams of the sensor architecture (left) and pin layout (right) for the CCDs, taken from the CCD specification.

tegration time, a signal is sent on another input pin (ϕ`V2`) which begins the read out process.

To read out the images, a clock pulse is sent which shifts the charge in each row of the image into the row below. The bottom row is shifted into a region known as the horizontal register. From here, another series of clock pulses shifts the charge in this row to the left, one pixel at a time. The charge in the pixel on the left end of the register gets shifted onto a floating diffusion output node. The voltage at this node is proportional to the amount of charge present. This voltage can be accessed from the pin `VOUT`. This process is then repeated for each row in the image. By running the signal from `VOUT` through an analog to digital converter (ADC) the amount of charge from each pixel can be read out, digitised and stored. The resulting image will have a discrete value at each pixel. This value is known as the *pixel count* and is related to the number of electrons (and hence, photons) collected by the corresponding photodiode by a constant gain factor.

2.2.1 Bias Level and Read Out Noise

Due to the electronics involved in the CCD, a signal will be registered even if the image is taken with a zero second exposure time. This signal is an inherent property of the CCD and is present in every image recorded. The signal comprises two components: the *bias level* and the *read out noise*. The bias level is the DC component of the signal while the read out noise is the variation about this level.

2.2.2 Interpixel Variation

Despite the best efforts of the manufacturers, the sensitivity of each pixel is not completely identical. As such, for a constant illumination of the CCD, each pixel will receive a different number of photons, and of the photons received, a different percentage will be converted to electrons. This interpixel variation is small, but needs to be accounted for, particularly if certain pixels are dead (i.e. they generate no charge) or saturated (i.e. they generate too much charge).

2.3 Automated Camera Control System

The task of actually taking images with the cameras is controlled by a shell script which is run on the controlling PC every five minutes by `cron`[3]. The shell script, which is attached as Appendix B, is called `slave_images`. This script sets the exposure time for each camera, takes the image, compresses it and then transfers it to the main storage disk.

The exposure time alternates between 40 seconds and 8 seconds when the sun is sufficiently low in the sky. When the sun is above -10 degrees relative to the horizon, the exposure time is reduced to ensure that the images do not saturate.

The data is stored on site over the winter until it can be transported in bulk, however a small subset of the data is transferred daily over an Iridium satellite link to the machine `mcba4.phys.unsw.edu.au`. This daily upload allows the cameras to be monitored remotely and also for preliminary analysis to be performed. The following data is sent every 24 hours for each camera:

- Two complete image files taken at 23h13m and 03h43m and one zero frame (see Section 2.4.3).
- A compressed jpeg version of one image from each hour.
- Cropped 200 x 200 pixel sections of the FITS files (see Section 2.4.1), close to the celestial South Pole, for the images taken at 43 and 48 minutes past each hour.

The PC which controls the cameras can be remotely logged into via the Iridium satellite link, allowing the experiment to be controlled over the winter period.

---

[3] `cron` is a Unix tool for running programs at scheduled intervals.

2.4 Data

During both the testing and operational phases, the cameras have been producing data which needs to be analysed. This data consists both of production data, being the actual images of the sky, as well as testing and calibration images.

2.4.1 Production Data

The production data used in this project consisted of images from the time the cameras went into operation in February 2006 until the 12th of October 2006. The full data set comprises of 42431 images from SBC and 43309 images from the all sky camera.

Each image is a FITS[4] file, compressed using `bzip2`. Each image consists of 1600x1200x16 bits of image data plus a small (< 1kB) header. Fully compressed, the data set requires approximately 180GB of storage. If stored in its uncompressed form, it would require around 307GB of storage.

The data was retrieved from Dome C and returned to Sydney on a single hard drive in February 2007. It has subsequently been backed up and made available for analysis.

In order to process a given image, we must uncompress the file, apply a flat field transformation (see Section 2.4.4) and then run our analysis over it. The process of flat fielding rescales the image data from 16 bit integers to 32 bit floating point values. This effectively doubles the size of the image. Were we to process the images in such a way that had them all uncompressed and flat field transformed at the same time we would require over 600GB of storage space. This goes well beyond what is available, so any processing system must avoid such a situation. This problem will be addressed in the Chapter 5.

It should be noted that after March 3rd the system was adjusted such that each frame was bias subtracted. This was done by subtracting the minimum value from the dark pixel rows outside the active 1200x1600 pixel region. This resulted in a residual bias count of around 75 counts (see Chapter 6) compared to the approximately 2700 counts which were bias subtracted.

---

[4] http://fits.gsfc.nasa.gov/standard21b.html

2.4.2 Dark Frames

Before the cameras were sent to Dome C, a number of test images were taken in dark conditions. These images were taken at a range of temperature and exposure times to try to determine the dark current of the cameras.

The dark current is the current which is measured from the CCD when there is no external incident flux. This current is usually due to thermal excitation of electrons on the chip and decreases logarithmically with the temperature. The CCD specification does not provide dark current values at the low temperatures which we have been using them at, however we expect it to be negligible.

Approximately 50 dark frames were taken for each camera, under a range of temperature conditions similar to those which they would be exposed to on location. The results from these dark frames are discussed in Chapter 6.

2.4.3 Bias Frames

As was discussed above, there is an inherent signal generated by the electronics of the CCD itself, giving a bias level and read out noise.

To monitor this signal a zero second exposure was taken each day at 23h48m. These bias frames allow us to keep track of the read noise and bias level from the electronics of the CCD. The error in the distribution of pixel values from these images gives us the read out noise. This read out noise provides a lower limit on any signal which we can detect.

2.4.4 Flat Frames

The properties of both the lens and the CCD on the cameras mean that for a constant illumination of the lens there is a variation across the image in the pixel values recorded. These systematic variations can be accounted for by scaling each image by a certain value at each pixel. The scaling factors at each pixel constitutes an image in itself, known as a flat field frame.

As well as the dark frames taken during the testing of the cameras, a number of images were also taken under conditions with uniform illumination of the lenses and at temperatures similar to those the cameras would be operating at on site. If the lens and CCD were both perfect, we would expect these images to be perfectly flat (i.e. each pixel would have the same value). Any variation in these images represents the variation due to the CCD and the lens. By combining these images together we can eliminate the variation which is due to read out noise and obtain a single flat frame which represents the systematic variations across the image.

Chapter 3

Image Gallery

To gain an insight into the nature of the data being collected, it is useful to see some of the different type of images which are being analysed. In this chapter I present a range of images from each camera which represent different features of the images occurring under various conditions.

3.1 Clear Sky

During times when the lens was not obscured by ice, there were no clouds in the sky and the sun and moon were both well below the horizon, very clear images were taken with both cameras. Figure 3.1 shows images under these conditions for the all sky camera and SBC respectively.

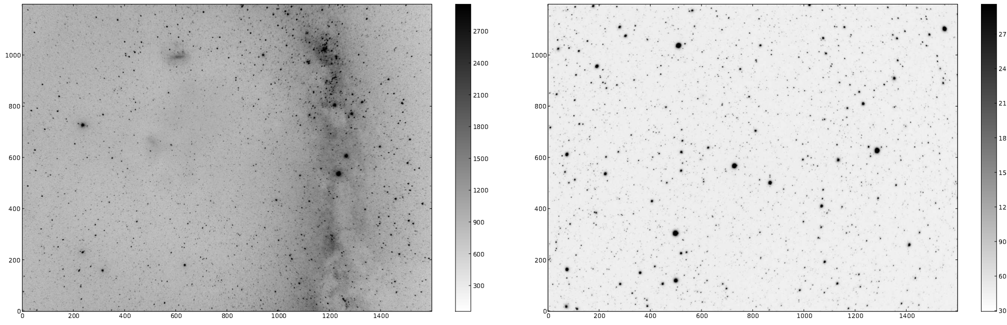

Figure 3.1: All sky camera (left) and SBC (right) in clear time.

The images are shown on a negative colour scale of pixel counts. Individual stars can easily be seen in the SBC image. The all sky camera shows large scale features such as the band of the Milky Way running down the right hand side of the image.

3.2 Ice and Snow

One of the ongoing problems with the SBC was that its window would often ice over, rendering a lot of its data useless. When the camera was iced over, we saw images such as Figure 3.2. It is clear that no stars can be identified, hence no analysis can be performed on such an image.

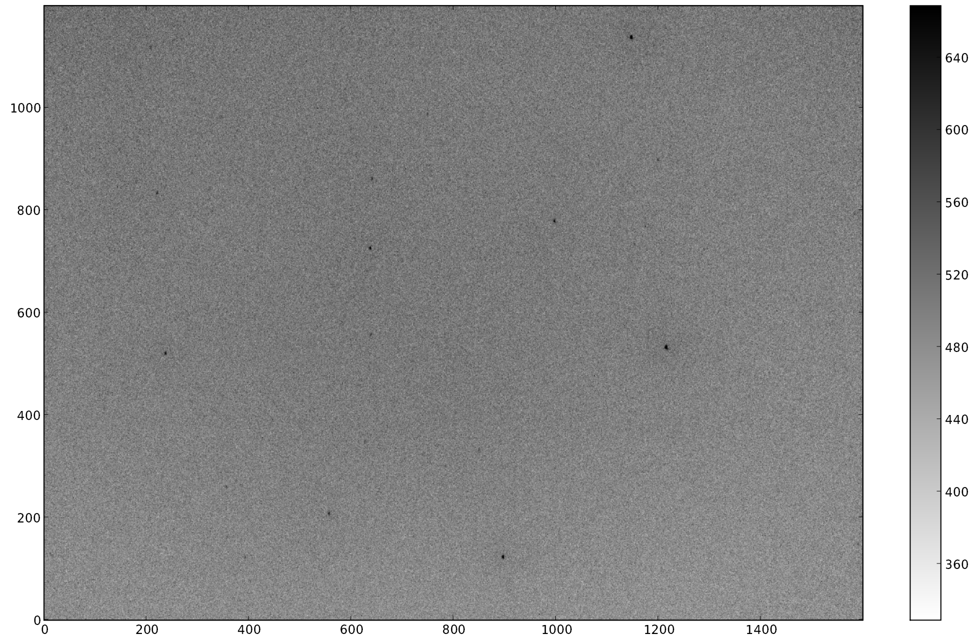

Figure 3.2: SBC camera while iced over.

The all sky camera did not suffer from the problem of icing, possibly due to the domed window on its enclosure, which discouraged the buildup of snow and ice.

3.3 Sun and Moon

The presence of the sun and the moon in the images result in a large contribution to the background sky brightness values which we will measure. Figure 3.3 shows an image from the all sky camera where the sun and the moon are both well below the horizon. In this image the stars and Milky Way are clearly identifiable.

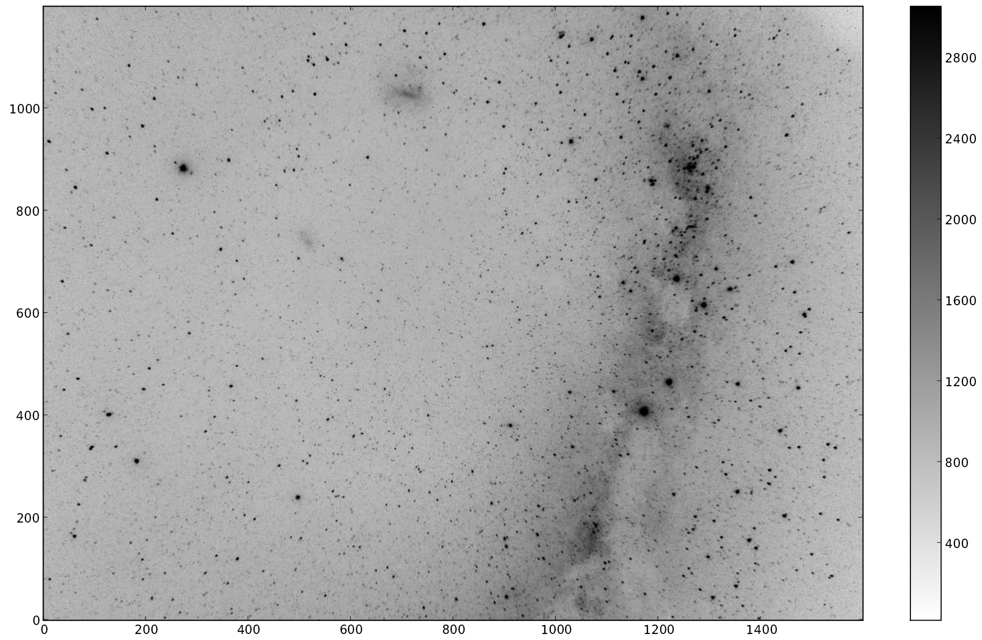

Figure 3.3: All sky camera with both the sun (−36°) and moon (−41°) well below the horizon.

In Figure 3.4 we show an image where the moon is above the horizon but the sun is below the horizon. In this image the background sky brightness is approaching that of the stars, so it becomes more difficult to identify them.

Figure 3.5 shows an image from the all sky camera when the sun is only 1.1° below the horizon. In this image the background is brighter than the stars, so there is no possibility of detecting any.

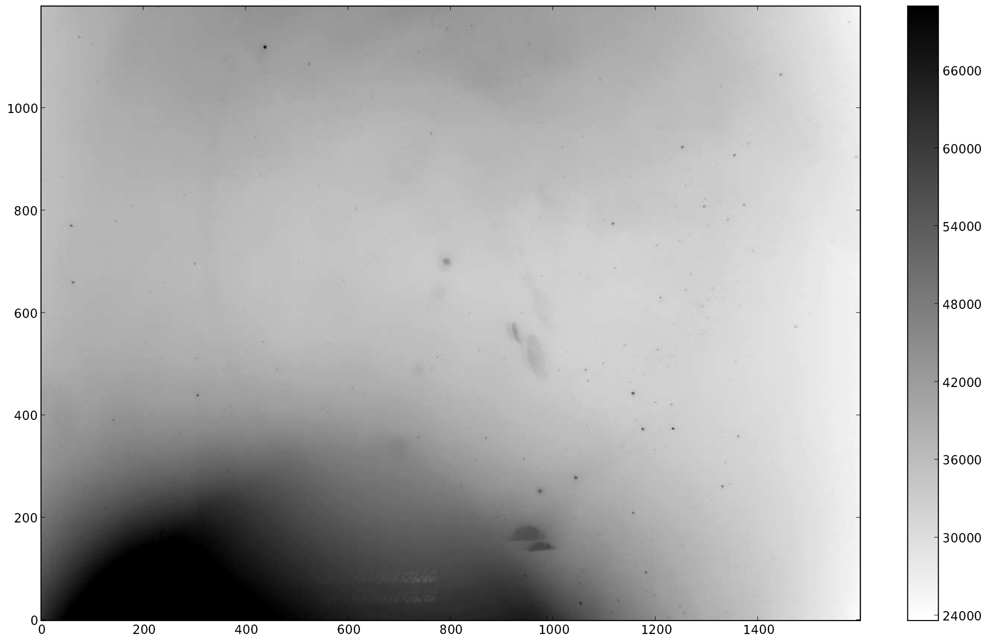

Figure 3.4: All sky camera with a lunar elevation of 42° and solar elevation of −35°.

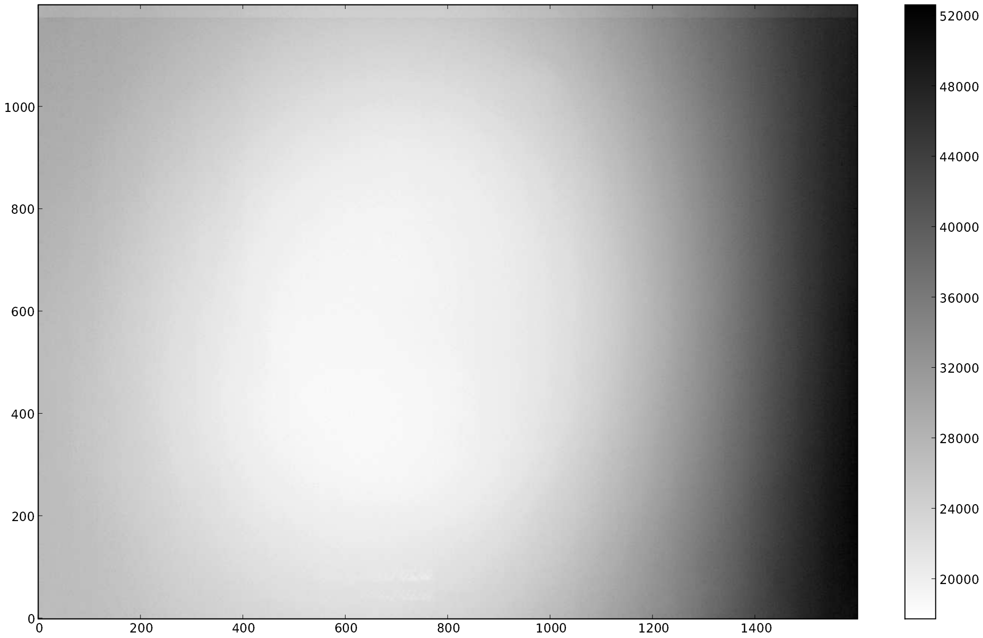

Figure 3.5: All sky camera with the sun only 1.1° below the horizon and the moon 41° below the horizon.

3.4 Bias Frames

As was described in Chapter 2, images were taken daily with a zero exposure time, which allows us to determine certain characteristics of the camera and its electronics. Figure 3.6 shows an example of a bias frame. Also shown in this image is a power vs wavelength graph, derived from the spatial FFT of the image (see Chapter 5). The wavy pattern which runs across the images proves to have a wavelength of approximately 30 pixels.

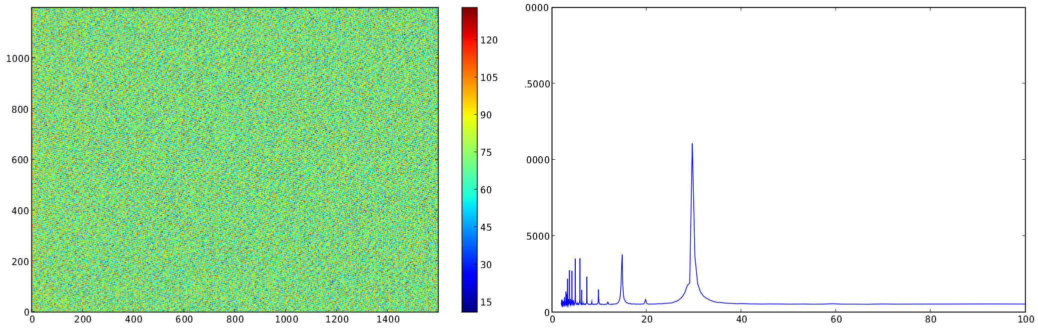

Figure 3.6: A bias frame image (left) and its power vs wavelength graph showing a 30 pixel spike (right).

3.5 Read Noise Limited Images

When the sky was sufficiently free from light from the sun and the moon, the amount of light falling on the cameras was quite low. As such the electronic noise from the camera systems could actually be detected in the image.

Figure 3.7 shows an example image in which the light from the sky is very weak. The characteristic wavy pattern seen in the bias frames above can also be seen here, and the power vs wavelength graph confirms that the pattern has a 30 pixel wavelength.

3.6 Cloud Cover

One of the aims of the all sky camera is to collect statistics about cloud cover at Dome C. Although it is not always possible to resolve the clouds, there are

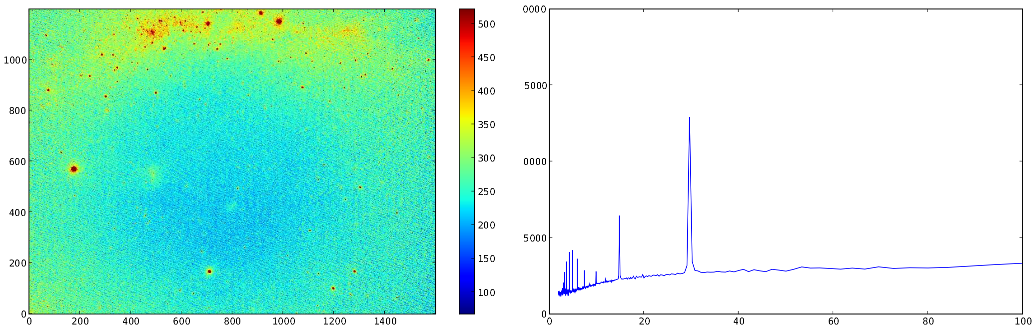

Figure 3.7: A read noise limited image (left) and its power vs wavelength graph showing a 30 pixel spike (right).

some images where the clouds are quite clear. Figure 3.8 show four images over a 20 minute period taken with the all sky camera, showing a band of clouds moving across the sky.

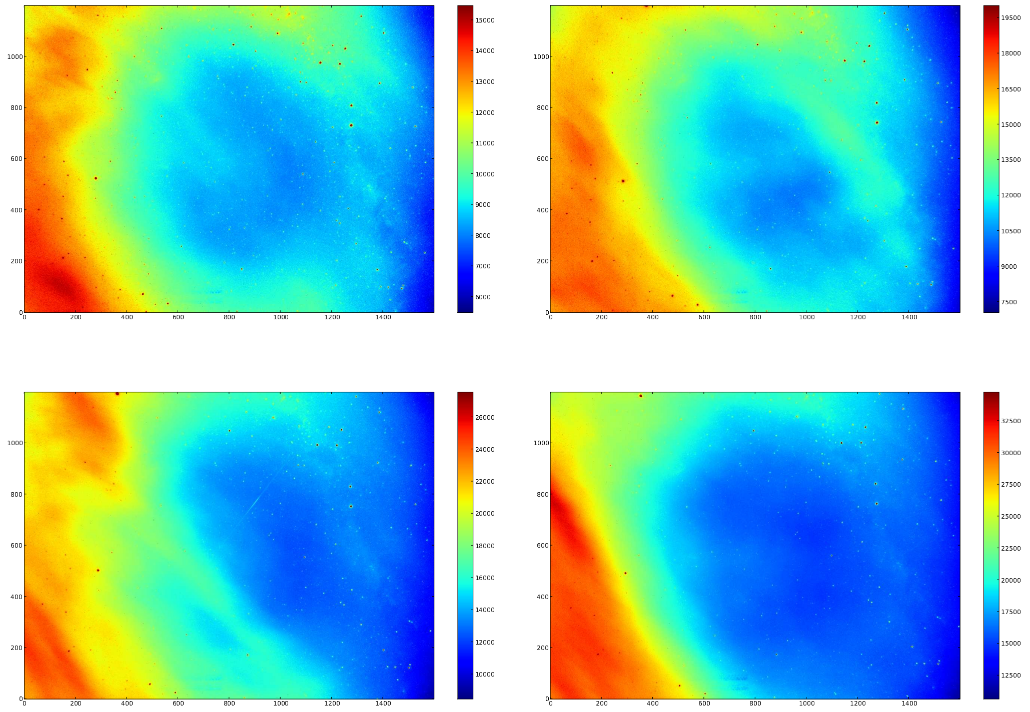

Figure 3.8: A series of images from the all sky camera showing clouds moving across the sky.

3.7 Satellite Trails

An interesting feature of many images are very clear satellite trails. These manifest themselves as bright straight lines across the image. The length of the line and the exposure time allows us to calculate the orbital velocity of the satellites.

Figure 3.9 shows examples of images with satellite trails for 8 second and 40 second exposure times respectively.

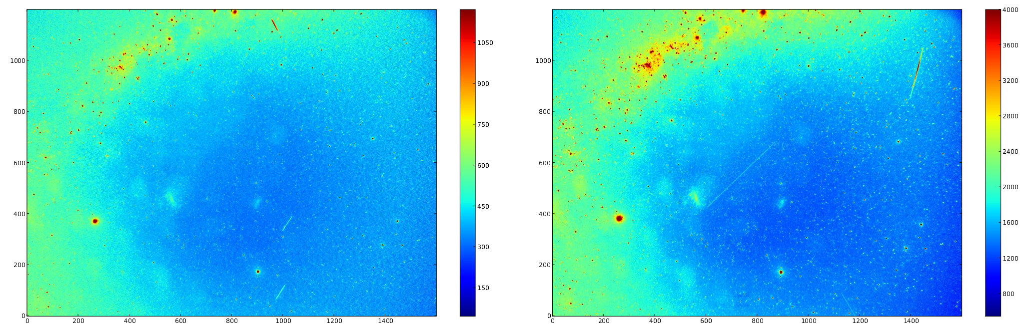

Figure 3.9: All sky camera 40 second exposure showing satellite trails.

3.8 Unidentified Images

There are some images where it is not entirely obvious what exactly is being seen. In Figure 3.10, for example, there is clearly something obscuring the image. This particular obstruction is transient in nature, as the next image taken with the camera shows a clear image. Such unidentified images provide interesting boundary cases for out image analysis tools as well as provoking the imagination of those viewing them[1].

---

[1] It has been hypothesised that the trails in Figure 3.10 are a form of space serpent, however there is no corroborating evidence of this

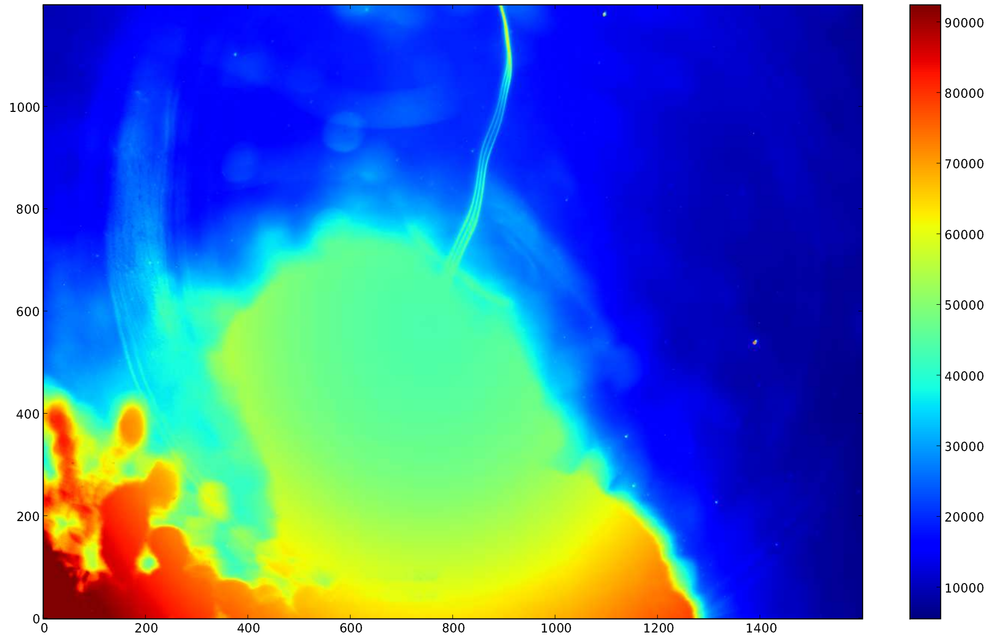

Figure 3.10: An image from the all sky camera with an unidentified obstruction.

Chapter 4

Analysis

The Gattini cameras have produced a large amount of data which required processing. In this chapter I describe the various analysis processes which were applied to the data.

4.1 Overview

The primary aim of the image analysis is to determine the background sky brightness in mag/arcsec^2. To do this we need to be able to know both the area of the sky subtended by each pixel in our image as well as the conversion scale for the image to go from pixel counts to mags.

The area of the sky subtended is a fixed value for each pixel, however the conversion scale varies between images. To calibrate the brightness scale we identify stars in each image which have a known brightness (from a published catalogue) and fix our scale against these known points. Once our brightness scale is determined for a given image, we can calculate the brightness of a particular object by taking its intensity relative to an appropriate background value and converting it according to the images brightness scale and the formulas which will be given below.

The sections below outline the steps involved in taking a raw image from the camera, applying the appropriate preprocessing, identifying the stars, calibrating the brightness scale, and measuring the background intensity.

4.2 Image Processing

To process the data from the Gattini cameras a number of individual processes had to be applied to each image in a particular order. This processing is handled by the IRAF[1] software package, which is widely used for astronomical image analysis. Each of the individual steps are described below, followed by an explanation of how the data set as a whole was handled.

Figure 4.1 shows a flow chart of the various steps involved (which will each be described below). Each step either modifies the image or its headers, writes data to the database, or possibly both.

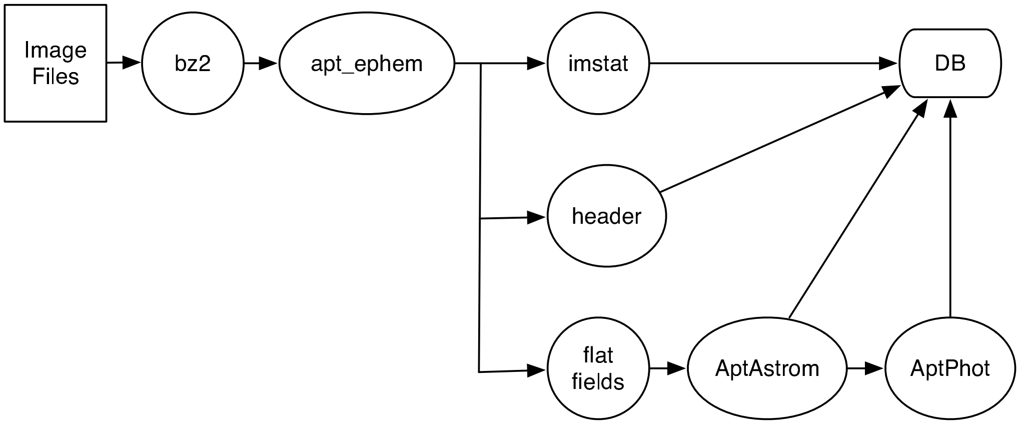

Figure 4.1: Image processing flowchart.

4.2.1 Uncompression

The first step in the image processing pipeline is to uncompress the image. This is done using the `bunzip2` program. The uncompressed image is stored on a local disk for subsequent processing.

4.2.2 `apt_ephem`

The IRAF command `apt_ephem` processes an image to determine the right ascension (RA) and declination (Dec) of the center of the image. The RA and Dec are the coordinates of a star in the celestial sphere which correspond

---

[1] http://iraf.noao.edu/

to the longitude and latitude on the terrestrial sphere. This gives an initial idea of what region of the sky is being imaged. As well as the RA and Dec, a number of other values are calculated. These values are added to the FITS header of the image. The additional header values are given in Table 4.1.

Header name	Description
RA	Right ascension (hours)
DEC	Declination (degrees)
WCSDIM	World coordinate system (WCS) number of dimensions
RADECSYS	The RA/Dec system used
CTYPE1	Type (RA or Dec) of Coordinate 1
CTYPE2	Type (RA or Dec) of Coordinate 2
CRVAL1	Right ascension (degrees)
CRVAL2	Declination (degrees)
CRPIX1	Centre pixel (x)
CRPIX2	Centre pixel (y)
CD1_1	Rotation matrix element
CD1_2	Rotation matrix element
CD2_1	Rotation matrix element
CD2_2	Rotation matrix element
DATE-OBS	UTC date of observation
AIRMASS	Airmass
LST	Local sidereal time
JD	Julian Date
MOONRA	Moon RA (radians)
MOONDEC	Moon Dec (radians)
MOONZD	The zenith distance of the moon (radians)
SUNZD	The zenith distance of the sun (radians)
MOONPHSE	The moon phase (percentage)
MOONMAG	The magnitude of the moon due to its phase
MOONDIST	The angle between the moon and the camera
EPHEMVER	The version of `apt_ephem` used

Table 4.1: Header values added to the FITS file by `apt_ephem`

4.2.3 `imstat`

The next step is to run the IRAF command `imstat`. This provides a very basic statistical description of the pixel counts in the image. The values returned are the maximum, minimum, average and standard deviation. These values are calculated and then put into the database (see Section 5.1.3).

4.2.4 Header Information

The next step is to extract the header information from the FITS files and place it in the database. This is done using the `pyfits`[2] Python package. Only those header values which are variable between the images are stored. The fields which are stored can be seen in the database schema for the table `header` in Appendix A.

4.2.5 Flat Fields

For the purposes of this analysis, the flat field frames were derived by taking the average values of all the flat images for each camera, as described in Section 2.4.4 . This process allowed us to create two flat field frames, one for each camera (Fig. 4.2). These average images were then normalised to have a total pixel sum of 1.00. This ensures that when it is combined with each image, the total pixel count of the image remains unchanged.

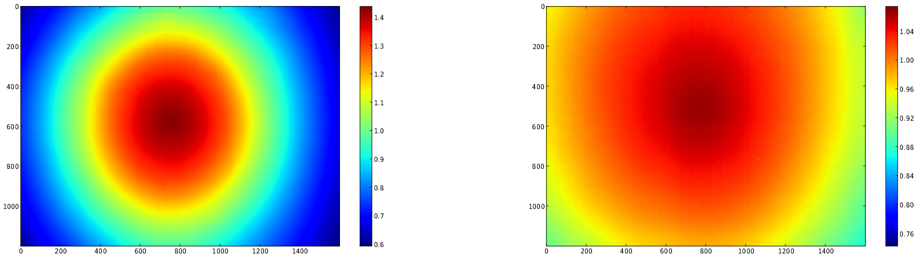

Figure 4.2: The flat field images used for the all sky camera (left) and the SBC (right).

These flat field frames were created and combined with each image using the IRAF command `imcombine`. This command provides an easy way to manipulate images by adding, dividing or applying other mathematical operators to them.

4.2.6 `AptAstrom`

The IRAF program `AptAstrom` adds astrometry information to the image headers as well as calculating some crucial magnitude parameters. The header values updated are those which define the position of the centre of the image

---

[2] http://www.stsci.edu/resources/software_hardware/pyfits

which had previously been calculated by `apt_ephem`. `AptAstrom` gives more accurate values based on the precise locations of the stars it uses in its calculations.

`AptAstrom` calls the IRAF routine `aptxymatch`, which locates stars in the image, matching them to known values in the Tycho-2 catalogue [26]. It produces three particular values, which are put into the database as `astrom.sky`, `astrom.smag` and `astrom.zmag`. These values are calculated as follows.

First, the middle 60% of pixels are taken from the middle row of the image. That is to say, pixels with an x position in the range $[320 : 1280]$. These pixel values are then sorted smallest to largest and the 30% value chosen. This provides an estimate of the background sky intensity and is stored in the database as `astrom.sky`. Figure 4.3 shows a histogram of the data used for this calculation for a particular image. The vertical line on the left is the estimated value of `astrom.sky`. The vertical line on the right shows the value of `imstat.mean`. We can see that `astrom.sky` is a much better estimator of the background sky intensity than the mean pixel value of the entire image.

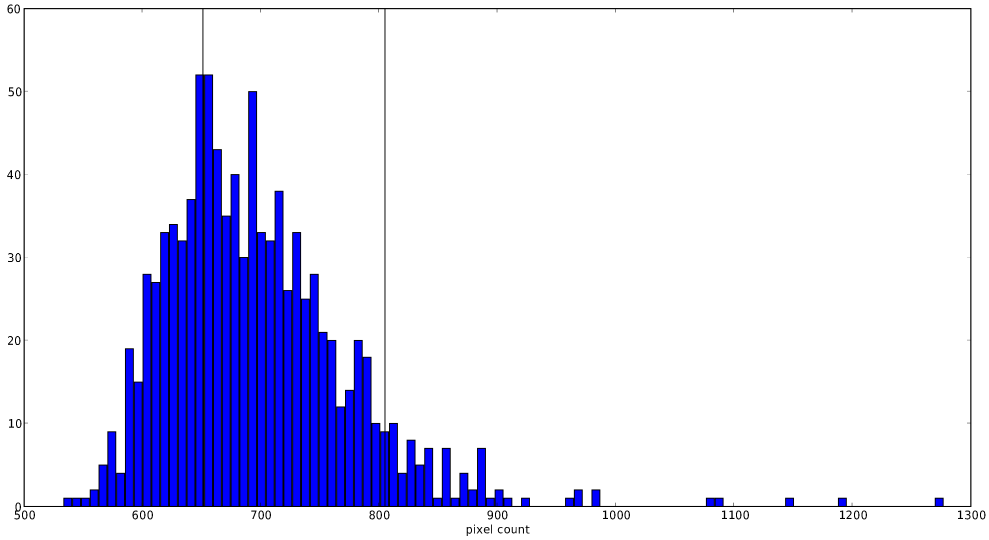

Figure 4.3: Histogram of data used to estimate `astrom.sky`.

The next step is to calculate the image's magnitude zero point, Z. This is a constant magnitude which must be added to any measured magnitudes to correctly calibrate them. An initial estimate is made as

$$
\begin{aligned}
Z_{est} &= Z_{cam} + 2.5\log_{10}(t) && (4.1)\\
Z_{cam}(SBC) &= 17.8 && (4.2)\\
Z_{cam}(Sky) &= 12.5 && (4.3)
\end{aligned}
$$

where t is the exposure time. The intensity of each star in then calculated. The pixels in a 5x5 region centered on the star are summed together to give an intensity $I_{5\times5}$. A background pixel intensity I_{bg} is then calculated as the minimum of the four pixels located at the corners of an 11x11 square centered on the star. Figure 4.4 shows these regions marked out for an example star.

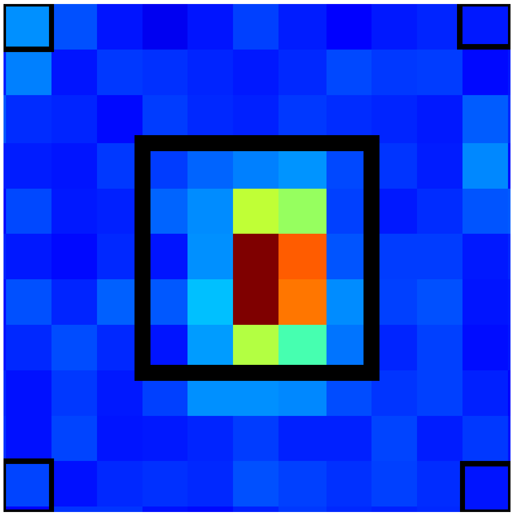

Figure 4.4: The regions used by `AptAstrom` to calculate the star intensity

Finally the star intensity is given by

$$I = I_{5\times5} - 5 * 5 * I_{bg} \qquad (4.4)$$

Combining this intensity with the estimated zero magnitude, an estimate of the actual magnitude of the star can be made.

$$M_{est} = Z_{est} - 2.5\log_{10}(I) \qquad (4.5)$$

From here the error in the estimated values with respect to the catalogue value for each star can be calculated by taking

$$\Delta M = M_{cat} - M_{est} \tag{4.6}$$

where M_{cat} is the catalogued star brightness. This value is calculated for each star and any outliers in the distribution of error values are discarded. This accounts for problems such as two stars being very close together and thus having their brightness values misestimated. The mean of these errors is then taken to give a quantity

$$S = \overline{\Delta M} \tag{4.7}$$

which is the average error in magnitude when using our initial estimation Z_{est} for the magnitude zero point. We finally define the zero point to be

$$Z = Z_{est} + S \tag{4.8}$$

The values of Z and S are returned and placed in the database as `astrom.zmag` and `astrom.smag`.

4.2.7 `AptPhot`

The IRAF routine `AptPhot` does aperture photometry on the stars which can be identified in each image, returning information about their position and magnitude. For each star the precise position is located to a subpixel accuracy. The magnitudes are then calculated for apertures of radius 3 and 4 pixels.

The method of calculating the magnitudes is as follows. Firstly the signal intensity $I_{sig}(r)$ of the pixels within the given radius r are summed. This is done with subpixel accuracy, with those pixels on the boundary of the aperture contributing an appropriate fractional amount. A background intensity I_{bg} is then determined from those pixels within an annulus of inner radius of 10 pix and outer radius of 20 pix. The histogram of the pixels within this annulus is created and the centroid value I_{bg} calculated.

Figure 4.5 shows the regions used in this calculation for an example star. The inner, dashed line, shows the $r = 3$ pixel aperture in which the signal

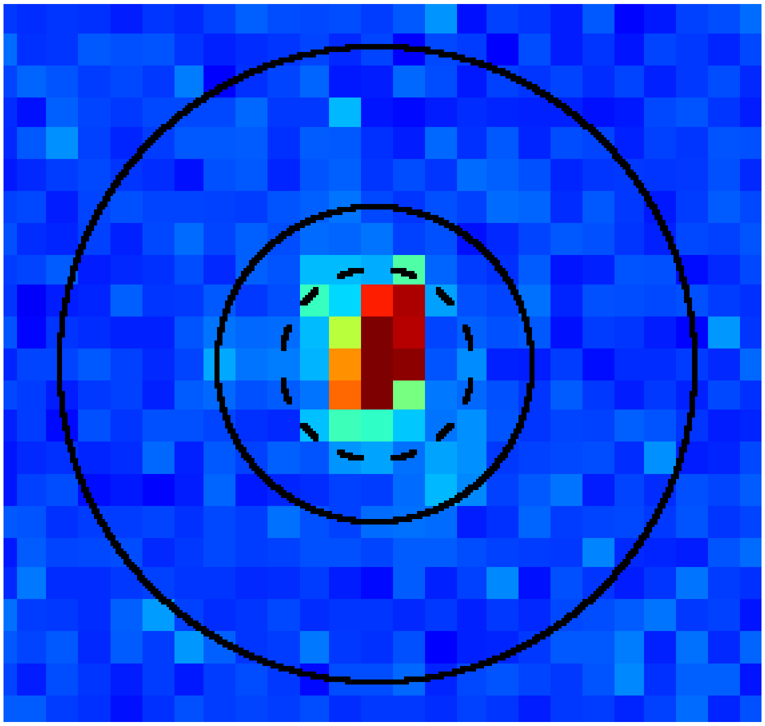

Figure 4.5: An example star showing the regions used by `AptPhot` to calculate the star's magnitude.

is integrated. The outer lines show the annulus from which the background value is calculated.

$$I(r) \quad = \quad I_{sig}(r) - A(r) I_{bg} \tag{4.9}$$

where $A(r)$ is the area of the aperture. The magnitude of the star is calculated as

$$M(r) \quad = \quad 25 - 2.5 \log_{10}(I(r)) \tag{4.10}$$

The values $M(3)$ and $M(4)$ are returned and placed in the database as the fields `phot.mag3` and `phot.mag4` respectively. The value I_{bg} is returned as `phot.smag`. It should be noted that `phot.smag` is a pixel value for the sky background in the local region of the star whereas `astrom.smag` is a measure of the error in estimated magnitude. Care should be taken not to confuse these two values.

4.3 Sky Brightness Calculations

We wish to be able to calculate the background sky brightness from the recorded images. We have an estimate of the zero point magnitude of each image, given by `astrom.zmag`. From here, the magnitude of a particular feature with a pixel count ΔI in the image can be given as

$$M = Z - 2.5\log_{10}(\Delta I) \tag{4.11}$$

This gives a magnitude in units of mag. Ideally we would like a value in units of $mag/arcsec^2$, so we must add a term given the area A of the feature. Our expression becomes

$$M = Z - 2.5\log_{10}(\Delta I) + 2.5\log_{10}(A) \tag{4.12}$$

4.4 Dark Frames

The dark frames allow us to determine the dark current of the CCD as well as identifying any hot spots on the image. The dark frames were analysed by taking a linear fit of their average pixel value to determine their dark current as a function of temperature and exposure time.

4.5 Bias Frames

The aim of the bias frames is to give us the read noise of the CCD. To analyse these images I looked at histograms of the minimum, maximum, mean and standard deviation of the pixel counts in these images. By considering the distributions of these values I was able to determine the read noise properties of each CCD.

Chapter 5

Software

The task of analysing a data set the size of that produced by the Gattini cameras requires powerful software systems. Not only is there the difficult task of processing each image, but there is also the subsequent task of examining the data produced by this image processing. In this chapter I explain the software which was developed for this thesis to address these tasks.

5.1 Image Processing Implementation

The steps described in Chapter 4 explain the individual processing steps that were applied to each image. The task of stringing all these processes together and applying them to over eighty thousand images posed a significant challenge, both logistically and computationally.

As was discussed in Chapter 2, the data set in its full, uncompressed, 32 bit form would require over 600GB of storage space. This is more than we had available to us, so any processing would require the data to never be fully expanded out at a given time. Additionally, the amount of CPU time required is quite significant. With 85740 image, if we spend 1 second processing each image, we will require very nearly 24 hours to process the entire set. As it turns out, the processing above required anywhere from 7 to 30 seconds per image, meaning a total processing time of a number of weeks is required to analyse the complete data set.

Due to the large amount of data and the long processing time required, a reasonably complex system was required to ensure that the processing happened as quickly and efficiently as possible. This involved setting up the processing scripts in such a way that the CPU could be fully utilised at all times without having to wait for data to be retrieved from the disk. It also involved designing a database in which to store the results of the processing.

5.1.1 Processing Script

Once all the processing steps from Chapter 4 had been decided on, the first step was to produce a script which could process a single image from start to finish, using minimal resources and cleaning up after itself so as to conserve disk space. This was done with a Python script which was able to interface with IRAF using the `pyraf`[1] module.

The processing script was broken into two main steps. The first step involved the basic processing, which included the steps given in Section 4.2 up to and including producing a flat field reduced image. The next was to run the photometry processes `AptAstrom` and `AptPhot`. In general most of the processing time was spent in these two routines.

The reason for breaking the processing up into these particular logical blocks was to see if the processing could be sped up by doing the first step on a series of images, followed by the photometry step on all these images. It turned out however that processing each image all the way through, rather than piecewise in groups, was faster overall. This was possibly due to disk caching and locality issues[2], however this was not investigated in depth.

The final step in processing a single image was to clean up any files that had been created during the processing. By doing this the processing could run over the entire data set without requiring massive storage overheads. The disadvantage with this approach is that tasks such as flat fielding must be repeated at later stages when we want to visually examine individual images.

5.1.2 Client-server Model

To help facilitate maximum usage of the available resources on the processing machine, and also as a precursor to a more flexible analysis system, a client-server model processing system was implemented. The server process acted as

---

[1] http://www.stsci.edu/resources/software_hardware/pyraf

[2] The principal of locality says the the data most likely to be needed by the processor is that closest on the disk to the data currently being processed. As such processors and disks are optimized for this case. By processing each individual image all at once we can make the most of these optimizations.

a simple job control and queuing daemon, handing out the IDs of the images which required processing to any client which asked for an image to process.

The clients and server communicated using a very simple text based protocol sent over TCP. The protocol was client initiated and consisted of three simple commands: `ADD`, `GET` and `STOP`.

The syntax for the `ADD` command was simply `ADD image_id`. This would tell the server to put the given image ID in the queue to be processed.

The `GET` command had no additional parameters and requested an image ID from the server to be processed. The server would reply with either an image ID or the string `EMPTY` which would indicate that there were no images left in its queue.

The `STOP` command was used to shut down the server. Any jobs left in the server queue would not be processed and the server process would terminate.

Running the analysis in a client-server model made the processing easier in a number of respects. The first was that it maximised the use of the available resources on the processing machine (e.g. CPU, memory, IO bandwidth, etc). Due to the large amount of data involved, the CPU would spend a lot of time idle while data was retrieved from the disk if there was only one process running. By having multiple processing running, some could be using the CPU while others retrieved their data from the disk. Constant monitoring of the processing showed that the optimal number of concurrent clients was around four or five. Any more than that and they would start getting in each others' way, causing slow downs due to swapping, cache misses, etc.

The next benefit was that it simplified the task of keeping track of which images needed processing. If we had multiple processing clients running, each with an individual list of images to process, the task of keeping track of which client was processing which data, and what data still needed to be processed would become unmanageable. In particular, in the event of a client terminating unexpectedly (as would happen occasionally, for a number of different reasons discussed in Chapter 7), it would be difficult to know which set of images needed to be restarted and from where. In the client-server model, the server process (which rarely terminated unexpectedly) was able to keep track of the images to be processed, and a client dropping out would not have an effect on the continued processing of the data set as a whole.

The other benefit of a client-server model, which is yet to be realised for this system, is that it allows the processing to be distributed among multiple machines, which could potentially speed up the processing time by a significant factor. There is still some work required to make this processing system fully distributable. In particular, the issue of distributing the data to be analysed, however if this data, or subsequent data sets need to be analysed again it would most likely be worth the effort to reduce the processing time from a number of weeks to days or possibly hours by taking advantage of otherwise idle machines on the network.

5.1.3 Database Design

The processing described above produces a large amount of data describing the images themselves and also the stars identified within them. To manage all this data, a database was designed to provide an easy way to store the results and to subsequently examine them. The database is implemented using the MySQL[3] relational database management system with the server running on the machine `mcba11.phys.unsw.edu.au`.

The Gattini Database (GDB) contains information related to three main classes of object; cameras, images and stars. Individual objects in each of these classes are assigned unique IDs which are used as indexes on which the various tables can be joined. The complete schema for the GDB can be found in Appendix A. The following gives a brief overview of each of the tables and the data stored in them.

`astrom:` This table stores the results of the `AptAstrom` program for each image. In particular this holds the values of `sky`, `smag` and `zmag` described in Section 4.2.6.

`cam:` This table holds a mapping between the internally used camera IDs and the camera names.

`flat:` The name of the file used to flat field correct each image and the name of the resulting file are stored in this table[4].

---

[3] http://www.mysql.com/

[4] The data in the database is affected by a bug which caused only the base path of the flat file used to be stored, leaving off the filename itself. This did not cause a problem in the course of this thesis but should be addressed before processing another data set

`header:` This table contains the values for each of the header fields from each image as described in Section 4.2.4.

`image:` This table maps a unique ID to each image in the original data set and stores the filename, camera ID and image time.

`imstat:` The basic statistical values calculated by the routine `imstat`, as described in Section 4.2.3, are stored in this table.

`phot:` The results of the photometry processing done by `AptPhot` are stored in this table. Each row contains the image ID and star ID of the identified star as well as (x, y) pixel coordinates and the magnitude values outlined in Section 4.2.7.

`star:` This table stores the catalogue ID and the RA and Dec of each star which has been identified by `AptPhot`. It also assigns each catalogue star a unique ID (separate to its catalogue ID) to be used as the database index.

`starcount:` The number of stars found by `AptPhot` in each image is stored in this table.

`unzip:` This table keeps track of whether each image was successfully uncompressed and the name of the resulting file.

5.2 Gattini Data Explorer

The result of the above processing was a database with a large number of variables and a staggering amount of data (over 22 million stars and 80 thousand images). The task of exploring all this data and obtaining useful results required a tool to visually present the data in a flexible and practical manner. To this end a database browser was designed and implemented which allowed for the values in the database to be plotted and charted in various different ways.

The Gattini Data Explorer (GDE) is an application which allows the user to plot the data of interest using a number of different modalities. Figure 5.1

shows the GDE in action. Different plotting modalities can be selected from the different tabs while the toolbar across the top allows the user to select the various plotting parameters. The various functionalities available provide both flexible and powerful data exploration and plotting capabilities which have been crucial to investigating the results in this thesis. The software is designed in such a way as to be easily extensible in the future. New tabs may be added, or existing tabs extended to give more features as required.

The GDE is written in Python and makes extensive use of the `pygtk`[5] bindings to GTK+[6] as well as the Matplotlib[7] plotting library. At present the GDB has some rather strict dependencies which must be met in order for it to run. As well as needing access to all the appropriate software libraries, it must also have access to the original Gattini image files and the GDB. As such it can only be run on `mcba11.phys.unsw.edu.au` at present, however it may be worth exploring the possibilities of removing some of these dependencies in the future so that it may be more widely used within the research group.

As well as producing a wide variety of plots, the GDE is able to take advantage of Matplotlib's capabilities to allow the user to interact with the image. A toolbar at the bottom of each of the plot (Fig. 5.2) allows the user to pan and zoom around the images to focus on detail of interest. Additionally, there is a save image button which allows the image to be saved to disk in any of a number of formats including `.png` and `.eps`.

5.2.1 Data Model

To describe the various functionalities of the GDE we must first define the different types of data that it needs to handle. There are three main types of data involved; *per image data*, *per star data* and *individual images*. Per image data consists of those fields from the database (and values derived from these) which have a single value for each image. These include things such as the time, the sun elevation, the the maximum pixel value, etc. Per star data consists of those fields (or derived values) which have a single value in each image for a given star. For example, if we pick a star s and take its x position on the image for a series of images, these values would constitute a per star data set. The final type of data is the individual image. The 1600x1200 pixel values and the associated headers of an image constitute a data set which we would like to be able to explore.

---

[5] http://www.pygtk.org/

[6] http://www.gtk.org/

[7] http://matplotlib.sourceforge.net/

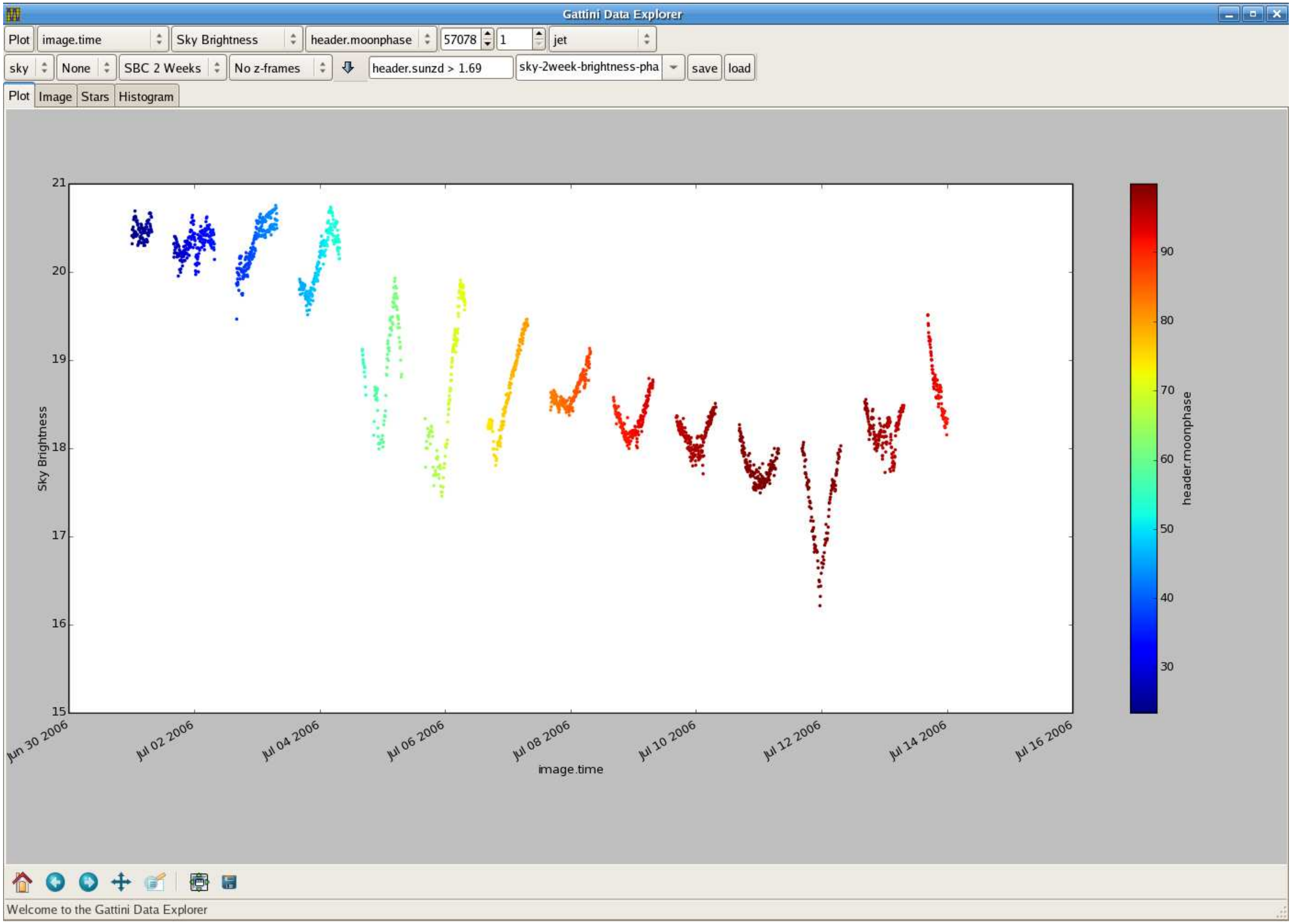

Gattini Data Explorer

Plot | image.time | Sky Brightness | header.moonphase | 57078 | 1 | jet

sky | None | SBC 2 Weeks | No z-frames | header.sunzd > 1.69 | sky-2week-brightness-pha | save | load

Welcome to the Gattini Data Explorer

Figure 5.1: The Gattini Data Explorer in action.

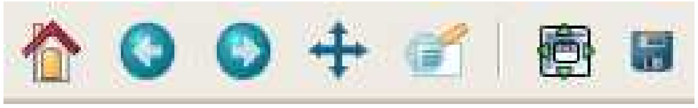

Figure 5.2: The Matplotlib toolbar, which is present on each plot.

Table 5.1. shows the database fields and their derived values which are considered per image fields and per star fields. The descriptions of each of these fields are given in Chapter 4.

Per image fields	**Per star fields**
image.time	phot.X
astrom.sky	phot.Y
astrom.smag	phot.vmag
astrom.zmag	phot.smag
header.ra	phot.mag3
header.decl	phot.mag4
header.crval1	phot.err3
header.crval2	phot.err4
header.lst	Star Brightness
header.moondist	Star Brightness Error
header.moonmag	
header.moonphase	
header.moonzd	
header.sunzd	
header.temp	
header.exposure	
imstat.max	
imstat.mean	
imstat.min	
imstat.stddev	
starcount.nstars	
Sky Brightness	

Table 5.1: The database fields and derived values which are considered per image fields and per star fields.

5.2.2 The Toolbar

At the top of the GDE window is a toolbar with two rows of controls, which allows the user to control the different aspects of the data being plotted (Fig.

5.3.). The first item on the first row of the toolbar is the plotting button. When clicked this button causes the program to obtain the required data from the database and plot it in the selected style.

Figure 5.3: The GDE toolbar.

Database Fields

The next three drop down boxes in the first row allow the user to select which fields from the database to use for the x axis, the y axis and the colour scale of the scatter plots. The database fields available for plotting are described below and depend on which tab is being used. The ability to map the colour of the scatter markers to values in the database provides a crucial third dimension which can give many insights when viewing the data.

Image and Star Selectors

Certain plotting modalities allow the user to plot results for a particular image or star. The toolbar has two numerical selectors which allow the user to specify the database IDs of the image and/or the star of interest.

Colourmap Selector

The final item on the first row of the toolbar is a drop down list of available colourmaps. The user is able to choose from any of the colourmaps available in Matplotlib. When plots are generated, the colourmap scale is present as a colour bar on the right hand side of the image.

Filters

The first set of items on the second row of the toolbar provide a number of different ways for the user to filter the results before they are displayed. The first 4 toolbar items are drop down boxes which allow the user to select the camera, the image exposure time, date range and whether or not to include bias frames (z-frames). Table 5.2. presents the different values which each of these filters can take on. It should be noted that the available date ranges are flexible in the sense that they can easily be changed or added to in the source code. The possible values of the other filters are fixed by the data.

Camera	**Exposure Time (s)**	**Date Range**	**Z-frames**
SBC	None	All	No z-frames
Sky	40	April	only z-frames
	10	May	all
	8	June	
	5	July	
	4	August	
	2	September	
	1	October	
	0.8	April+	
	0.5	SBC 2 Weeks	
	0.4		
	0.2		
	0.1		
	0.05		
	0.005		
	0.002		
	0		

Table 5.2: The particular values which each of the filter selectors can take.

As well as having these criteria selectable from their drop down boxes, there is also a text entry box which allow the user to add custom conditions to their plot. The syntactic form of these custom conditions is identical to that of the condition of the `WHERE` clause in an SQL statement[8]. These conditions can be based on any field related to the image, not just those available to be plotted.

A history of custom queries is kept so that when plotting subsequent images the user can access filters which have been previously used. This history is in the form of a drop down list of previously used filters, each of which has a check box which can be selected (Fig. 5.4). All those filters selected are applied to the plot being generated. This both saves time on entering common filters and also ensures consistency between the filters used for different plots by reducing the scope for human error.

It should be noted that the implementation of the custom condition feature assumes a knowledgeable, non-malicious user. No checks are performed to

---

[8] http://dev.mysql.com/doc/refman/5.0/en/select.html

☑ astrom.sky > 0
☐ starcount.nstars > 0
☑ header.sunzd > 1.8
☐ header.sunzd > 1.69

Figure 5.4: The drop down list of previously used filters with some selected.

ensure correct syntax or that the generated query does not in some way modify the data.

Image Save/Load Controls

The final set of controls on the toolbar consist of a mechanism to load and save the plots and the parameters used to generate them. A drop down text entry box allows the user to either enter a new name to save the image under or select from a list of previously saved plots. A `save` button allows the user to save the current plot and its parameters while a `load` button allows the user to load the selected plot parameters.

As an added feature the `save` button also generates an `.eps` file of the image. All plots and images in this thesis have been generated with this feature.

5.2.3 The Plotting Tab

The plotting tab (Fig. 5.1.) allows the user to plot any two per-image fields against each other, with the colour scale of the markers representing a third field. The results are plotted as a scatter plot, where each point represents the value for a single image. By clicking on a given point (which represents a single image), the user can set the value of the image ID selector on the toolbar, which can in turn be used to plot that image in the image tab (described below). In this way, when an interesting point is found in a plot, the origin of the data can be further investigated.

5.2.4 The Image Tab

The image tab (Fig. 5.5) allows the user to display the image data in various ways. The image to be displayed is selected by the value of the image ID selector on the toolbar (which may have had its value set by clicking on an image in the plotting or star tabs). Once the image is selected its header data is presented in a table on the left hand side of the window (Fig. 5.6) and the appropriate visualisation is displayed.

When using the image tab, there are no database fields to be selected and no filtering to be applied, so these items on the toolbar have no effect on the images plotted. Only the star and image ID selectors and the colourmap selector are used.

The visualisation method to use is selected from a list of possible options, which present the data in different ways (Fig. 5.7). The first of these methods simply displays the currently selected image in its post flat-fielding form. The colour scale used is linear, so to ensure a reasonable contrast level the image values are clipped at a very generous six standard deviations. This removes any unusually saturated pixels while still maintaining a maximum level of detail.

As well as showing the flat fielded image, the user can also select an option to only show the raw image. This gives the original image as it was taken with the camera. This provides an easy way to check what effect applying the flat fields had.

The next visualisation method allows the user to mark a single star in the image. The current star ID is taken from the toolbar and, if found in the current image, marked with a blue circular marker (Fig. 5.8). This allows the user to easily see where in the sky a particular star lies, with relation to other bodies, such as the moon or the Milky Way.

As well as being able to mark a single star in the image, there is also an option to mark all the stars, with each star being overlaid with a blue circular marker (Fig. 5.9). This feature can let the user see if there are certain stars visible in the image which have not been detected by the analysis software.

The above methods share a feature which allows the user to set the current star ID in the toolbar by clicking on a star in the image. When a click is made on the image, the location of all the identified stars in the image is retrieved from the database and the one closest to the point of the click is selected. This allows the user to pick a particular star from an image and then view its properties in the star tab.

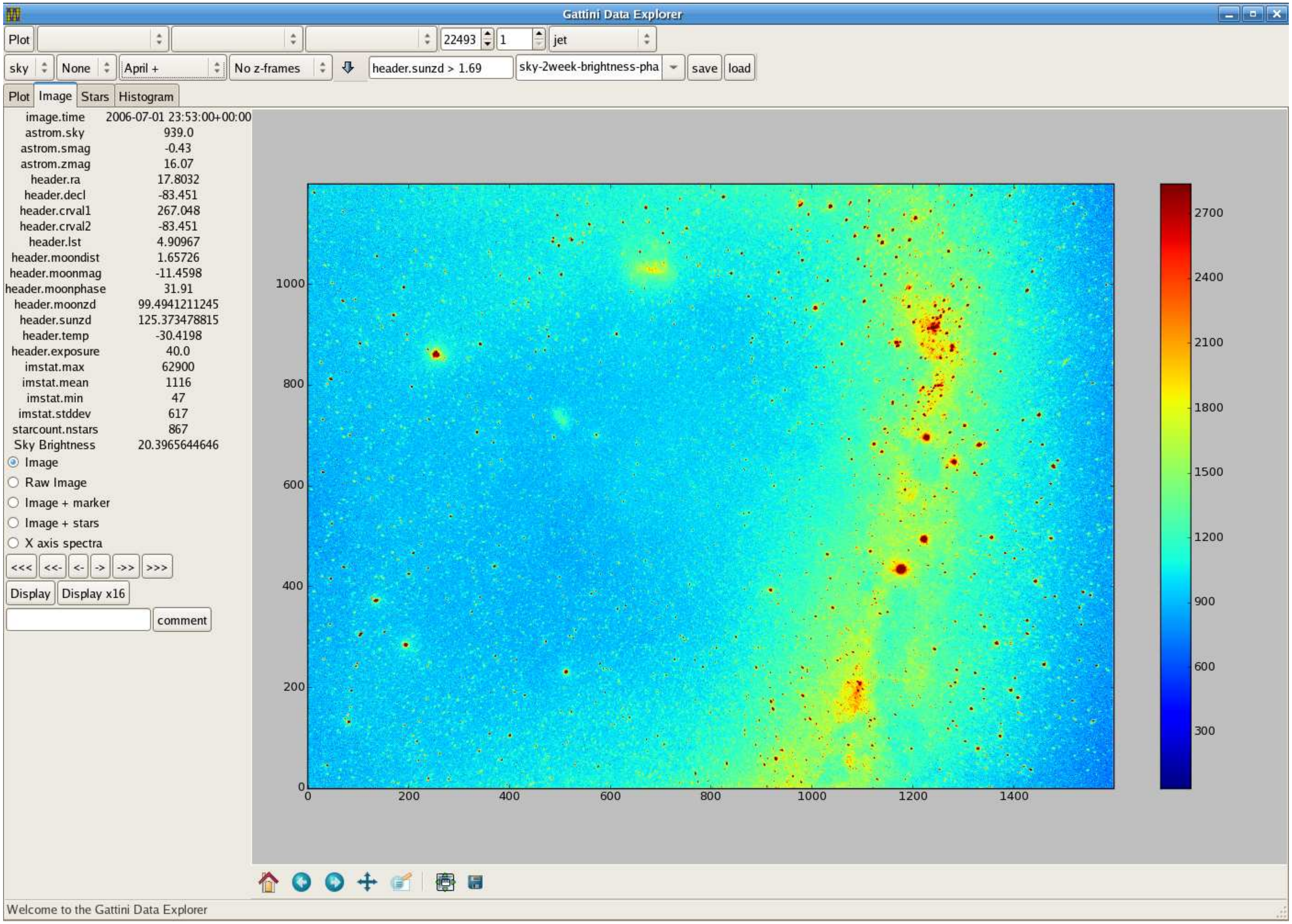

image.time	2006-07-01 23:53:00+00:00
astrom.sky	939.0
astrom.smag	-0.43
astrom.zmag	16.07
header.ra	17.8032
header.decl	-83.451
header.crval1	267.048
header.crval2	-83.451
header.lst	4.90967
header.moondist	1.65726
header.moonmag	-11.4598
header.moonphase	31.91
header.moonzd	99.4941211245
header.sunzd	125.373478815
header.temp	-30.4198
header.exposure	40.0
imstat.max	62900
imstat.mean	1116
imstat.min	47
imstat.stddev	617
starcount.nstars	867
Sky Brightness	20.3965644646

Figure 5.5: The GDE image tab.

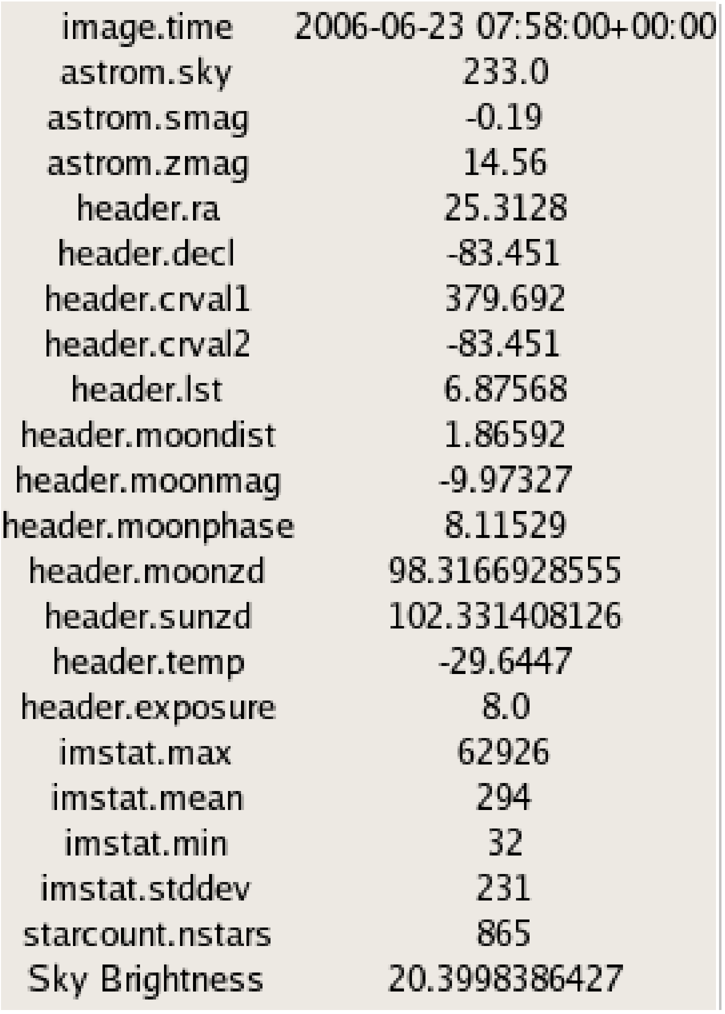

image.time	2006-06-23 07:58:00+00:00
astrom.sky	233.0
astrom.smag	-0.19
astrom.zmag	14.56
header.ra	25.3128
header.decl	-83.451
header.crval1	379.692
header.crval2	-83.451
header.lst	6.87568
header.moondist	1.86592
header.moonmag	-9.97327
header.moonphase	8.11529
header.moonzd	98.3166928555
header.sunzd	102.331408126
header.temp	-29.6447
header.exposure	8.0
imstat.max	62926
imstat.mean	294
imstat.min	32
imstat.stddev	231
starcount.nstars	865
Sky Brightness	20.3998386427

Figure 5.6: The header data presented in the side panel of the image tab.

● Image
○ Raw Image
○ Image + marker
○ Image + stars
○ X axis spectra

Figure 5.7: The plotting options available from the image tab.

Plotting the image as a whole is not the only possibility in the image tab. Another type of plot which was found to be useful was a spatial Fourier transform across the image (Fig. 5.10). This plot takes each row of the image and

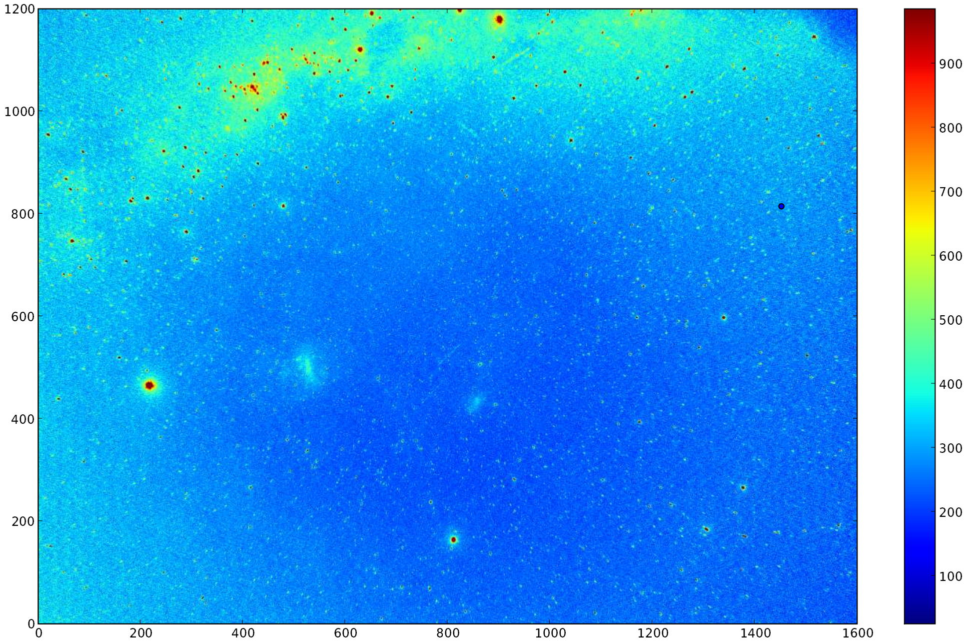

Figure 5.8: An image with a single star marked.

applies a fast Fourier transform (FFT) of the pixel values. The FFTs for each row are then averaged together to give the power as a function of spatial frequency. This is then converted to a function of spatial distance and plotted as the power vs wavelength (in pixels). This feature allows us to observe certain characteristic features of some images, as discussed in Chapter 6.

One of the design points of the GDE is that it is easily extensible. In the case of the image tab, this extensibility allows for the simple addition of new visualisation methods. To add a new routine the user has only to define a function which takes a 1600x1200 array as input, processes this data in some way, and plots the desired results. Once this function is defined, its name can be added to the list of existing methods and it will become available to use.

As well as being able to select the image using the toolbar's image ID selector, the user can also skip between images with a single mouse click using a set of buttons on the left hand side of the window (Fig. 5.11). These buttons allow the user to skip either forwards or backwards through the images by either 1, 10 or 50 images at a time. This provides an easy way to look at a series of images over a time period in a very simple manner.

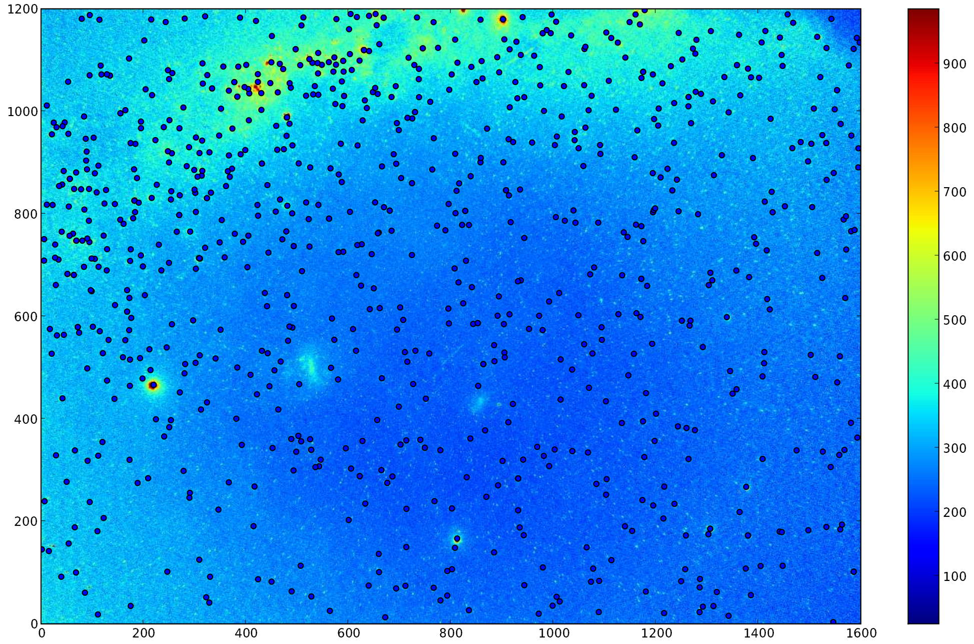

Figure 5.9: The same image with all identified stars marked.

The left hand panel also has a place for the user to enter short comments about the image they are observing (Fig. 5.12). When the `comment` button is clicked, the comment in the text box is saved to a file along with the image ID. This file can later be reviewed to come back to images of interest.

The final feature of the image tab is a pair of buttons which allow the use to open the current image using the ds9 [27] image viewer. ds9 is a very feature complete image viewer which can often give the user a better view of the image than that provided by the GDE. The two buttons available are labeled `Display` and `Display x16` (Fig. 5.13). The first button will open up just the currently selected image. The second button opens up the 16 images closest in time to the currently selected image, which allows the user to scroll through images from a given time period in the ds9 viewer.

5.2.5 The Star Tab

Data for a given star can be displayed in the star tab (Fig. 5.14). Stars are identified by their database IDs and selected using the toolbar's star ID

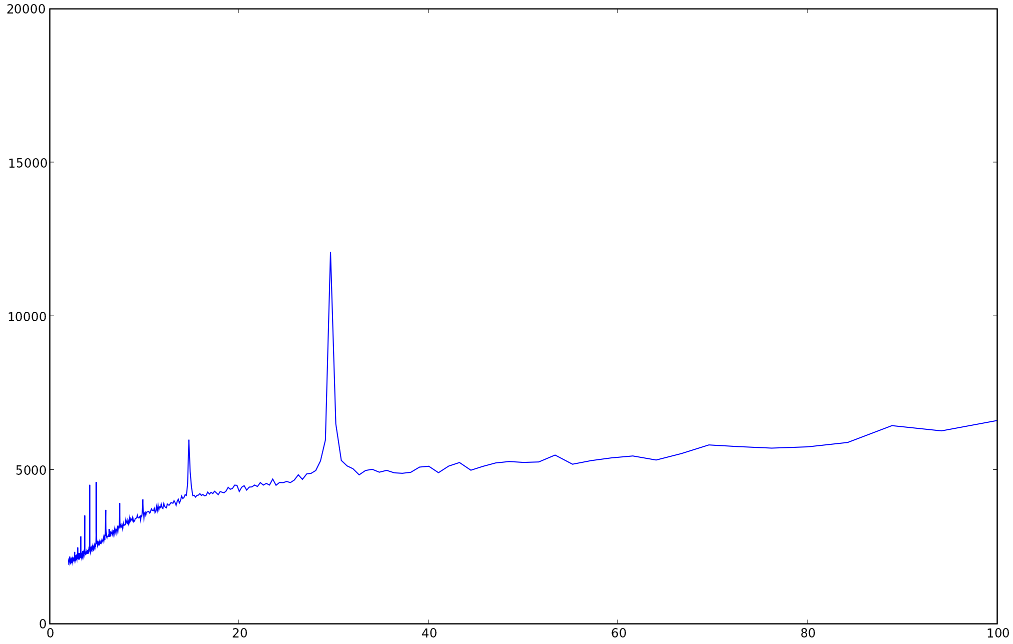

Figure 5.10: An example x axis spectra, showing a distinct peak at 30 pixels.

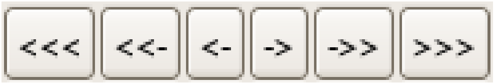

Figure 5.11: The image tab buttons which allow quick scrolling between images.

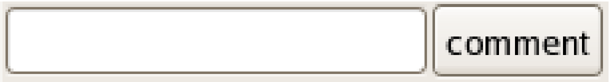

Figure 5.12: The comment entry box and button on the image tab.

Figure 5.13: The buttons on the image tab which allow the image to be displayed in ds9.

selector.

As with the image tab, there is a set of buttons which allow the user to

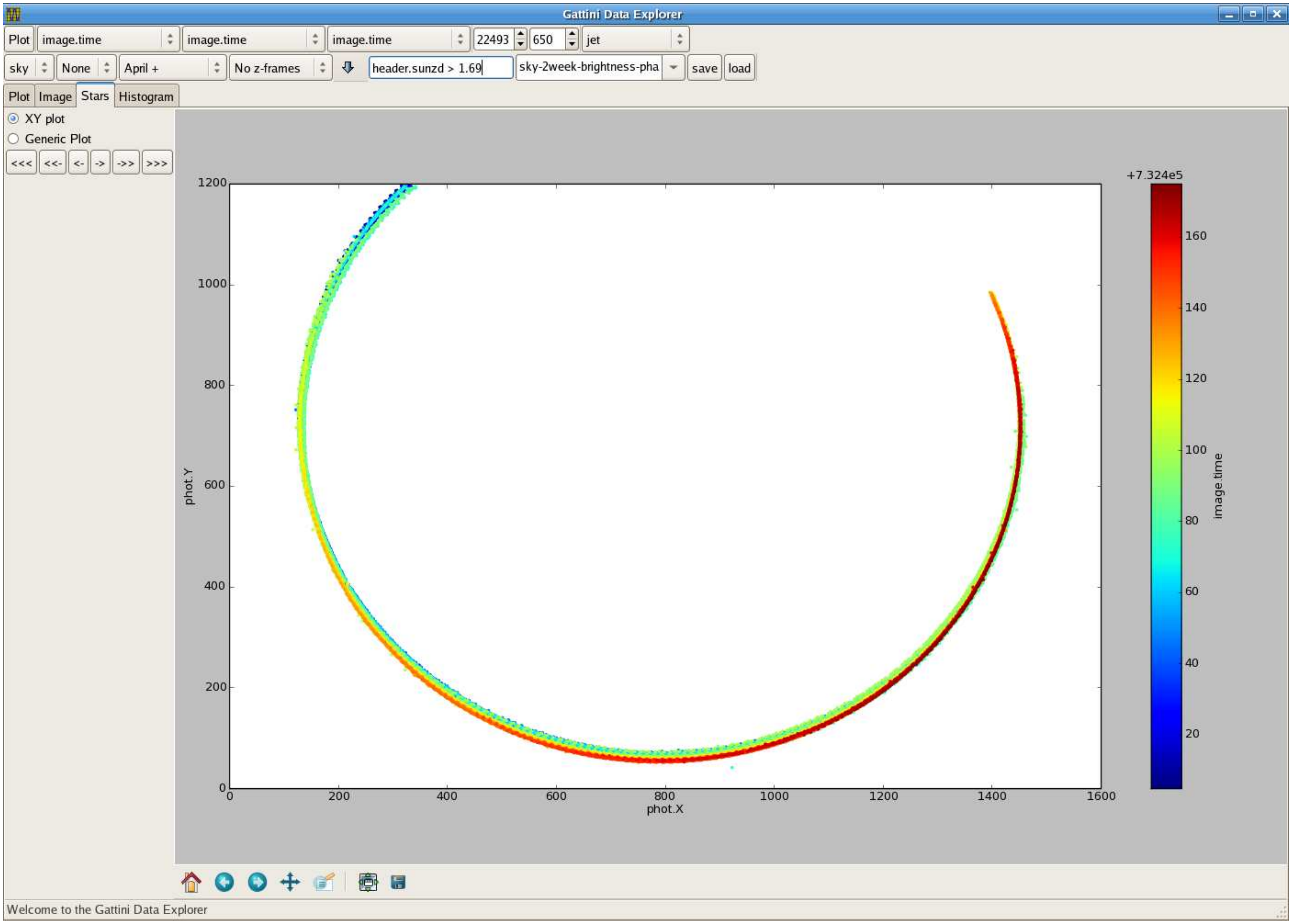

header.sunzd > 1.69

Welcome to the Gattini Data Explorer

Figure 5.14: The GDE star tab.

increment or decrement the star ID by 1, 10 or 50 and then plot the new star's data with a single click.

The user is able to pick from two plotting modes in the star tab (Fig. 5.15) (although as with the image tab, new methods can easily be added). The first plotting mode plots the position of the given star (in (x, y) pixel coordinates) in the images defined by the filters (Fig. 5.14). This allows the user to see the locus defined by the star as it traverses the sky over selected the time period. By selecting an appropriate field for the colour scale the user can see how this field varies for the star across different locations in the sky and on the image.

● XY plot
○ Generic Plot

Figure 5.15: The plotting options available from the star tab.

The second mode allows a more general set of plots to be created. Each plot is a scatter plot where each points represents an image in which the selected star was identified. These images can be further filtered using the filter options on the toolbar. The fields which are plotted for the x, y and colour axes can be any of either the per image fields or the per star fields.

5.2.6 The Histogram Tab

The histogram tab allows for histograms to be produced in a number of different useful combinations (Fig. 5.16). When plotting histograms the user can control the upper and lower bounds on the x axis and also the number of bins used. In this tab the left hand panel has a list of different types of histograms which can be generated as well as certain controls (Fig. 5.17). The first row of controls has two number selectors which control the upper and lower bounds of the image as well as a button which allows these bounds to be applied once chosen. The next row contains a number selector which controls the number of bins to use.

When a histogram is first plotted the number of bins is taken from the bin controller, but the upper and lower bounds are defined by the range of the data. The values of the bounds controllers are set to the bounds of the data. The user can then adjust these bounds and replot the histogram using the button mentioned above. Using the plot button on the main toolbar will cause the histogram to be plotted using the bounds of the data.

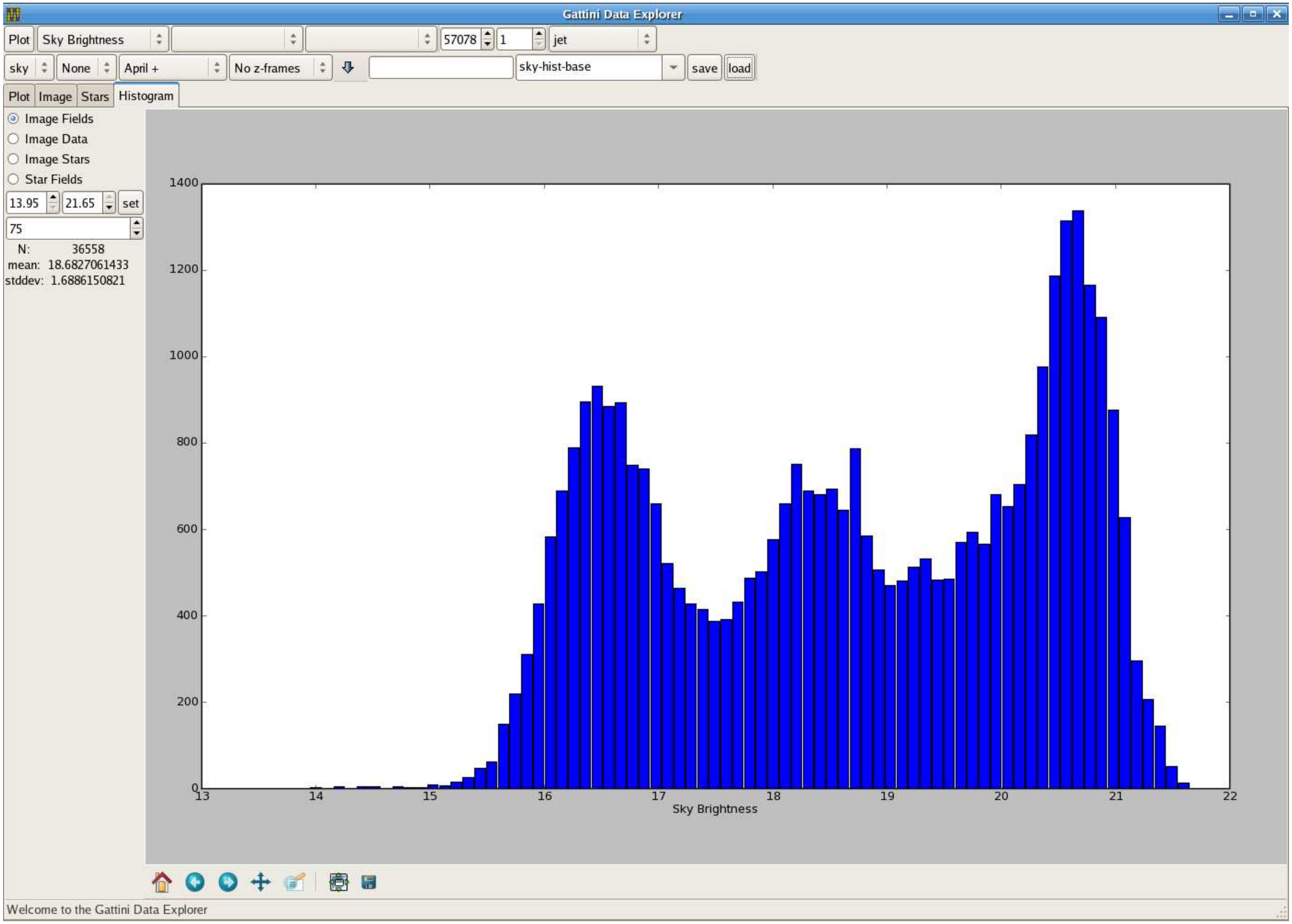

Gattini Data Explorer

Plot | Sky Brightness | 57078 | 1 | jet

sky | None | April + | No z-frames | sky-hist-base

○ Image Fields (selected)

13.95 | 21.65

75

N: 36558

mean: 18.6827061433

stddev: 1.6886150821

Welcome to the Gattini Data Explorer

Figure 5.16: The GDE histogram tab.

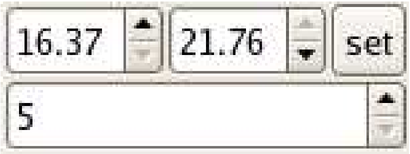

16.37 21.76 set

5

Figure 5.17: The histogram controls for setting the upper and lower bounds and also the number of bins used.

There are a number of different types of histograms which can be generated (Fig. 5.18). Each of these allows different conditions to be used when plotting. The database fields available to be plotted depend on the type of histogram as described below.

● Image Fields
○ Image Data
○ Image Stars
○ Star Fields

Figure 5.18: The plotting options available from the histogram tab.

The histogram also provides a basic statistical description of the data being presented. The number of data point, the mean and the standard deviation are all presented in the left hand panel for each plot (Fig. 5.19).

N: 36558
mean: 18.6827061433
stddev: 1.6886150821

Figure 5.19: The basic statistical description provided for the data being plotted.

Image Fields

When plotting image fields all images which match the filter criteria are used and the appropriate per image field is the variable which is plotted.

Image Data

The image data histogram uses the pixel values of the selected image as the data to plot. This provides a simple way to check the distribution of pixel counts in each image. The image plotted is taken from the image ID selector.

Image Stars

The image stars histogram looks at the per star fields for all of the stars identified in a particular image. This allows the user to see the distribution of photometry values in a given image.

Star Fields

As with the star tab, this histogram option allows a histogram of any per image or per star field, for those images where the selected star was detected.

Chapter 6

Results

The analysis of the Gattini images produced a large number of interesting results. The ability to explore the available data from so many different points of views with the GDE meant that the patterns in the data could easily be identified and accounted for. In this chapter I present the most interesting results that were found.

6.1 Bias Frames

The bias frames, which were taken daily with a zero second exposure time, must be examined first as they provide a baseline of noise in all subsequent data. Figures 6.1, 6.2 and 6.3 show histograms of the mean pixel count, the maximum pixel count and the standard deviation in pixel count for the bias frames from both cameras. These values were taken from the full 1600x1200 set of pixels in each image. The histograms represent all the bias frames taken from April 1 onwards (for reasons to be discussed in section 6.4).

The interesting thing to note from these figures is that while the mean and maximum values vary over a reasonably large range, the standard deviation is very stable, taking on only 7 discrete values for the all sky camera and 6 for the SBC. These results indicate that while the bias level may vary from frame to frame, the read out noise, given by the standard deviation, is very consistent. For the all sky camera the noise level is between 18 and 24 pixel counts and for the SBC it is between 14 and 19 pixel counts. It is curious that the range of error values between the two cameras is almost disjoint, as the CCDs are nominally identical.

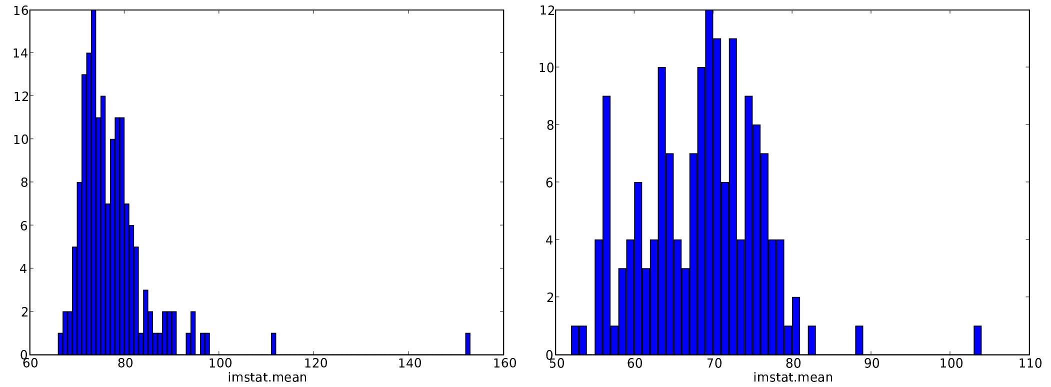

Figure 6.1: Bias frame histograms of mean pixel counts for the all sky camera (left) and SBC (right) from April 1 onwards.

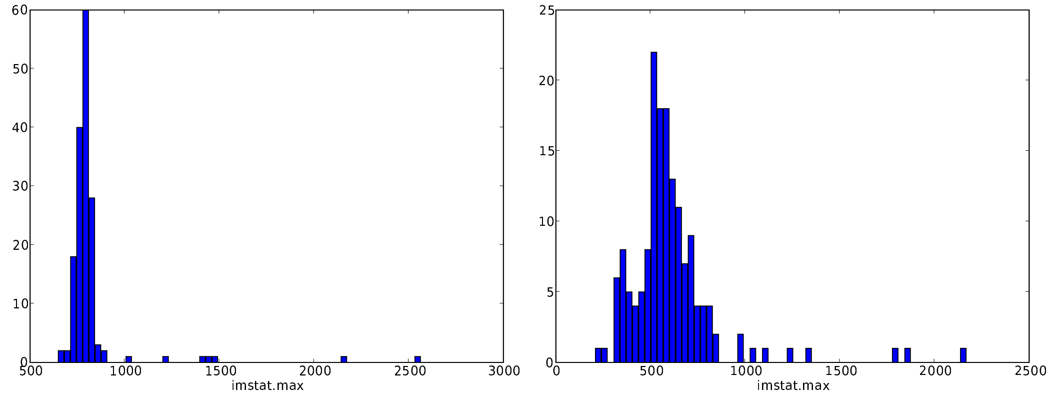

Figure 6.2: Bias frame histograms of maximum pixel counts for the all sky camera (left) and SBC (right) from April 1 onwards.

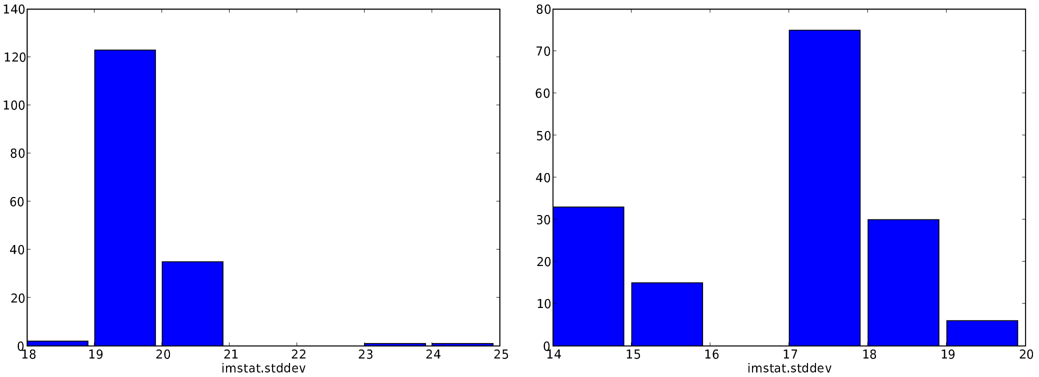

Figure 6.3: Bias frame histograms of standard deviations of pixel counts for the all sky camera (left) and SBC (right) from April 1 onwards.

The important values to take from these histograms is the bias frame bias level and the bias frame noise. The noise, which is just the standard deviation of counts in each frame, tells us the minimum signal level which we can hope to detect. The bias level, which is the mean number of counts per frame gives us an offset level when calculating ΔI (see Formula 4.12) for the background sky brightness. Table 6.1 gives these values for each camera.

	All sky camera	**SBC**
Bias level	77 ± 9	68 ± 8
Read out noise	19 ± 1	17 ± 2

Table 6.1: Summary of bias frame statistics for each camera.

6.2 Dark Frames

During the camera tests, dark frames (i.e. frames exposed to no light) were taken across a range of temperatures. Figure 6.4 shows the CCD temperature for each camera during the month of June. As can be seen, the temperature spent continued periods around −40°C and −30°C, while at other times it varied freely within a similar range. The dark frames available to us were taken at various temperatures, in increments of 10°C, so we shall present here the results for −30°C and −40°C.

In Figure 6.5 we show the mean dark current as a function of time for the all sky camera at each temperature. A linear fit to the points is also shown in

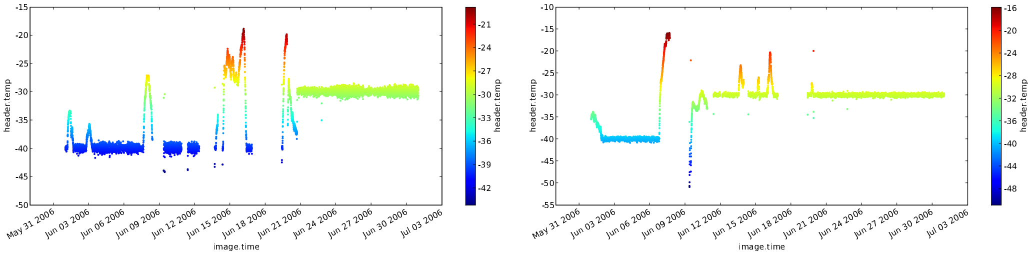

Figure 6.4: CCD temperature (°C) as a function of time for the month of June for the all sky camera (left) and SBC (right).

each graph. The parameters of these fits give an expression for the mean dark current I_μ as a function of exposure time at each temperature.

$$\begin{aligned} I_\mu(-30) &= 84.98 + 2.25t \qquad (6.1) \\ I_\mu(-40) &= 86.18 + 0.59t \qquad (6.2) \end{aligned}$$

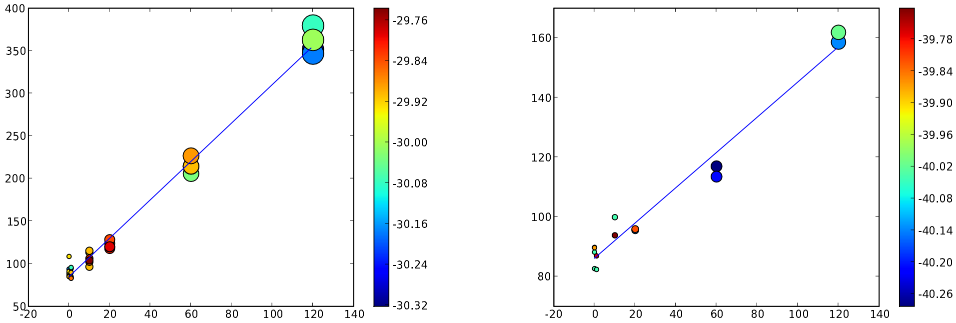

Figure 6.5: Average pixel counts from dark frames with the all sky camera. CCD temperature −30°C (left) and −40°C (right).

The constant term in each of the expressions given above corresponds quite closely with the bias level determined from the bias frames, which is what we would expect. The linear term then gives the contribution due to the dark current itself. Statistically, the bias level estimate from the bias frames (hundreds of images) will be more accurate than that obtained from the dark current measurements (tens of images). As such, to work out the total CCD contribution to the measured intensity we will use the bias level from the bias frames and the linear term from the dark current. This gives an expression of

$$I_{CCD}(-30) = 77.1 + 2.25t \qquad (6.3)$$

$$I_{CCD}(-40) = 77.1 + 0.59t \qquad (6.4)$$

The expressions above give the contribution from the CCD to any signals measured as a function of temperature and exposure time. These contributions must be subtracted from our measurements of the background sky intensity to get the contribution from the sky itself.

In Figure 6.6 we present the same results for the SBC. From this figure we can see that there is no detectable dark current above the bias level and read out noise. As such, in the the rest of our analysis, we only consider the bias level derived from the bias frames for the SBC, giving $I_{CCD} = 68.0$.

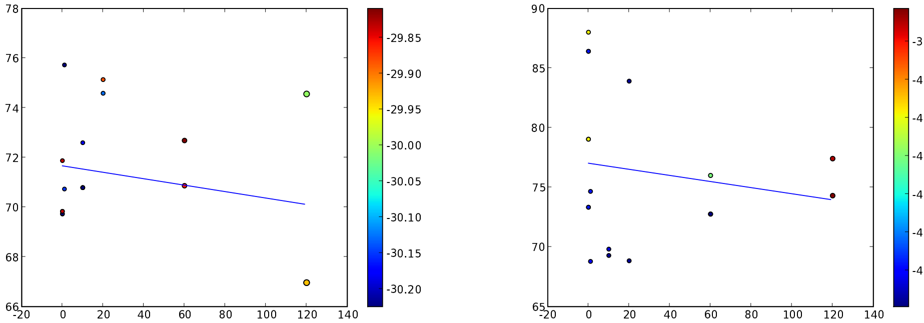

Figure 6.6: Average pixel counts from dark frames with the SBC. CCD temperature −30°C (left) and −40°C (right).

According to the manufacturer's specification for the CCD, the dark current at these temperatures should be negligible[1]. This suggests that our measurements for the all sky camera dark frames may not be correct. For the purposes of the analysis we use our measured values rather than the specification values, with the implications of this discussed in Chapter 7.

6.3 SBC

The sky brightness camera suffered throughout the year from the accumulation of ice on the external window of its enclosure (see Figure 3.2 in Chapter 3 for

---

[1] http://www.ccd.com/pdf/ccd_2000.pdf

an example of this). Figure 6.7 shows the sun elevation plotted against time. The colour scale shows the number of stars identified by `AptPhot`. As can be seen, there is only a small window of time when `AptPhot` was able to consistently identify stars.

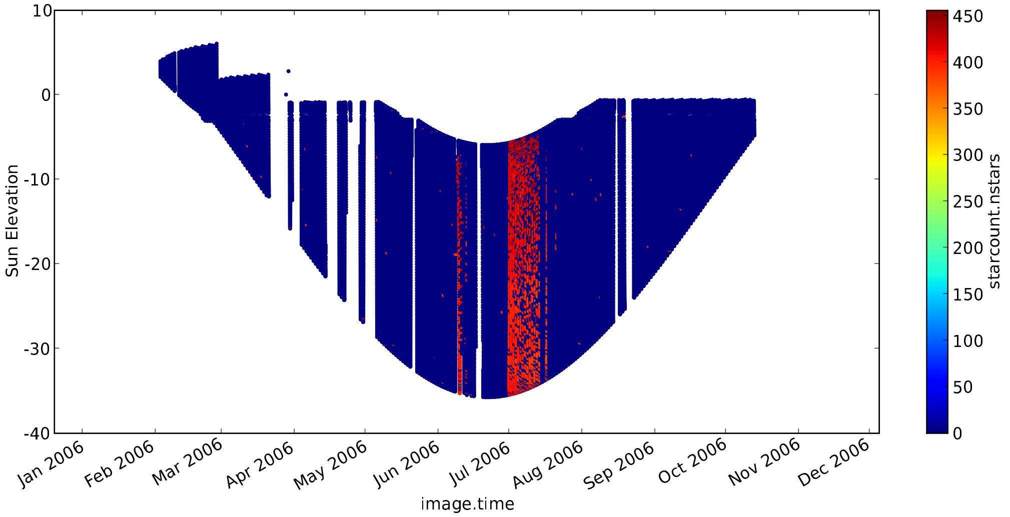

Figure 6.7: Sun elevation vs time for SBC - all images. Colour shows the number of stars identified.

Figure 6.8 shows the same variables as Figure 6.7, zoomed in on the first 2 weeks of July. This shows that during those two weeks, a large proportion of the images were sufficiently clear for stars to be identified. Unless otherwise specified all results for the SBC below are given for these first two weeks of July.

6.4 All Sky Camera

The all sky camera was much more successful than the SBC, providing consistent results for a large portion of the winter. In Figure 6.9 we plot the sun elevation against time, as in Figure 6.7. It can be seen that from the start of April onwards, when the sun was sufficiently low (i.e. sunzd[2] > 1.69 radians) we were able to successfully detect and measure stars.

Figure 6.10 shows the same data as Figure 6.9 for the time period after April

---

[2] sunzd is the value of sun zenith distance calculated by `apt_ephem`

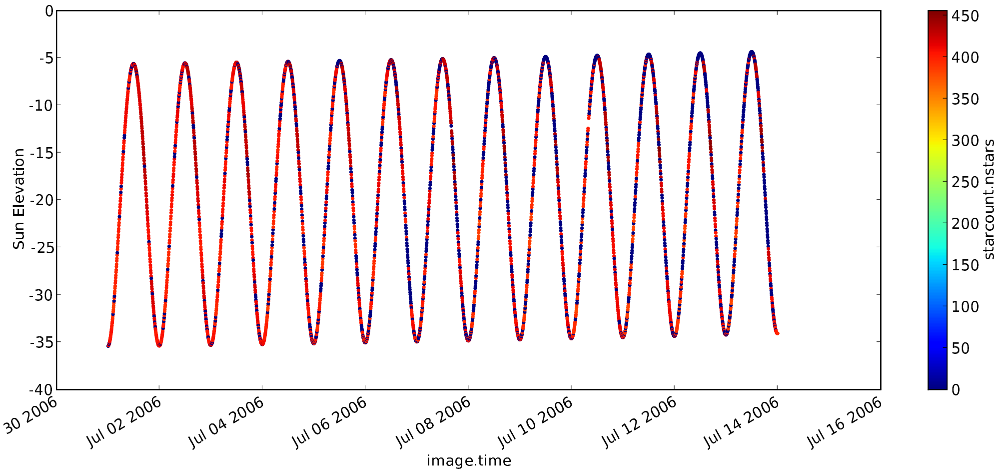

Figure 6.8: Sun elevation vs time for SBC images in the first 2 weeks of July, 2006. Colour shows the number of stars identified.

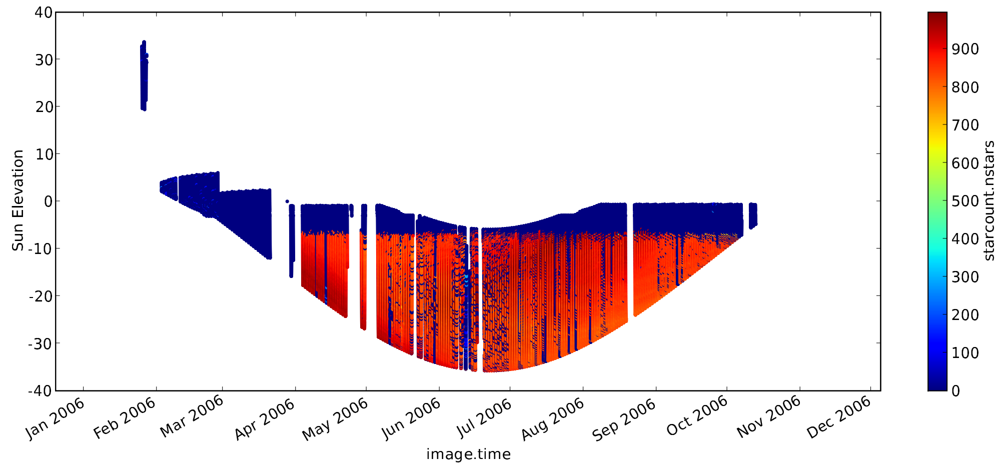

Figure 6.9: Sun elevation vs time for the all sky camera - all images. Colour shows the number of stars identified.

1st for images where the sun zenith distance was greater than 1.69 radians (approximately 6.8° below the horizon). In this regime we can see that `AptPhot` could consistently identify stars.

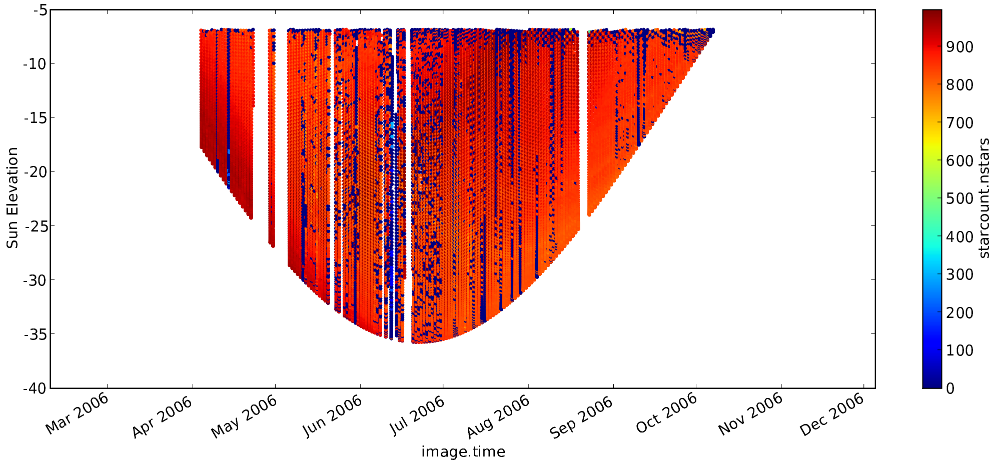

Figure 6.10: Sun elevation vs time Sky camera for images after April 1, 2006 with sun zenith distance > 1.69 radians. Colour shows the number of stars identified.

6.5 `AptPhot`

As the sky rotates above the fixed cameras, different parts of the sky come into the field of view. The rotation of the field of view is measured (in radians) by the local sidereal time (LST), so if two images have the same LST, they will have the same stars in their field of view.

Figure 6.11 shows a plot of the number of stars identified by `AptPhot` (when it actually succeeded in identifying any) as a function of LST for each camera.

As can be seen there is a large variation in the number of identified stars as the LST changes. This variation is much larger than the range of values at a given LST, and must be accounted for before using the number of stars as a measure. Furthermore, it is not clear why one given image would detect more stars than another similar image. As such we don't use the number of stars as a measure in the analysis below, we only use the success or failure of `AptPhot` as our condition.

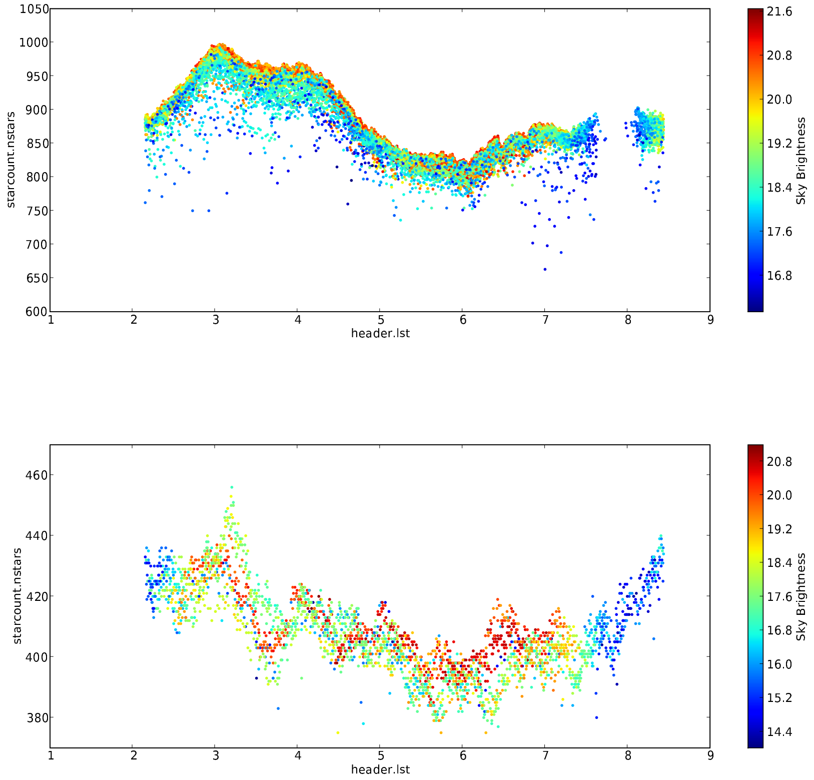

Figure 6.11: Number of stars identified by `AptPhot` vs local sidereal time. top: all sky camera. bottom: SBC.

6.6 Cloud Cover Estimates

One of the primary aims of the all sky camera is to measure cloud cover. In most cases it is not possible to actually resolve the clouds themselves, so we must infer their presence from our measurements. We use two different estimators for cloud cover here and then compare them against each other.

6.6.1 `AptAstrom`

The first estimator uses the value of `astrom.smag` from the database, which is calculated by `AptAstrom`. This value gives an estimate of the zero point magnitude (relative to our initial estimate, see Section 4.2.6 for details). If this value is large and negative then it indicates that our assumed zero magnitude was a long way from the actual zero magnitude. This will occur when there is a significant extinction being applied to the stars being measured. As clouds are a prime source of extinction in the atmosphere we take a large, negative *smag* value as an indicator of possible cloud cover.

Figure 6.12 shows a plot of the *smag* value vs time as well as the corresponding distribution of *smag* values when the sun zenith distance is greater than 1.69 radians. The colours show the number of stars detected by `AptPhot`, which will have significance in the sections below. We can see that the peak value is around -0.3, dropping off as the smag gets lower, with an odd looking component just above zero.

The condition we used for cloud free skies was $-1.0 < smag < 0.0$. This allows for the variation about the mean *smag* value of around -0.3 mag plus extinction of -0.4 mag. Table 6.2 shows the percentage of clear skies we have under various circumstances using this condition. The first column of results represents those images where the sun was sufficiently low for `AptPhot` to succeed (e.g. $sunzd > 1.69$). The second column is for astronomical twilight, when $1.69 < sunzd < 1.88$. The final column is for astronomical night time, when $sunzd > 1.88$ (-18°).

The results are split up into months, and for each month we consider the particular conditions of 8 second exposures, 40 second exposures as well as the complete data set. The results show a particularly low result for the month of April. If we consider Figure 6.12 it appears there is some constant offset being applied to *smag* for the month of April compared to the rest of the year. This also explains the small feature in the histogram just above $smag = 0$. As such our cloud cover estimates for this month are probably not representative of

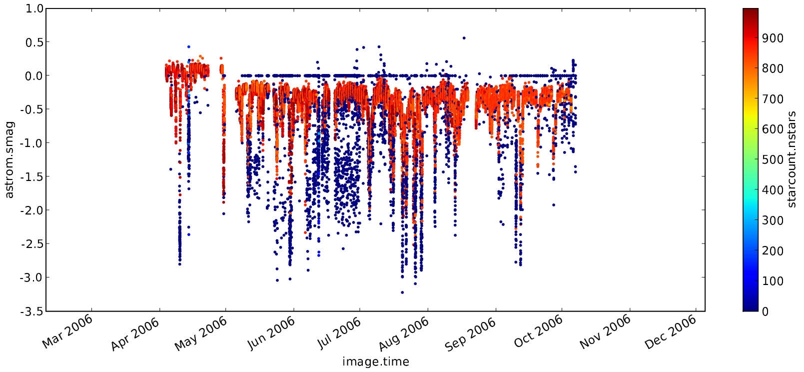

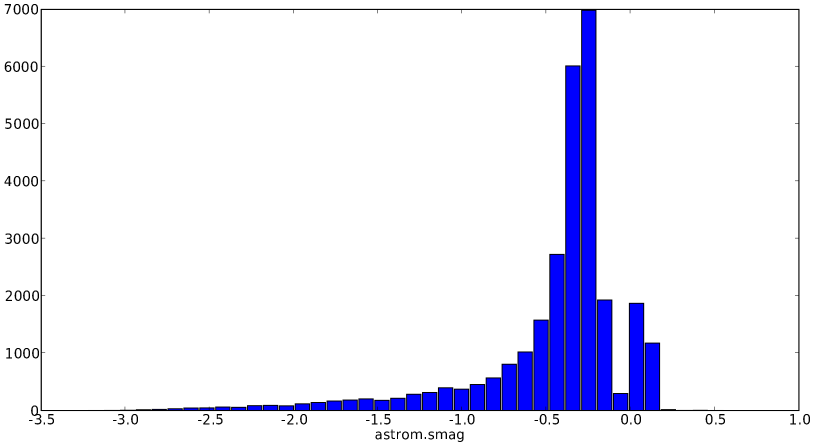

Figure 6.12: top: *smag* vs time for the all sky camera with the sun zenith distance greater than 1.69 radians. The colour scale shows the number of stars detected. bottom: Histogram of smag values.

		$sunzd > 1.69$	$1.69 < sunzd \leq 1.88$	$sunzd > 1.88$
April	8	0/0 = 0.0%	0/0 = 0.0%	0/0 = 0.0%
	40	653/2922 = 22.3%	440/1674 = 26.3%	213/1248 = 17.1%
	Any	664/2955 = 22.5%	451/1707 = 26.4%	213/1248 = 17.1%
May	8	0/0 = 0.0%	0/0 = 0.0%	0/0 = 0.0%
	40	4129/4813 = 85.8%	1517/1716 = 88.4%	2612/3097 = 84.3%
	Any	4156/4848 = 85.7%	1544/1750 = 88.2%	2612/3098 = 84.3%
June	8	1380/1768 = 78.1%	530/679 = 78.1%	850/1089 = 78.1%
	40	3459/4147 = 83.4%	1314/1543 = 85.2%	2145/2604 = 82.4%
	Any	4868/5950 = 81.8%	1873/2256 = 83.0%	2995/3694 = 81.1%
July	8	2845/3490 = 81.5%	1017/1271 = 80.0%	1828/2219 = 82.4%
	40	2815/3484 = 80.8%	1006/1255 = 80.2%	1809/2229 = 81.2%
	Any	5662/6977 = 81.2%	2025/2528 = 80.1%	3637/4449 = 81.7%
August	8	2229/2328 = 95.7%	938/984 = 95.3%	1291/1344 = 96.1%
	40	2216/2312 = 95.8%	938/977 = 96.0%	1278/1335 = 95.7%
	Any	4445/4640 = 95.8%	1876/1961 = 95.7%	2569/2679 = 95.9%
September	8	1269/1474 = 86.1%	1118/1317 = 84.9%	151/157 = 96.2%
	40	1284/1486 = 86.4%	1127/1326 = 85.0%	157/160 = 98.1%
	Any	2553/2960 = 86.2%	2245/2643 = 84.9%	308/317 = 97.2%
October	8	82/107 = 76.6%	82/107 = 76.6%	0/0 = 0.0%
	40	101/111 = 91.0%	101/111 = 91.0%	0/0 = 0.0%
	Any	192/229 = 83.8%	192/229 = 83.8%	0/0 = 0.0%
May-Oct	8	7805/9167 = 85.1%	3685/4358 = 84.6%	4120/4809 = 85.7%
	40	14004/16353 = 85.6%	6003/6928 = 86.6%	8001/9425 = 84.9%
	Any	21876/25604 = 85.4%	9755/11367 = 85.8%	12121/14237 = 85.1%

Table 6.2: Cloud cover estimates using the condition $-1.0 < smag < 0.0$ as the clear sky criterium.

the actual conditions, so the April results are not included in the final rows of the table, which show the combined results over the winter. The average combined clear sky percentage obtained using this method is 85.4%.

6.6.2 `AptPhot`

The other method we have for estimating cloud cover is to look at the success rate of the `AptPhot` routine. This assumes that if `AptPhot` is able to identify stars then the cloud cover cannot be significant.

In Table 6.3 we present the results for each month, as for Table 6.2, except with the condition for clear skies in this case being `starcount.nstars` > 0.

		$sunzd > 1.69$	$1.69 < sunzd \leq 1.88$	$sunzd > 1.88$
April	8	0/0 = 0.0%	0/0 = 0.0%	0/0 = 0.0%
	40	2709/2922 = 92.7%	1551/1674 = 92.7%	1158/1248 = 92.8%
	Any	2724/2955 = 92.2%	1566/1707 = 91.7%	1158/1248 = 92.8%
May	8	0/0 = 0.0%	0/0 = 0.0%	0/0 = 0.0%
	40	4015/4813 = 83.4%	1481/1716 = 86.3%	2534/3097 = 81.8%
	Any	4020/4848 = 82.9%	1486/1750 = 84.9%	2534/3098 = 81.8%
June	8	1174/1768 = 66.4%	401/679 = 59.1%	773/1089 = 71.0%
	40	3218/4147 = 77.6%	1182/1543 = 76.6%	2036/2604 = 78.2%
	Any	4396/5950 = 73.9%	1587/2256 = 70.3%	2809/3694 = 76.0%
July	8	2604/3490 = 74.6%	842/1271 = 66.2%	1762/2219 = 79.4%
	40	3201/3484 = 91.9%	1133/1255 = 90.3%	2068/2229 = 92.8%
	Any	5805/6977 = 83.2%	1975/2528 = 78.1%	3830/4449 = 86.1%
August	8	2055/2328 = 88.3%	825/984 = 83.8%	1230/1344 = 91.5%
	40	2239/2312 = 96.8%	938/977 = 96.0%	1301/1335 = 97.5%
	Any	4294/4640 = 92.5%	1763/1961 = 89.9%	2531/2679 = 94.5%
September	8	1163/1474 = 78.9%	1016/1317 = 77.1%	147/157 = 93.6%
	40	1351/1486 = 90.9%	1194/1326 = 90.0%	157/160 = 98.1%
	Any	2514/2960 = 84.9%	2210/2643 = 83.6%	304/317 = 95.9%
October	8	18/107 = 16.8%	18/107 = 16.8%	0/0 = 0.0%
	40	92/111 = 82.9%	92/111 = 82.9%	0/0 = 0.0%
	Any	110/229 = 48.0%	110/229 = 48.0%	0/0 = 0.0%
May-Oct	8	7014/9167 = 76.5%	3102/4358 = 71.2%	3912/4809 = 81.3%
	40	14116/16353 = 86.3%	6020/6928 = 86.9%	8096/9425 = 85.9%
	Any	21139/25604 = 82.6%	9131/11367 = 80.3%	12008/14237 = 84.3%

Table 6.3: Cloud cover estimates using the condition `starcount.nstars` > 0 as the clear sky criterium.

We can see here that the estimate for April is around 92% clear skies, which confirms that the results for April from Section 6.6.1 are indeed incorrect.

The most significant feature of these results is that the estimates from the 8 second exposures are much lower than from the 40 second exposures, suggesting that `AptPhot` is more likely to succeed with a 40 second exposure than an 8 second one. This difference is most pronounced during twilight, suggesting that the presence of the sun is contributing to `AptPhot`'s inability to detect stars under these conditions. We don't see this difference between exposure times for the *smag* results above. The average combined clear sky percentage obtained using this method is 82.6%.

6.6.3 Comparison of Methods

In both cases presented above we notice that the variation between months is much larger than the variation between twilight and night time within a given month. This suggests that the sun itself is not likely to be a significant contributor to our measurements of cloud cover in most cases. The one exception to this is for 8 second images measured with the star counting criteria.

If we consider Figure 6.12 we can see that the majority of images which have identified stars fall within the the acceptable clear sky limits of *smag* used above. As such we expect that both these criteria are detecting the same thing, e.g. clear skies. If this is the case then we should expect a large number of the clear sky images identified with one criteria to also be identified by the other.

As a final measure we combine the conditions for each of the above methods. This gives us a single condition which says that clear skies are defined as those where the *smag* value is within our acceptable range *and* the number of stars detected is greater than zero. Table 6.4 presents the results under this combined condition.

The results for this combined condition can be thought of as providing a lower bound on the amount of clear sky time. This gives us, in the most general case, a value of 79.4% clear time over the winter when the sun is below 1.69 radians zenith distance.

While the criteria used are not expected to have many false positives (i.e. images marked as clear when they actually are affected by cloud cover), the converse is not true. Images which are taken during clear skies may be deemed unclear for a number of reasons. For example, snow or ice on the enclosure window can lead to extinction, or the complete inability to identify stars, which would render an image unclear. The `AptPhot` routines may not be able to detect stars in an image if, for example, the image if affected by read out noise. For these reasons, while we may conclude that at least 79.4% of images are clear, we should not assume that the remaining 20.6% are obscured by cloud cover.

6.7 Sky Brightness

One of the primary aims of the cameras and this thesis is to measure the background sky brightness. I present here the results of these measurements

		$sunzd > 1.69$	$1.69 < sunzd \leq 1.88$	$sunzd > 1.88$
April	8	$0/0 = 0.0\%$	$0/0 = 0.0\%$	$0/0 = 0.0\%$
	40	$582/2922 = 19.9\%$	$396/1674 = 23.7\%$	$186/1248 = 14.9\%$
	Any	$582/2955 = 19.7\%$	$396/1707 = 23.2\%$	$186/1248 = 14.9\%$
May	8	$0/0 = 0.0\%$	$0/0 = 0.0\%$	$0/0 = 0.0\%$
	40	$3891/4813 = 80.8\%$	$1440/1716 = 83.9\%$	$2451/3097 = 79.1\%$
	Any	$3896/4848 = 80.4\%$	$1445/1750 = 82.6\%$	$2451/3098 = 79.1\%$
June	8	$1174/1768 = 66.4\%$	$401/679 = 59.1\%$	$773/1089 = 71.0\%$
	40	$3181/4147 = 76.7\%$	$1179/1543 = 76.4\%$	$2002/2604 = 76.9\%$
	Any	$4359/5950 = 73.3\%$	$1584/2256 = 70.2\%$	$2775/3694 = 75.1\%$
July	8	$2495/3490 = 71.5\%$	$817/1271 = 64.3\%$	$1678/2219 = 75.6\%$
	40	$2805/3484 = 80.5\%$	$997/1255 = 79.4\%$	$1808/2229 = 81.1\%$
	Any	$5300/6977 = 76.0\%$	$1814/2528 = 71.8\%$	$3486/4449 = 78.4\%$
August	8	$2053/2328 = 88.2\%$	$823/984 = 83.6\%$	$1230/1344 = 91.5\%$
	40	$2209/2312 = 95.5\%$	$931/977 = 95.3\%$	$1278/1335 = 95.7\%$
	Any	$4262/4640 = 91.9\%$	$1754/1961 = 89.4\%$	$2508/2679 = 93.6\%$
September	8	$1135/1474 = 77.0\%$	$988/1317 = 75.0\%$	$147/157 = 93.6\%$
	40	$1274/1486 = 85.7\%$	$1117/1326 = 84.2\%$	$157/160 = 98.1\%$
	Any	$2409/2960 = 81.4\%$	$2105/2643 = 79.6\%$	$304/317 = 95.9\%$
October	8	$18/107 = 16.8\%$	$18/107 = 16.8\%$	$0/0 = 0.0\%$
	40	$92/111 = 82.9\%$	$92/111 = 82.9\%$	$0/0 = 0.0\%$
	Any	$110/229 = 48.0\%$	$110/229 = 48.0\%$	$0/0 = 0.0\%$
May-Oct	8	$6875/9167 = 75.0\%$	$3047/4358 = 69.9\%$	$3828/4809 = 79.6\%$
	40	$13452/16353 = 82.3\%$	$5756/6928 = 83.1\%$	$7696/9425 = 81.7\%$
	Any	$20336/25604 = 79.4\%$	$8812/11367 = 77.5\%$	$11524/14237 = 80.9\%$

Table 6.4: Cloud cover estimates using the conditions `starcount.nstars` > 0 and $-1.0 < smag < 0.0$ as the clear sky criteria.

and also the contributions due to the moon and the sun. To calculate the brightness we use the following formula

$$\begin{aligned} M &= Z - 2.5\log_{10}(\Delta I) + 2.5\log_{10}(A) && (6.5) \\ \Delta I &= I_{bg} - I_{CCD} && (6.6) \\ A(SBC) &= 11.3^2 && (6.7) \\ A(Sky) &= 225^2 && (6.8) \end{aligned}$$

In these formulas M is the sky brightness (in mag/arcsec^2), Z is the zero point magnitude (in mag), ΔI is the relative intensity of the background with respect to the CCD bias level and A is the pixel area for each camera, in arcsec^2

All results below are calculated using the database field `astrom.sky` as I_{bg} and the formulas (6.3) and (6.4) as the I_{CCD}. Z is of course given by the database field `astrom.zmag`.

6.7.1 Brightness vs Time

We first look at the behaviour of the sky brightness as a function of time and compare the results in each camera. Figure 6.13 shows the sky brightness as a function of time for each camera. The colour scale shows the exposure time. Only those images where the sun zenith distance is greater than 1.69 radians and on which `AptPhot` was successful are shown in this and the following plots.

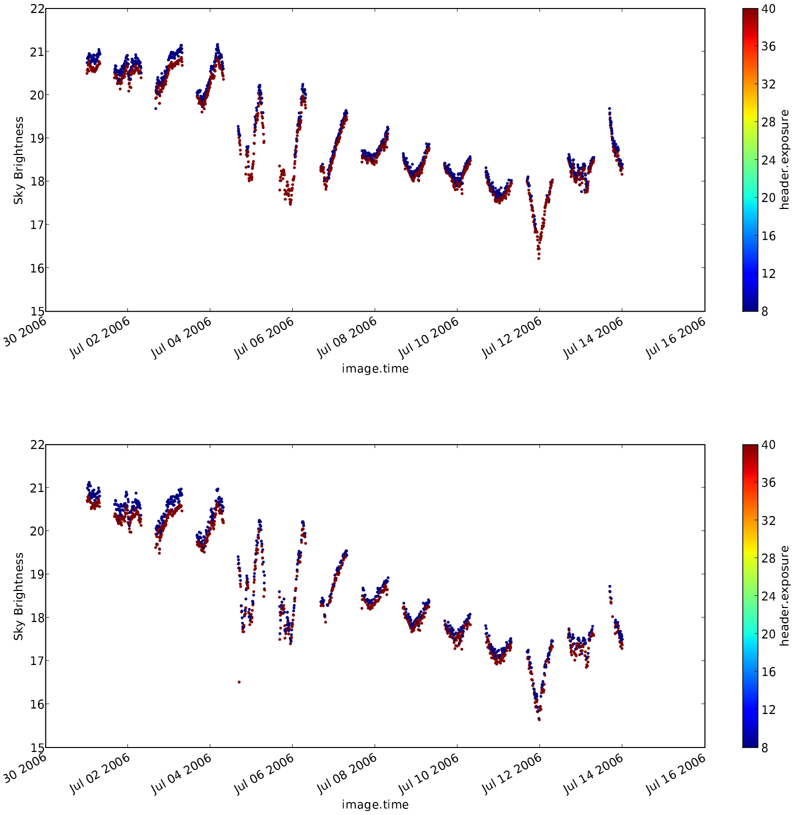

Figure 6.13: Sky brightness vs time during the first 2 weeks of July for the all sky camera (top) and SBC (bottom). Colour represents exposure time.

We can see that over the first two weeks of July, when both cameras were operating well, the measurements of sky brightness from the two cameras correspond quite closely.

There is however a distinct difference of approximately 0.2 mag/arcsec^2 between the results for 8 second exposures compared to 40 second exposures. This suggests that our estimate of the dark current is not as accurate as it could be. This issue is discussed in more detail in Chapter 7.

Figure 6.14 shows the background sky brightness as a function of time for the first two weeks of July for both the SBC and the all sky camera. The colour scale shows the angular distance from the middle point of the camera's field of view to the moon (`header.moondist`). The daily variation in the moon distance can be seen both in the colour scale and the daily variation in the background brightness.

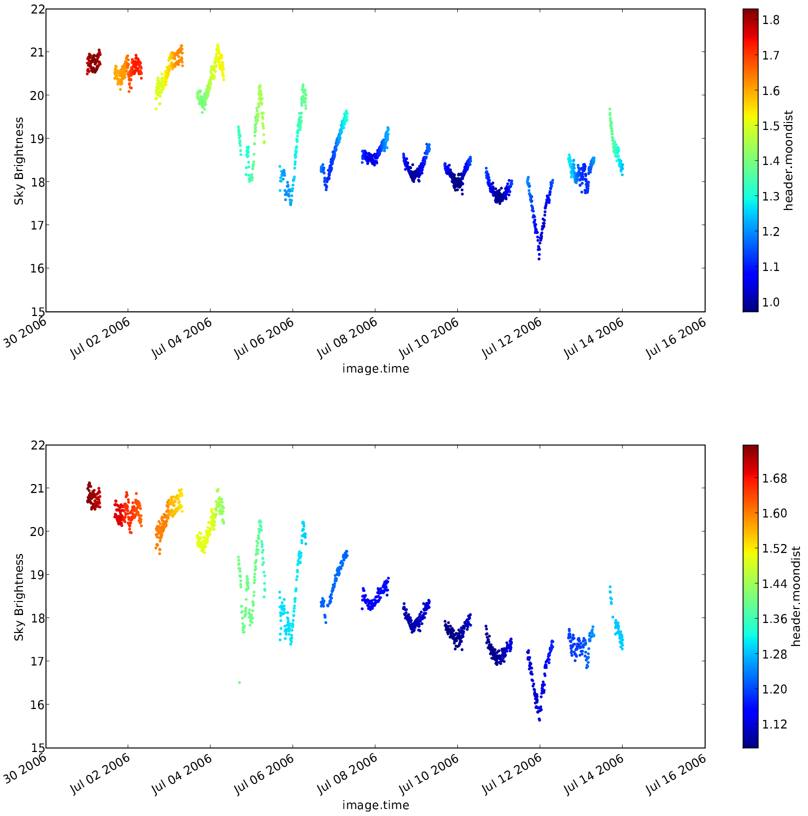

Figure 6.14: Sky brightness vs time during the first 2 weeks of July for the all sky camera (top) and SBC (bottom). Colour represents `header.moondist`.

Figure 6.15 shows the same data as Figure 6.14 except with the colour scale showing the phase of the moon as a percentage. It can clearly be seen the brightness increases as the moon becomes fuller.

Figure 6.16 shows the sky brightness as a function of time for the all sky

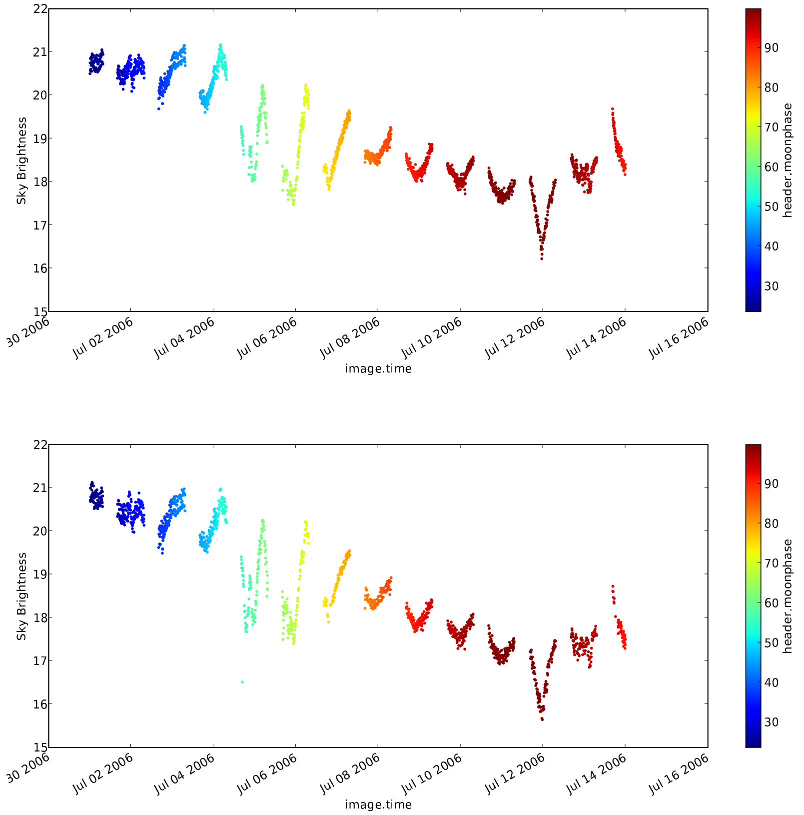

Figure 6.15: Sky brightness vs time during the first 2 weeks of July for the all sky camera (top) and SBC (bottom). Colour represents moon phase (%).

camera for the period of time from April 1 to October 12. The monthly variation due to the phase of the moon, represented by the colour scale, can very clearly be seen.

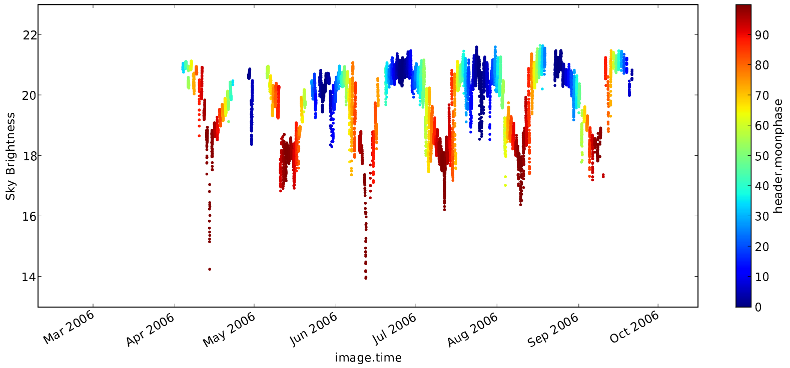

Figure 6.16: Sky brightness vs time for the all sky camera from April 1 to October 12. Colour scale shows moon phase.

6.7.2 Brightness Histograms

In Figure 6.17 we show the distribution of sky brightnesses for each camera as well as the effects of the sun and the moon. The left hand column shows the all sky camera, while the SBC is on the right. For the all sky camera we take all images from between April 1 and October 12 where `astrom.sky` $>$ 0 (e.g. `AptAstrom` ran successfully) while for the SBC we take those images from the same time period where `starcount.nstars > 0` (e.g. `AptPhot` ran successfully).

In the first row we have essentially all the images. There are clearly different effects contributing to the trimodal distributions seen in the histograms. In the second row we remove all images where the sun zenith distance is above 1.8 radians. This removes the brightest mode from the distribution. In the third row those images with a moon zenith distance above 1.8 radians are removed from the distribution. This removes the next brightest mode. In the final images we keep only those images which have an *smag* value greater than -0.8 (e.g. clear skies without cloud cover). This removes a large proportion of the images from the bright tail, leaving us with a distribution representing those images taken in clear, dark viewing time.

The distribution parameters (mean and standard deviation) for each of these

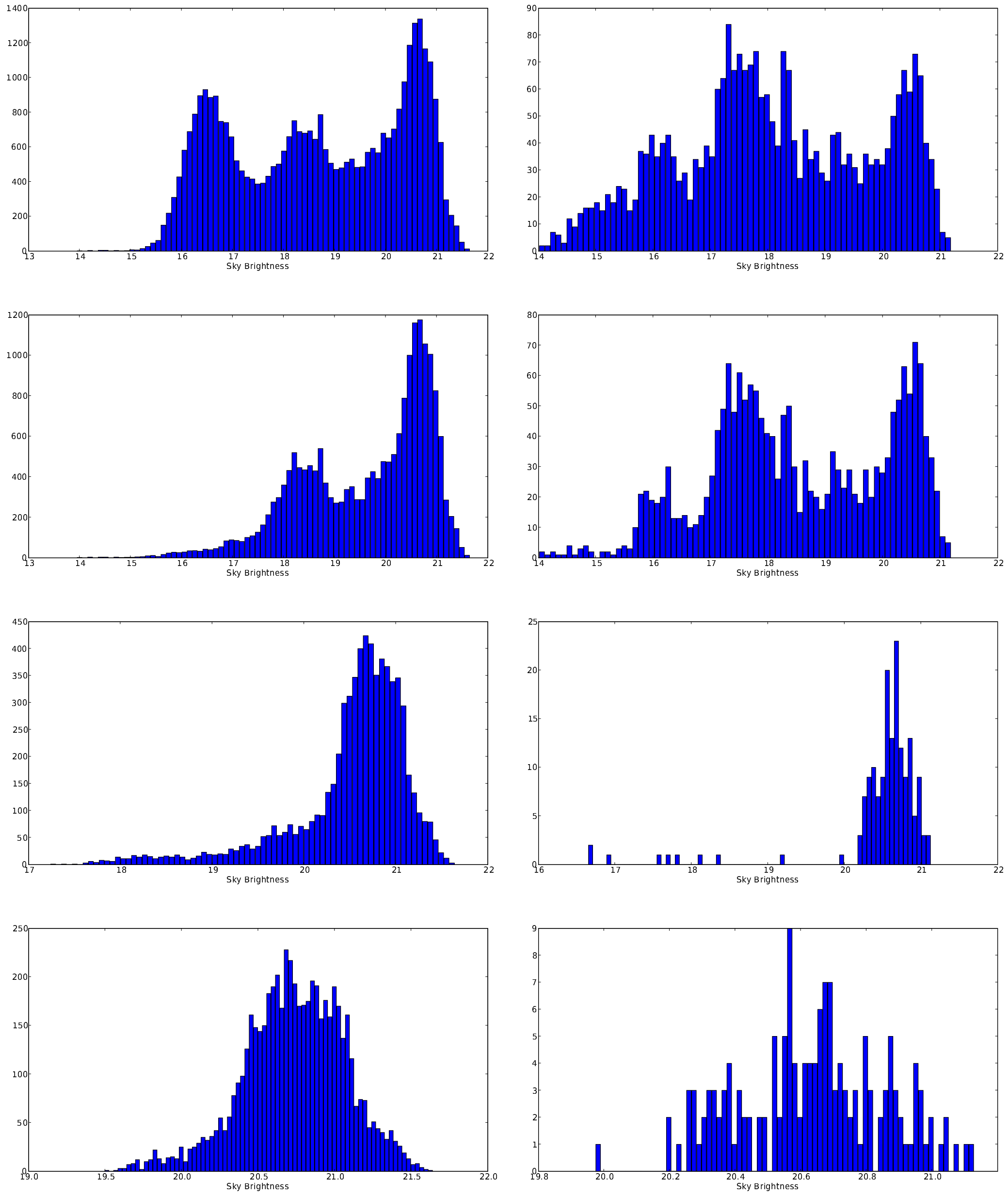

Figure 6.17: Histograms of sky brightness for the all sky camera (left) and SBC (right). Row 1: all images. Row 2: `header.sunzd` > 1.8 radians filter added. Row 3: `header.moonzd` > 1.8 radians filter added. Row 4: `astrom.smag` > -0.8 filter added.

histograms is given in Table 6.5. From this table we can see that during optimal conditions we have a sky brightness of 20.7 ± 0.3 mag/arcsec^2 according to the all sky camera and 20.6 ± 0.2 mag/arcsec^2 according to the SBC.

All sky	**SBC**
18.7 ± 1.7	18.1 ± 1.7
19.6 ± 1.3	18.5 ± 1.6
20.5 ± 0.7	20.5 ± 0.7
20.7 ± 0.3	20.6 ± 0.2

Table 6.5: Brightness estimates corresponding to the images in Figure 6.17.

6.7.3 Brightness vs Sun

As shown in the histograms above, the sun contributes significantly to the sky brightness. We wish to quantify this contribution of the sun to the background sky brightness. In Figure 6.18 we plot the sky brightness as a function of sun zenith distance for those images from the all sky camera which have no moon and are clear (e.g. `astrom.smag` > -0.8 and `header.moonzd` > 1.8 and `starcount.nstars` > 0).

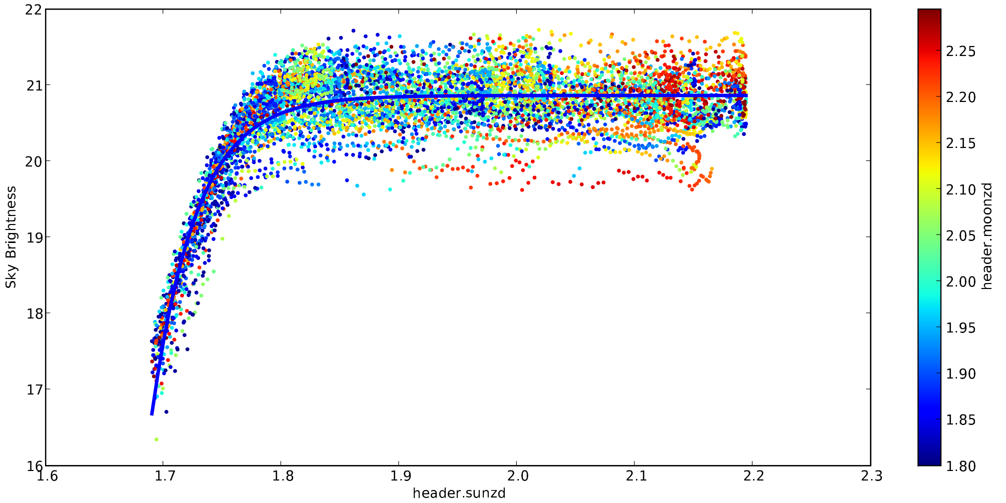

Figure 6.18: Sky brightness (mag/arcsec^2) vs sun zenith (rad) distance for clear skies with no moon.

The solid line in this figure shows a fitted curve[3] which has the parameters

---

[3] All fitted curves in this section were calculated using the routine `optimize.fmin` from

$$M(\theta_s) \quad = \quad 20.77 - 10^{20.32 - 11.66\theta_s} \tag{6.9}$$

where θ_s is the sun zenith distance, with an an average error of 0.26 mag/arcsec^2 per image. In this basic model we have a background sky brightness of 20.77 mag/arcsec^2. This model is appropriate when the sun is below 1.69 radians (i.e. it does not account for day time brightness), the sky is free of clouds and there is negligible contributions from the moon.

6.7.4 Brightness vs Moon

The contribution due to the moon is slightly more complicated than for the sun, as we need to take into account both the zenith distance and the phase.

In Figure 6.19 we plot the sky brightness as a function of magnitude for a small range of moon zenith distance values ($1.4 <$ `header.moonzd` < 1.5) which shows that for an approximately constant moon elevation, the moon phase has a linear contribution to the sky brightness.

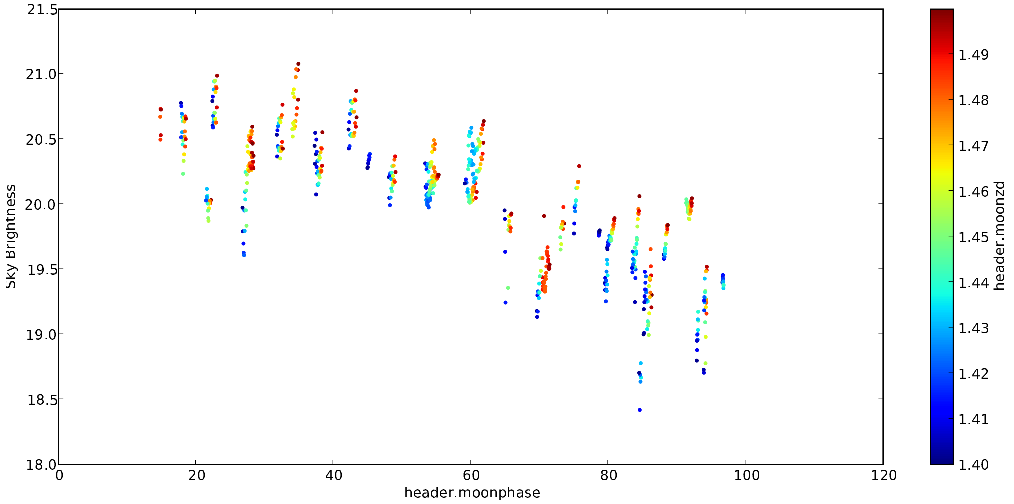

Figure 6.19: Sky brightness (mag/arcsec^2) vs moon phase (%) for clear skies with no sun for an approximately constant moon elevation.

In Figure 6.20 we show the sky brightness as a function of the moon zenith distance for images from the all sky camera when the sky was clear and the

---

the `scipy` Python package. http://www.scipy.org/. This routine uses a Nelder-Mead simplex algorithm to find the minimum of a function of one or more variables.

sun was well below the horizon (e.g. `header.sunzd` > 1.88). The colour scale of this image shows the phase of the moon.

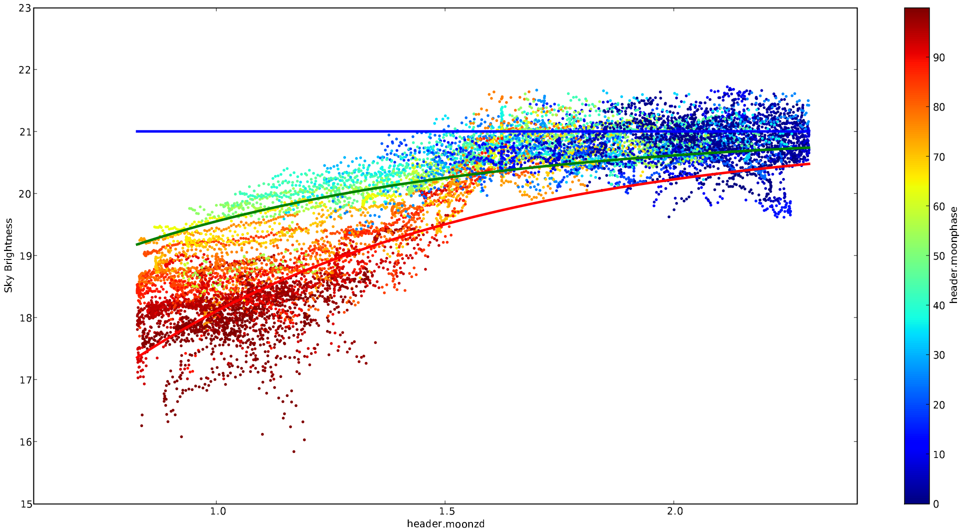

Figure 6.20: Sky brightness (mag/arcsec^2) vs moon zenith distances (rad) for clear skies with no sun.

The data from Figure 6.20 was fitted to two models, one which accounted for moon phase and one which did not. The parameters of these fits are.

$$\begin{aligned} M(\theta_m) &= 21.68 - 10^{1.08-0.58\theta_m} && (6.10) \\ M(\theta_m, \phi_m) &= 20.91 - \phi_m 10^{-0.97-0.58\theta_m} && (6.11) \end{aligned}$$

where θ_m is the moon zenith distance (in radians) and ϕ_m is the moon phase (as a percentage). The average error per image in this fit is 0.32 mag/arcsec^2. The lines in Figure 6.20 show the fits from this model for different values of the moon phase. The blue line is for $\phi_m = 0$ (e.g. a new moon), the green line is for $\phi_m = 50$ (a half moon) and the red line is for $\phi_m = 100$ (a full moon). These show how the contribution to the sky brightness increase as the moon becomes fuller. According to this model the background sky brightness is 20.91 mag/arcsec^2.

6.7.5 Brightness vs Sun and Moon

We have considered the contribution of the sun and moon individually. We now combine these two models to calculate the sky brightness when both the sun and the moon are present. Figure 6.21 shows the sky brightness as a function of sun zenith distance, with the colour scale representing the moon zenith distance.

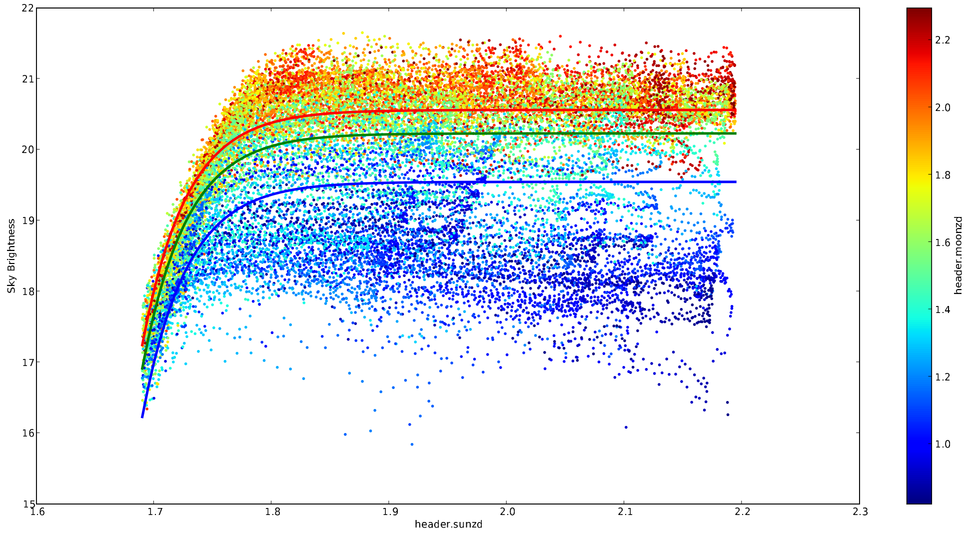

Figure 6.21: Sky brightness (mag/arcsec^2) vs sun zenith distance (rad) for clear skies.

The model we have used is simply a linear combinations of the individual models for the sun and the moon. The parameters obtained are

$$M(\theta_s, \theta_m, \phi_m) \quad = \quad 20.87 - 10^{19.97-11.51\theta_s} - \phi_m 10^{-0.95-0.63\theta_m} \tag{6.12}$$

with an average error per image of 0.35 mag/arcsec^2. The lines in Figure 6.21 show the fitted model for a half moon at various values of moon zenith distance. The red, green and blue lines have moon zenith distance values of 1.0, 1.5 and 2.0 radians respectively. According to this model, which incorporates a significantly larger number of images than the individual models given above, the background sky brightness is 20.87 mag/arcsec^2.

6.8 Summary

In the results above we presented a number of different estimates for the cloud cover and the background sky brightness.

Using the condition of $-1.0 <$ `astrom.smag` < 0.0 we estimate clear skies 85.4% of the time. Using the condition `starcount.nstars` > 0 we estimate clear skies 82.6% of the time. Using a combined condition of $-1.0 <$ `astrom.smag` < 0.0 and `starcount.nstars` > 0 we estimate clear skies 79.4% of the time.

From histograms of the sky brightness for each camera we get an estimate of the background sky brightness of 20.7 ± 0.3 mag/arcsec^2 for the all sky camera and 20.6 ± 0.2 for the SBC.

Based on models of the sun and moon for the sky brightness measured by the all sky camera we get the following results:

$$
\begin{aligned}
M(\theta_s) &\rightarrow 20.77 \pm 0.26 \qquad (6.13)\\
M(\theta_m, \phi_m) &\rightarrow 20.91 \pm 0.32 \qquad (6.14)\\
M(\theta_s, \theta_m, \phi_,) &\rightarrow 20.87 \pm 0.35 \qquad (6.15)
\end{aligned}
$$

Chapter 7

Discussion

In the process of obtaining the results presented above, a large number of lessons were learned along the way. In this Chapter I provide a discussion of various aspects of the project including what worked well, what was less than ideal, and what can be done in the future.

7.1 Software

The development of various software tools was vital for the completion of this project. Each of the tools developed arose out of necessity when it became clear that doing a certain task manually was going to take too long. By automating as many processes as possible I was able to cut down on the countless hours of manual labour which would have been involved in handling all the data.

7.1.1 Image Processing

The initial processing of the data took weeks of processing time. As such, it was important that the software ran in the most efficient way possible. The client-server model software, while running on a single machine, allowed the CPU to remain fully utilised at all times, minimising the total analysis time.

The client server model also helped to minimise the down time of the processing. Occasionally a fault would arise which would cause one of the processing clients to terminate unexpectedly. By having multiple clients running, the system could continue processing data. If there was only a single process running the analysis, such an error would mean that no processing was being done until the user (e.g. me) came and restarted the program. It was after this had happened a number of times that the decision to develop the client-server system was made.

7.1.2 Data Exploration

The Gattini Data Explorer proved to be invaluable while exploring the database. Not knowing *a priori* what to expect from the data it was important to look closely at many different aspects of it while working towards the final results presented in this thesis. Being able to plot the data from a graphical user interface saved a lot of time which would have been spent manually writing SQL statements and plotting the results. This meant I was able to look at a considerably greater amount of data while looking for results. Furthermore, when other researchers need to examine the data they will not need to spend their time learning the appropriate way in which to query the database, as the GDE provides an intuitive way to get at the data needed quickly and easily.

The scope for improvement of the GDE is quite large. The code is flexible enough that essentially any analysis which can be performed on the data can be incorporated into the program. One particular feature which may be useful is the ability to export data to other file formats, such as text files or binary blocks. This would allow the data to be easily imported into other programs, such as spreadsheets, which may be more appropriate for the analysis required in some situations.

Another possibility for the GDE is to provide a web based front end. This would require a reasonable amount of effort, but may be an appropriate way in which to make the results of our analysis available to other researchers.

7.1.3 Summary

The software tools developed for this thesis have been crucial in obtaining the results presented. Furthermore, they will be an extremely valuable set of tools for subsequent analysis of data collected from the Gattini cameras.

7.2 Analysis and Results

While the analysis of the data has provided a number of interesting results, the preliminary nature of these results should be noted. Our results suggest a background sky brightness in the V band of 20.9 mag/arcsec^2, which compares poorly with sites such as Paranal, which have sky brightness values of 21.6 mag/arcsec^2. The results for sky brightness, however, may change significantly with more in depth analysis. The flat fields used in the analysis are less than ideal, although improvements for these are currently being worked on. This means that the estimates of the magnitude zero point are not as accurate as they could be. Furthermore, the images are calibrated against V magnitudes from the catalogue, however it is not the case that our images are actually measured completely in the V band.

The cloud cover estimates depend directly on the flat fielding of the raw images. By using more accurate flat fields we can improve the confidence in the results of both `AptAstrom` and `AptPhot`.

The condition on *smag* used to define clear skies which was presented is somewhat arbitrary. Further investigation into the expected extinction due to various kinds of cloud cover will provide a more robust condition on which to base future results. Additionally, a method of discriminating between extinction due to ice and snow on the lens would improve the accuracy of the results.

7.2.1 Flat Fields

The flat fields which were available for this analysis were only preliminary images taken during the commissioning of the cameras. The lighting conditions for these images may not have been perfectly uniform, so the overall shape of the flat fields will not perfectly correct for the properties of the lens and CCD.

Inaccuracies in the flat fields lead to errors in our estimates of sky brightness when calibrating against the catalogue values. This in turns leads to errors in our estimate of the zero point magnitude. It also affects the estimate of the sky background intensity used in determining the sky brightness.

Work is currently underway to derive more precise flat field images, based on comparisons of the brightness of catalogue stars across the images. Unfortunately, due to time constraints on this thesis, results using this new method are not able to be presented here. Initial investigations suggest that this new method will result in a significant improvement in the sky brightness estimate accuracy.

In addition, preliminary work has been done to generate twilight flat frames, which will provide the expected background intensity across the image as a function of sun and moon position. We will then be able to compare these twilight flat frames to our images to determine how well the models fit the experimental images.

7.2.2 Filters

The calibration against catalogue stars is done based on their magnitude in the V band. This assumes that our cameras are detecting precisely in the V band. As can be seen in Figure 7.1, the central wavelength of this passband is 505nm.

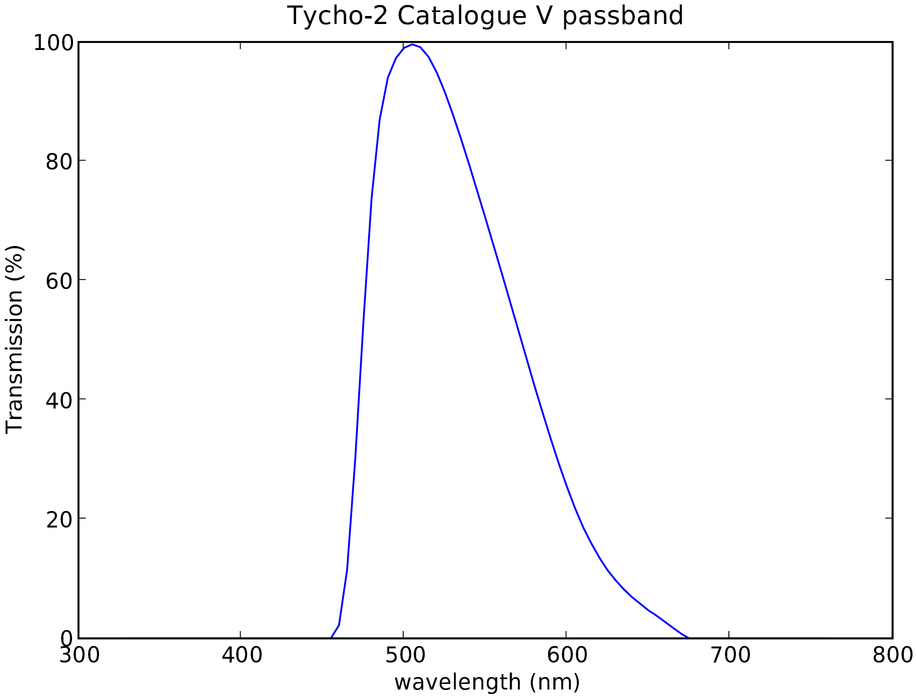

Figure 7.1: The V passband used by the Tycho-2 catalogue

The passband of the all sky camera has its peak around 500nm (recall Figure 2.3), however it also extends well into the longer wavelengths of the red (R) part of the spectrum. Large contributions to the sky brightness are expected in this region of the spectrum due to various airglow emissions [18]. These extra contributions to our signal will lead to over estimates of the V band sky brightness. Quantifying this over estimate is one of the top priorities for the ongoing analysis of the Gattini data, as meaningful comparisons with other sites cannot be made if the effective passband is not accounted for.

While the passband of the all sky camera may explain the comparatively bright results it obtained, a similar argument cannot be applied to the SBC, which had similar sky brightness results. Further investigation into this issue will be undertaken in the near future.

7.2.3 Airmass

The effect of airmass has not been accounted for in the analysis performed so far. For the all sky camera there is a variation in the extinction due to airmass of up to 0.13 mag across the image. Because this is not taken into account when calibrating against the catalogue stars our estimate of the zero point magnitude will have at least this much error in it.

By accounting for airmass we can expect to reduce the variability in the value of $smag$. This will also improve the accuracy of cloud cover estimates which rely on $smag$.

7.2.4 Dark Current

Our estimates of the dark current vary from zero to $2.25t$ (where t is exposure time, see Section 6.2) across various conditions and between the cameras. The cameras are nominally identical, with negligible dark current at our operating temperatures, so the difference in dark current warrants further investigation. If, for example, the dark current of the SBC at -30°C was actually $2.25t$ rather than the zero we measured, this would results in our original brightness estimate being approximately 0.15 mag/arcsec^2 too bright. Conversely, if the dark current on the all sky camera is indeed negligible, we would see a change in our estimates in the opposite direction.

The difference in brightness results for 8 second vs 40 second exposures suggest that either our dark current or bias level estimates are not completely accurate, so further investigation should be undertaken to resolve these differences. Preliminary investigations show that zero dark current with a bias level of approximately 35 counts would bring the 8 second and 40 second exposures into line with each other for both cameras, however at this stage there is no reason to believe that this is indeed the bias level.

7.3 Future Work

This thesis represents the first analysis of the data from the Gattini project. While the results presented here provide a useful first estimate, there is a large scope for improving the analysis on this data set, as well as improving the operation of the experiment for subsequent data sets.

7.3.1 Calibration

As we have discussed above there is a great need for further calibration of the cameras. The remote location of the cameras means that doing such testing will not be an easy task. For the results of the cameras to be accurate however, they must be accurately calibrated, so it is in the best interests of the project to arrange for further testing to be undertaken.

At present, for a given exposure time and operating temperature we have no more than three dark frames for each camera. This does not provide much statistical power, so we should aim to take perhaps 30 images in each condition to get a more accurate estimate of the dark current. The same applies for flat fields. We need a reasonable number of images taken at each appropriate condition to ensure our average flat frames are representative of the properties of the lens and CCD.

7.3.2 Cloud Cover Statistics

As well as improving the quality of our cloud cover estimators, we would also like to collect statistics on the duration of both clear and cloudy periods. These figures have important implications for experiments which require long periods of uninterupted observing.

7.3.3 Software

The analysis code which was used in this project can be improved in a number of ways. Due to time pressures a number of corners were cut during its development which could be improved upon. In particular, exception handling could be done much better. At various times the processing clients would terminate due to an uncaught exception. These exceptions were not accounted for in the program, however they should be revisited before analysing another data set to maximise the efficiency of the processing.

The other major improvement which can be made is to fully distribute the processing model. By allowing otherwise idle machines on the network to help with the processing the total processing time required can be reduced by a large factor. There are two main obstacles to this at present: distributing the data, and handling software dependencies. The problem of distributing data can be handled by placing the raw images in an appropriate shared network drive. Software dependencies are slightly more difficult as each machine is likely to have a different operating set up, so installing packages such as IRAF may be difficult. Once these problems are addressed however, the processing of data will become much more manageable.

7.3.4 Real Time Processing

Using the processing methods described in this thesis, each image can be analysed in less than 30 seconds. With 5 minutes between each pair of images being taken, there is ample time left over for the controlling machine to do real time processing of the images.

Each pair of images can be expected to produce approximately 40kB of compressed results. Taking an image every 5 minutes means that approximately 11.5MB of results will be generated each day. If this is too much for the Iridium link to handle then the amount of data produced for each identified star can be reduced to a reasonable size by leaving out the less important variables for each star.

Doing such real time processing on site would have two main benefits. Firstly, it would allow for the most up to date results to be assessed immediately, rather than waiting until summer for a disk to be returned. Secondly, it would serve as a rudimentary backup system. In the event that the data on site was corrupted, there would still be usable results available from the experiment.

One of the difficulties in setting up such a system will be getting the appropriate software installed on the controlling machine, as the only connection it has to the internet is the Iridium satellite link, which has a connection speed of 2400 baud.

7.3.5 Lunar Shield

Over the summer of 2006/2007 a lunar shield was installed on the all sky camera to reduce the brightness due to scattered moonlight. This has had the effect of slightly reducing the effective field of view of the camera while also blocking out a large amount of moonlight. The effectiveness of this device will be quantified when the data from the 2007 winter is analysed.

7.3.6 Icing

One of the biggest problems experienced by the cameras was the accumulation of ice on the enclosure. This was particularly detrimental to the SBC, with only a fraction of its data being usable.

As the Gattini cameras continue operation at Dome C, and when they are moved to other sites, it is important that ice cover is detected early so that it can be cleared in a timely manner. This is not always an easy task, particularly over the winter when outside temperatures drop to $-80°$, as the cameras are located approximately 1km from the main station.

By making sure that the cameras remain ice free we maximise the amount of clean data available, which improves any results obtained. The difficulty in doing this is in finding either a robust, automatic way to detect ice cover, along with a way to remove ice once formed, or a method stop ice from forming in the first place. This is something which is being investigated this year, as it also has implications for our cloud cover estimates.

7.3.7 Exposure Times

During particularly dark periods of time, the 8 second exposures taken with the all sky camera were affected by the read out noise of the CCD. This low signal to noise ratio could lead to errors in our brightness calculation. Furthermore, the 40 second exposures had stars detected in them more often than the 8 second exposures. As such, the possibility of extending the exposure time of the 8 second exposures should be considered for the ongoing experiment.

7.3.8 Camera Logs

At present there is no systematic way of keeping track of adjustments made to the cameras or any of their supporting systems throughout their operations. Most changes which are made are done in an ad-hoc manner, with decisions made through personal communications between the concerned parties. While this is probably the most efficient way to get things done, it is not the most transparent. When we look at the data there are clearly systematic changes which have been made at various stages, however these changes are not officially documented anywhere.

To address this issue it would be worthwhile to implement a systematic camera logging system, where any changes to the system can be noted for future reference. Such a system would allow any changes in the behaviour of the data to be compared back to changes in the cameras or their systems.

7.3.9 Publishing of Data and Code

To provide complete transparency in the analysis process we should publish both the analysis software and the raw data, so that our methodologies can be understood, and hopefully improved on, by other interested parties. This ensures that any comparisons with results from other sites can be made in the appropriate context.

The first step in doing this will be to document all the software and make the code repository internally accessible within the department. Once this is done appropriate methods of making the analysis available to outside parties can be considered. This depends of course on the wishes of the researchers in charge of the project as a whole.

Chapter 8

Conclusion

In this thesis I have presented the first analysis of the data from the Gattini cameras. A number of software systems were developed to automate this processing and to subsequently explore the data. These systems will provide the foundation for future analysis of both the currently available data as well the data which is actively being collected as the cameras continue their operation.

A number of operational issues, such as icing of the sky brightness camera for large periods of the winter, and their effect on the results have been identified. The Gattini team will continue to work on minimising the impact of such problems.

Throughout the thesis it has become clear that having the appropriate tools to handle and examine the available data is of crucial importance. The development of these tools will a valuable asset during all future work with the Gattini data. They will allow researchers to work with the data without having to worry about the details of manually extracting and plotting data themselves. Furthermore the automated processing scripts will allow future data sets to be processed quickly and efficiently when they become available.

Measurements of the amount of clear sky time have found that the sky can be considered clear at least 79% of the time, which represents an improvement on the results of previous experiments, which put a lower bound at 74%. More detailed investigation into appropriate clear sky criteria will lead to more accurate estimates in the future.

While we are not yet in a position to compare the sky brightness at Dome C to other sites, we are certainly much closer to this particular goal. A number of issues with the analysis, as performed in this thesis, have been identified and they will be addressed in the immediate future.

As the quest for better astronomy conditions on the Antarctic plateau continues [28] it is possible that the Gattini cameras will be called into action to measure the conditions at locations such as Dome A, the highest point on the plateau. If so, then the tools and techniques presented in this thesis can hopefully provide a starting point in measuring the darkest skies on the planet.

Appendix A

Database Schema

The following is the output of the program `mysqldump` when run on the GDB. It decribes the commands required to replicate our database structure, and thus defines the database schema.

```
-- MySQL dump 10.10
--
-- Host: localhost    Database: test
-- ------------------------------------------------------
-- Server version 5.0.27

/*!40101 SET @OLD_CHARACTER_SET_CLIENT=@@CHARACTER_SET_CLIENT */;
/*!40101 SET @OLD_CHARACTER_SET_RESULTS=@@CHARACTER_SET_RESULTS */;
/*!40101 SET @OLD_COLLATION_CONNECTION=@@COLLATION_CONNECTION */;
/*!40101 SET NAMES utf8 */;
/*!40103 SET @OLD_TIME_ZONE=@@TIME_ZONE */;
/*!40103 SET TIME_ZONE='+00:00' */;
/*!40014 SET @OLD_UNIQUE_CHECKS=@@UNIQUE_CHECKS, UNIQUE_CHECKS=0 */;
/*!40014 SET @OLD_FOREIGN_KEY_CHECKS=@@FOREIGN_KEY_CHECKS,
                  FOREIGN_KEY_CHECKS=0 */;
/*!40101 SET @OLD_SQL_MODE=@@SQL_MODE, SQL_MODE='NO_AUTO_VALUE_ON_ZERO' */;
/*!40111 SET @OLD_SQL_NOTES=@@SQL_NOTES, SQL_NOTES=0 */;

--
-- Table structure for table `astrom`
--
```

```
DROP TABLE IF EXISTS ‘astrom‘;
CREATE TABLE ‘astrom‘ (
  ‘image_id‘ int(11) NOT NULL,
  ‘success‘ tinyint(4) NOT NULL,
  ‘smag‘ float NOT NULL,
  ‘zmag‘ float NOT NULL,
  ‘sky‘ float NOT NULL,
  PRIMARY KEY  (‘image_id‘),
  UNIQUE KEY ‘image_id‘ (‘image_id‘),
  CONSTRAINT ‘astrom_ibfk_1‘ FOREIGN KEY (‘image_id‘) REFERENCES ‘image‘ (‘id‘)
) ENGINE=InnoDB DEFAULT CHARSET=latin1;

--
-- Table structure for table ‘cam‘
--

DROP TABLE IF EXISTS ‘cam‘;
CREATE TABLE ‘cam‘ (
  ‘id‘ tinyint(4) NOT NULL auto_increment,
  ‘name‘ char(3) NOT NULL,
  PRIMARY KEY  (‘id‘),
  UNIQUE KEY ‘id‘ (‘id‘),
  UNIQUE KEY ‘name‘ (‘name‘)
) ENGINE=InnoDB DEFAULT CHARSET=latin1;

--
-- Table structure for table ‘flat‘
--

DROP TABLE IF EXISTS ‘flat‘;
CREATE TABLE ‘flat‘ (
  ‘image_id‘ int(11) NOT NULL,
  ‘flatfile‘ varchar(25) NOT NULL,
  ‘outputfile‘ varchar(50) NOT NULL,
  PRIMARY KEY  (‘image_id‘),
  UNIQUE KEY ‘image_id‘ (‘image_id‘),
  CONSTRAINT ‘flat_ibfk_1‘ FOREIGN KEY (‘image_id‘) REFERENCES ‘image‘ (‘id‘)
) ENGINE=InnoDB DEFAULT CHARSET=latin1;

--
```

```
-- Table structure for table ‘header‘
--

DROP TABLE IF EXISTS ‘header‘;
CREATE TABLE ‘header‘ (
  ‘image_id‘ int(11) NOT NULL,
  ‘temp‘ float NOT NULL,
  ‘exposure‘ float NOT NULL,
  ‘time‘ datetime NOT NULL,
  ‘sunzd‘ float NOT NULL,
  ‘moonzd‘ float NOT NULL,
  ‘moondist‘ float NOT NULL,
  ‘moonphase‘ float NOT NULL,
  ‘moonmag‘ float NOT NULL,
  ‘ra‘ float NOT NULL,
  ‘decl‘ float NOT NULL,
  ‘lst‘ float NOT NULL,
  ‘jd‘ float NOT NULL,
  ‘crval1‘ float NOT NULL,
  ‘crval2‘ float NOT NULL,
  PRIMARY KEY  (‘image_id‘),
  UNIQUE KEY ‘image_id‘ (‘image_id‘),
  CONSTRAINT ‘header_ibfk_1‘ FOREIGN KEY (‘image_id‘)
  REFERENCES ‘image‘ (‘id‘)
) ENGINE=InnoDB DEFAULT CHARSET=latin1;

--
-- Table structure for table ‘image‘
--

DROP TABLE IF EXISTS ‘image‘;
CREATE TABLE ‘image‘ (
  ‘id‘ int(11) NOT NULL auto_increment,
  ‘filename‘ varchar(100) NOT NULL,
  ‘basename‘ varchar(50) NOT NULL,
  ‘cam_id‘ tinyint(4) NOT NULL,
  ‘time‘ datetime NOT NULL,
  PRIMARY KEY  (‘id‘),
  UNIQUE KEY ‘id‘ (‘id‘),
  UNIQUE KEY ‘filename‘ (‘filename‘),
```

```
  UNIQUE KEY ‘basename‘ (‘basename‘),
  KEY ‘cam_id‘ (‘cam_id‘),
  CONSTRAINT ‘image_ibfk_1‘ FOREIGN KEY (‘cam_id‘) REFERENCES ‘cam‘ (‘id‘)
) ENGINE=InnoDB DEFAULT CHARSET=latin1;

--
-- Table structure for table ‘imstat‘
--

DROP TABLE IF EXISTS ‘imstat‘;
CREATE TABLE ‘imstat‘ (
  ‘image_id‘ int(11) NOT NULL,
  ‘min‘ int(11) NOT NULL,
  ‘max‘ int(11) NOT NULL,
  ‘mean‘ int(11) NOT NULL,
  ‘stddev‘ int(11) NOT NULL,
  PRIMARY KEY  (‘image_id‘),
  UNIQUE KEY ‘image_id‘ (‘image_id‘),
  CONSTRAINT ‘imstat_ibfk_1‘ FOREIGN KEY (‘image_id‘) REFERENCES ‘image‘ (‘id‘)
) ENGINE=InnoDB DEFAULT CHARSET=latin1;

--
-- Table structure for table ‘phot‘
--

DROP TABLE IF EXISTS ‘phot‘;
CREATE TABLE ‘phot‘ (
  ‘image_id‘ int(11) NOT NULL,
  ‘star_id‘ int(11) NOT NULL,
  ‘vmag‘ float NOT NULL,
  ‘smag‘ float NOT NULL,
  ‘mag3‘ float NOT NULL,
  ‘mag4‘ float NOT NULL,
  ‘err3‘ varchar(100) NOT NULL,
  ‘err4‘ varchar(100) NOT NULL,
  ‘X‘ float NOT NULL,
  ‘Y‘ float NOT NULL,
  KEY ‘star_id‘ (‘star_id‘),
  KEY ‘image_id‘ (‘image_id‘,‘star_id‘),
  CONSTRAINT ‘phot_ibfk_1‘ FOREIGN KEY (‘star_id‘)
```

```
  REFERENCES `star` (`star_id`),
  CONSTRAINT `phot_ibfk_2` FOREIGN KEY (`image_id`)
  REFERENCES `image` (`id`)
) ENGINE=InnoDB DEFAULT CHARSET=latin1;

--
-- Table structure for table `star`
--

DROP TABLE IF EXISTS `star`;
CREATE TABLE `star` (
  `star_id` int(11) NOT NULL auto_increment,
  `cat_id` int(11) NOT NULL,
  `ra` float NOT NULL,
  `decl` float NOT NULL,
  PRIMARY KEY  (`star_id`),
  UNIQUE KEY `cat_id` (`cat_id`)
) ENGINE=InnoDB DEFAULT CHARSET=latin1;

--
-- Table structure for table `starcount`
--

DROP TABLE IF EXISTS `starcount`;
CREATE TABLE `starcount` (
  `image_id` int(11) NOT NULL,
  `nstars` int(11) NOT NULL,
  KEY `image_id` (`image_id`),
  CONSTRAINT `starcount_ibfk_1` FOREIGN KEY (`image_id`)
  REFERENCES `image` (`id`)
) ENGINE=InnoDB DEFAULT CHARSET=latin1;

--
-- Table structure for table `unzip`
--

DROP TABLE IF EXISTS `unzip`;
CREATE TABLE `unzip` (
  `image_id` int(11) NOT NULL,
  `success` tinyint(4) NOT NULL,
```

```
  ‘outputfile‘ varchar(50) default NULL,
  PRIMARY KEY  (‘image_id‘),
  UNIQUE KEY ‘image_id‘ (‘image_id‘),
  UNIQUE KEY ‘outputfile‘ (‘outputfile‘),
  CONSTRAINT ‘unzip_ibfk_1‘ FOREIGN KEY (‘image_id‘)
  REFERENCES ‘image‘ (‘id‘)
) ENGINE=InnoDB DEFAULT CHARSET=latin1;
/*!40103 SET TIME_ZONE=@OLD_TIME_ZONE */;

/*!40101 SET SQL_MODE=@OLD_SQL_MODE */;
/*!40014 SET FOREIGN_KEY_CHECKS=@OLD_FOREIGN_KEY_CHECKS */;
/*!40014 SET UNIQUE_CHECKS=@OLD_UNIQUE_CHECKS */;
/*!40101 SET CHARACTER_SET_CLIENT=@OLD_CHARACTER_SET_CLIENT */;
/*!40101 SET CHARACTER_SET_RESULTS=@OLD_CHARACTER_SET_RESULTS */;
/*!40101 SET COLLATION_CONNECTION=@OLD_COLLATION_CONNECTION */;
/*!40111 SET SQL_NOTES=@OLD_SQL_NOTES */;

-- Dump completed on 2007-06-05  4:12:46
```

Appendix B

slave_images

```
#!/bin/bash

DIRECT=/home/local/bin

[ -e $DIRECT/image.lock2 ] && rm -f /$DIRECT/image.lock*
 && killall slave_images && exit

[ -e $DIRECT/image.lock1 ] && touch $DIRECT/image.lock2
&& exit

touch $DIRECT/image.lock1

DIR=`date +%y%m%d`
FNAME=`date +%y%m%d%H%M`
MINS=`date +%M`
HR=`date +%H`

export LD_LIBRARY_PATH=/opt/apogee/lib

EL=`$DIRECT/el.pl $FNAME`

echo "elevation is $EL"

SETSBC=-40
SETSKY=-40

if [ $EL -ge -1 ]
```

```
then
       OUT1=`$DIRECT/cam_temp -u 2 -c $SETSKY`
       OUT2=`$DIRECT/cam_temp -u 1 -c $SETSBC`
else

       SKYEXP=8
       SBCEXP=8

       [ $EL -ge -7 ] && SBCEXP=2
       [ $EL -ge -6 ] && SBCEXP=1.0
       [ $EL -ge -5 ] && SBCEXP=0.2
       [ $EL -ge -4 ] && SBCEXP=0.1
       [ $EL -ge -3 ] && SBCEXP=0.002

       [ $EL -ge -9 ] && SKYEXP=10
       [ $EL -ge -8 ] && SKYEXP=5
       [ $EL -ge -7 ] && SKYEXP=0.5
       [ $EL -ge -5 ] && SKYEXP=0.1
       [ $EL -ge -4 ] && SKYEXP=0.05
       [ $EL -ge -3 ] && SKYEXP=0.005

       if [ $EL -le -10 ]
           then
           [ $MINS -eq 3 ] || [ $MINS -eq 13 ] || [ $MINS -eq 23 ] || \
       [ $MINS -eq 33 ] || [ $MINS -eq 43 ] || [ $MINS -eq 53
   ] && SBCEXP=40
           [ $MINS -eq 3 ] || [ $MINS -eq 13 ] || [ $MINS -eq 23 ] || \
       [ $MINS -eq 33 ] || [ $MINS -eq 43 ] || [ $MINS -eq 53
   ] && SKYEXP=40

       fi

       [ $MINS -eq 48 ] && [ $HR -eq 23 ] && SBCEXP=0 && SKYEXP=0

       USED=`df -h|grep hdb1|awk '{print $5}'| cut -d"%" -f 1`
       [ $USED -ge 95 ] && rm -f /home/local/bin/image.lock* && exit
       [ ! -d /slave/$DIR ] && mkdir /slave/$DIR

       rm -f /data/*fits.bz2
       rm -f /data/Sky.fits
```

```
    rm -f /data/SBC.fits
    OUT1=`$DIRECT/cam_image -s 1 -b 20 -c $SETSKY -t $SKYEXP -i ` \
`/data/Sky.fits -u 2`
    OUT2=`$DIRECT/cam_image -s 1 -b 20 -c $SETSBC -t $SBCEXP -i ` \
`/data/SBC.fits -u 1`

    if [ $MINS -eq 48 ] || [ $MINS -eq 43 ]
    then
    /home/local/bin/fitscopy /data/SBC.fits[756:956,548:748] \
"!/data/jpegs/$FNAME.cSBC.fits"
    /home/local/bin/fitscopy /data/Sky.fits[695:895,612:812] \
"!/data/jpegs/$FNAME.cSky.fits"
#       [ 684:884, 612:812 ]
    bzip2 /data/jpegs/$FNAME.cSBC.fits
    bzip2 /data/jpegs/$FNAME.cSky.fits
    fi

    bzip2 /data/SBC.fits
    bzip2 /data/Sky.fits

    if [ $MINS -eq 43 ] && [ $HR -eq 23 ]
    then
            cp /data/SBC.fits.bz2 /data/fits/$FNAME.SBC.fits.bz2
            cp /data/Sky.fits.bz2 /data/fits/$FNAME.Sky.fits.bz2
    fi

    if [ $MINS -eq 48 ] && [ $HR -eq 23 ]
    then
            cp /data/SBC.fits.bz2 /data/fits/$FNAME.zSBC.fits.bz2
            cp /data/Sky.fits.bz2 /data/fits/$FNAME.zSky.fits.bz2
    fi

    if [ $MINS -eq 43 ] && [ $HR -eq 3 ]
    then
            cp /data/SBC.fits.bz2 /data/fits/$FNAME.SBC.fits.bz2
            cp /data/Sky.fits.bz2 /data/fits/$FNAME.Sky.fits.bz2
    fi

    mv /data/SBC.fits.bz2 /slave/$DIR/$FNAME.SBC.fits.bz2
    mv /data/Sky.fits.bz2 /slave/$DIR/$FNAME.Sky.fits.bz2
```

```
       echo "$FNAME xSky=$SKYEXP xSBC=$SBCEXP" >> /data/$DIR.camlog
fi

TEMP1=‘echo "$OUT1" | grep "Current temperature:" | awk ’{print $3}’‘
FAN1=‘echo "$OUT1" | grep "Fan state:" | awk ’{print $3}’‘
SETP1=‘echo "$OUT1" | grep "Cooler setpoint:" | awk ’{print $3}’‘
EN1=‘echo "$OUT1" | grep "Cooler Enable:" | awk ’{print $3}’‘
STAT1=‘echo "$OUT1" | grep "Cooler status:" | awk ’{print $3}’‘
CPOW1=‘echo "$OUT1" | grep "Cooler power:" | awk ’{print $3}’‘

TEMP2=‘echo "$OUT2" | grep "Current temperature:" | awk ’{print $3}’‘
FAN2=‘echo "$OUT2" | grep "Fan state:" | awk ’{print $3}’‘
SETP2=‘echo "$OUT2" | grep "Cooler setpoint:" | awk ’{print $3}’‘
EN2=‘echo "$OUT2" | grep "Cooler Enable:" | awk ’{print $3}’‘
STAT2=‘echo "$OUT2" | grep "Cooler status:" | awk ’{print $3}’‘
CPOW2=‘echo "$OUT2" | grep "Cooler power:" | awk ’{print $3}’‘

echo "$FNAME Sky el=$EL temp=$TEMP1 fan=$FAN1 setp=$SETP1, enab=$EN1, " \
    "stat=$STAT1, pow=$CPOW1" >> /data/$DIR.camlog
echo "$FNAME SBC el=$EL temp=$TEMP2 fan=$FAN2 setp=$SETP2, enab=$EN2, " \
    "stat=$STAT2, pow=$CPOW2" >> /data/$DIR.camlog

rm -f /home/local/bin/image.lock1
rm -f /home/local/bin/image.lock2
```

Bibliography

[1] M. Burton, D. K. Aitken, D. A. Allen, M. C. B. Ashley, M. G. Burton, R. D. Cannon, B. D. Carter, G. S. Dacosta, M. A. Dopita, and M. L. Duldig. The scientific potential for astronomy from the Antarctic Plateau. *Proceedings of the Astronomical Society of Australia*, 11:127–150, August 1994.

[2] R. D. Marks, J. Vernin, M. Azouit, J. F. Manigault, and C. Clevelin. Measurement of optical seeing on the high antarctic plateau. A&AS, 134:161–172, January 1999.

[3] R. D. Marks. Astronomical seeing from the summits of the Antarctic plateau. A&A, 385:328–336, April 2002.

[4] J. T. Dempsey, J. W. V. Storey, and A. Phillips. Auroral Contribution to Sky Brightness for Optical Astronomy on the Antarctic Plateau. *Publications of the Astronomical Society of Australia*, 22:91–104, 2005.

[5] J. S. Lawrence. Infrared and Submillimeter Atmospheric Characteristics of High Antarctic Plateau Sites. PASP, 116:482–492, May 2004.

[6] J. P. Lloyd, B. R. Oppenheimer, and J. R. Graham. The Potential of Differential Astrometric Interferometry from the High Antarctic Plateau. *Publications of the Astronomical Society of Australia*, 19:318–322, 2002.

[7] E. Aristidi, K. Agabi, M. Azouit, E. Fossat, J. Vernin, T. Travouillon, J. S. Lawrence, C. Meyer, J. W. V. Storey, B. Halter, W. L. Roth, and V. Walden. An analysis of temperatures and wind speeds above Dome C, Antarctica. A&A, 430:739–746, February 2005.

[8] M. C. B. Ashley, M. G. Burton, P. G. Calisse, A. Phillips, and J. W. V. Storey. Site testing at Dome C - cloud statistics from the ICECAM experiment. *Highlights of Astronomy*, 13:932–+, January 2005.

[9] E. Aristidi, A. Agabi, J. Vernin, M. Azouit, F. Martin, A. Ziad, and E. Fossat. Antarctic site testing: First daytime seeing monitoring at Dome C. A&A, 406:L19–L22, July 2003.

[10] Eric Aristidi, Abdelkrim Agabi, Eric Fossat, Max Azouit, Francois Martin, Tatiana Sadibekova, Tony Travouillon, Jean Vernin, and Aziz Ziad. Site testing in summer at dome c, antarctica, 2005.

[11] Abdelkrim Agabi, Eric Aristidi, Max Azouit, Eric Fossat, Francois Martin, Tatiana Sadibekova, Jean Vernin, and Aziz Ziad. First whole atmosphere night-time seeing measurements at Dome C, Antarctica, 2005.

[12] J. S. Lawrence, M. C. B. Ashley, M. G. Burton, P. G. Calisse, J. T. Dempsey, J. R. Everett, O. Maher, J. W. V. Storey, and T. Travouillon. The AASTINO: Automated Astrophysical Site Testing INvincible Observatory. *Memorie della Societa Astronomica Italiana Supplement*, 2:217–+, 2003.

[13] J. S. Lawrence, M. C. B. Ashley, A. Tokovinin, and T. Travouillon. Exceptional astronomical seeing conditions above Dome C in Antarctica. Nature, 431:278–281, September 2004.

[14] A. Tokovinin, J. Vernin, A. Ziad, and M. Chun. Optical Turbulence Profiles at Mauna Kea Measured by MASS and SCIDAR. PASP, 117:395–400, April 2005.

[15] T. Travouillon, M. C. B. Ashley, M. G. Burton, J. W. V. Storey, and R. F. Loewenstein. Atmospheric turbulence at the South Pole and its implications for astronomy. A&A, 400:1163–1172, March 2003.

[16] A. Mayer. On the History of the Stellar Magnitude Scale. *Journal of the American Association of Variable Star Observers (JAAVSO)*, 15:283–285, December 1986.

[17] F. Patat. Night Sky Brightness During Sunspot Maximum at Paranal. *The Messenger*, 115:18–21, March 2004.

[18] S. L. Kenyon and J. W. V. Storey. A Review of Optical Sky Brightness and Extinction at Dome C, Antarctica. PASP, 118:489–502, March 2006.

[19] Suzanne L. Kenyon, Michael C. B. Ashley, Jon Everett, Jon S. Lawrence, and John W. V. Storey. Nigel and the optical sky brightness at dome c, antarctica. volume 6267, page 62671M. SPIE, 2006.

[20] P. G. Calisse, M. C. B. Ashley, M. G. Burton, M. A. Phillips, J. W. V. Storey, S. J. E. Radford, and J. B. Peterson. Submillimeter Site Testing at Dome C, Antarctica. *Publications of the Astronomical Society of Australia*, 21:256–263, 2004.

[21] V. P. Walden, M. S. Town, B. Halter, and J. W. V. Storey. First Measurements of the Infrared Sky Brightness at Dome C, Antarctica. PASP, 117:300–308, March 2005.

[22] L. Valenziano and G. dall'Oglio. Millimetre astronomy from the High Antarctic Plateau: Site testing at Dome C. *Publications of the Astronomical Society of Australia*, 16:167–174, August 1999.

[23] L. Valenziano, M. R. Attolini, C. Burigana, M. Malaspina, N. Mandolesi, G. Ventura, F. Villa, G. dall'Oglio, L. Pizzo, R. Cosimi, A. Miriametro, L. Martinis, L. Piccirillo, M. Bersanelli, and G. Morgante. APACHE96. CMBR Anisotropy Experiment at Dome C. In G. Novak and R. Landsberg, editors, *Astrophysics From Antarctica*, volume 141 of *Astronomical Society of the Pacific Conference Series*, pages 81–+, 1998.

[24] M. Busso, G. Tosti, F. Roncella, M. Bagaglia, G. Nucciarelli, R. Fastellini, O. Straniero, M. Dolci, M. Ragni, I. di Varano, L. Corcione, C. Abia, I. Dominguez, F. Rossi, and A. Nicolini. The IRAIT Project Infrared Astronomy from Antarctica. In M. Giard, F. Casoli, and F. Paletou, editors, *EAS Publications Series*, volume 14 of *EAS Publications Series*, pages 181–186, 2005.

[25] Anna Moore, Eric Aristidi, Michael Ashley, Maurizio Busso, Maurizio Candidi, Jon Everett, Suzanne Kenyon, Jon Lawrence, D. Luong-Van, Andre Phillips, Brice Le Roux, Roberto Ragazzoni, Piero Salinari, John Storey, Melinda Taylor, Gino Tosti, and Tony Travouillon. The gattini cameras for optical sky brightness measurements in antarctica. volume 6267, page 62671N. SPIE, 2006.

[26] E. Høg, C. Fabricius, V. V. Makarov, U. Bastian, P. Schwekendiek, A. Wicenec, S. Urban, T. Corbin, and G. Wycoff. Construction and verification of the Tycho-2 Catalogue. A&A, 357:367–386, May 2000.

[27] W. A. Joye and E. Mandel. New Features of SAOImage DS9. In H. E. Payne, R. I. Jedrzejewski, and R. N. Hook, editors, *Astronomical Data Analysis Software and Systems XII*, volume 295 of *Astronomical Society of the Pacific Conference Series*, pages 489–+, 2003.

[28] J. W. Storey, M. C. Ashley, and M. G. Burton. Beyond Dome C. *Astronomy in Antarctica, 25th meeting of the IAU, Special Session 2, 18 July, 2003 in Sydney, Australia, meeting abstract*, 2, 2003.